Title

Fluid dynamics, heat transfer, and power efficiency of piezoelectrically actuated pitching plates for low-power thermal management

Author

Dehdari Ebrahimi, Navid

Publication Date

2020

UNIVERSITY OF CALIFORNIA

Los Angeles

Fluid dynamics, heat transfer, and power efficiency of piezoelectrically actuated pitching plates for low-power thermal management

A dissertation submitted in partial satisfaction
of the requirements for the degree
Doctor of Philosophy in Mechanical Engineering

by

Navid Dehdari Ebrahimi

2020

ABSTRACT OF THE DISSERTATION

Power consumption, fluid dynamics, and heat transfer study of piezoelectric fans for low-power thermal management

by

Navid Dehdari Ebrahimi

Doctor of Philosophy in Mechanical Engineering

University of California, Los Angeles, 2020

Professor Yongho Sungtaek Ju, Chair

Current trends in consumer electronics thermal management have prompted a strong push toward low-power and low-noise air moving devices due to the inability of conventional rotary fans to provide satisfactory performance for small-scale applications. Piezoelectric fans, on the other hand, offer an intriguing alternative owing to their simpler structure, less noise, and lower power consumption. Piezoelectric fans typically consist of a flexible plate attached to a piezoelectric actuation beam that oscillates the plate near its resonance frequency, causing the plate to undergo large-amplitude vibrations, which in turn induces net airflows in the streamwise direction and enhances convective heat transfer from heated surfaces.

Despite being available for more than 40 years, a comprehensive understanding of the power consumption mechanisms, complex fluid dynamics, and their correlation with heat transfer performance of the piezoelectric fans is missing from the relevant literature. In the present study, we aim to fill this knowledge gap and provide practical guidelines to facilitate the optimized design of these fans for a variety of thermal applications.

We first report a combined experimental and modeling study to help elucidate power consumption mechanisms in piezoelectric fans. We identify three main sources of power consumption, namely dielectric loss, hysteresis loss, and aerodynamic loss. We then correlate the aerodynamic loss, as the portion of the total power most related to airflow generation, with the thermal performance of the fan. Based on the models derived in this study, practical recommendations are provided in order to increase the power efficiency of the fans.

Next, we perform a combined experimental and numerical study on the vortex regimes present in the wake of piezoelectric fans of systematically varied geometries, resonance frequencies and amplitudes. We focus on the two-dimensional wake vortices on the mid-span plane. Three distinct vortex regimes are identified in the wake based on the fan's oscillatory Reynold number. A regime map is proposed next, denoting the incident of each vortex regime as a function of relevant dimensionless parameters. Finally, the effects of these vortex regimes on the flow generation capability, and hence power efficiency of the fans, are examined.

We then extend the previous study to the three-dimensional characteristics of the time-averaged induced jet in the wake of piezoelectric fans and correlate these characteristics with the transient vortex structures in the wake and their temporal evolution. Our results reveal, for the first time, the unconventional dual region of the induced jet in the wake of pitching plates; a shrinking region immediately downstream of the trailing edge followed by an abrupt expansion region. Scaling laws are also provided to facilitate predicting the jet boundary at various operating conditions and plate geometries.

Finally, we investigate the effect of the shape of the oscillating plate on the thermo-power efficiency of the fans. Plates with concave and convex trailing edges and varying upstream surface areas are compared in their flow generation capability, power consumption, and thermal performance. Based on our experimental results, recommendations are provided for choosing the most efficient plate shape based on application and space constraints. The effect of heated surface roughness is also examined as another means to enhance the thermo-power efficiency of the piezoelectric fans.

The dissertation of Navid Dehdari Ebrahimi is approved.

Adrienne G. Lavine

Jeffrey D. Eldredge

Marcus Roper

Yongho Sungtaek Ju, Committee Chair

University of California, Los Angeles

2020

Dedication:

To my beloved family who patiently encouraged me from 7,900 miles away during my five-year absent while working on this dissertation.

To my lovely Negar, for having faith in me when I didn’t.

Contents

List of Figures

ACKNOWLEDGEMENTS

I would like to express my sincere appreciation and gratitude to my advisor, Professor Yongho Sungtaek Ju, for his enthusiastic guidance and encouragement throughout my Ph.D. research, as well as his insightful suggestions and supports for my future career development.

I would also like to thank my committee members, Professor Adrienne Lavine, Professor Jeff Eldredge, and Professor Marcus Roper for their valuable suggestions and encouragements.

My appreciation also extends to my former and current colleagues at UCLA Multiscale Thermosciences Laboratory: Jinda Zhuang, Cheng Peng, Yide Wang, Chao Fan, Zhengxian Qu, Dong Hyun Ko, and Erfan Sedighi for their help and support. A special thanks to Abolfazl Sadeghpour for being a supportive colleague, roommate, teammate, and friend.

I would also like to thank Mr. Roy Kornbluh and other researchers at SRI International whose ideas and guidance were critical in initiating this thesis.

I am also grateful to staff members of UCLA mechanical engineering department, Mr. Benjamin Tan and Mr. Miguel Lozano, for their assistance and support in material testing, device fabrication, and teaching assistant training.

I am thankful to my friends, Samira Chizari, Sepehr Ghasemi, Shadi Torabi, Katayoun Yazdinejad, Behnam Shahbazi, Hamed Nilchi, and other “dining hall” and “zizigooloo” team members for all the fun and memorable moment we made together at UCLA.

Finally, I would like to give my deepest gratitude to my mom, dad, little sister – Niloofar – and my lovely partner – Negar – for their endless love and support throughout my Ph.D. studies.

VITA

2011-2015	Bachelor of Science Mechanical Engineering Department Sharif University of Technology, Tehran, Iran
2015-2020	Doctor of Philosophy Candidate Mechanical and Aerospace Engineering Department University of California, Los Angeles

PUBLICATIONS

Journal Publications

Navid Dehdari Ebrahimi, Yide Wang, Y. Sungtaek Ju, “Mechanisms of Power Dissipation in Piezoelectric Fans and Their Correlation with Convective Heat Transfer Performance”. *Sensors & Actuators A: Physical* 272 (2018): 242–252.

Navid Dehdari Ebrahimi, Y. Saungtaek Ju, "Thermal conductivity of sintered copper samples prepared using 3D printing-compatible polymer composite filaments." *Additive Manufacturing* 24 (2018): 479-485.

Navid Dehdari Ebrahimi, Jeff D. Eldredge, Y. Saungtaek Ju, "Wake vortex regimes of a pitching cantilever plate in quiescent air and their correlation with mean flow generation." *Journal of Fluids and Structures* 84 (2019): 408-420.

Navid Dehdari Ebrahimi, Jeff D. Eldredge, Y. Saungtaek Ju, "Three-dimensional characteristics of the jet flows induced by a pitching plate in a quiescent fluid". *Journal of Fluid Mechanics* 887 (2020).

Abolfazl Sadeghpour, Zezhi Zeng, Hanji Ji, **Navid Dehdari Ebrahimi**, Andrea L. Bertozzi, Y. Sungtaek Ju, Y. "Water vapor capturing using an array of traveling liquid beads for desalination and water treatment". *Science advances* 5.4 (2019): eaav7662.

Conference Publications

Navid Dehdari Ebrahimi, Zezhi Zeng, Y. Sungtaek Ju. "Vortex Propagation in Air Flows Generated by Piezoelectric Fans and Their Correlation with Fan Cooling Power Efficiency,". *Proceedings of the 16th International Heat Transfer Conference IHTC-16(2018)*

Navid Dehdari Ebrahimi, Y. Saungtaek, "Heat Transfer Augmentation Using Scale-Roughened Surfaces for Low-Reynolds Number Flows Generated by Piezoelectric Fans." *18th IEEE Intersociety Conference on Thermal and Thermomechanical Phenomena in Electronic Systems (ITherm). IEEE, 2019.*

Chapter 1. Introduction

1.1 Motivation

Recent developments in portable and wearable electronics with limited access to power sources have led to challenges in their thermal management. This challenge is even more pronounced when operating at small scales (sub-centimetric). At these scales, conventional rotary fans are difficult to fabricate and are power inefficient due to increased ratio of surface forces (friction) to volume forces (electromagnetic). Piezoelectric fans, on the other hand, are promising alternatives because of their simpler structures, less noise, and lower power consumption [1]–[3]. Piezoelectric fans typically consist of flexible blades attached to ceramic actuation beams. When operated near its resonance frequency, the blade undergoes large-amplitude vibrations, which in turn generates net airflows in the forward direction and induce convective heat transfer. Figure 1.1 depicts a typical piezoelectric fan with rectangular vibrating plates. In the past few years, there has been a constant push toward low-noise and low-power thermal solutions in consumer electronics industry, such as laptops and personal computers, which has motivated research and development efforts around piezoelectric fans. A major portion of this research concerns the thermal performance of these fans with little to zero attention to the details of fluid-solid interactions and power consumption mechanisms, to the extent that a comprehensive understanding of the operation of the fans, from the electromechanical energy conversion in the actuator to the vortex-induced jet and eventually convective heat transfer at the heat source, is missing in the relevant literature. In this study, we aim to fill this gap and eventually provide a guideline for the systematic design and optimization of these fans.

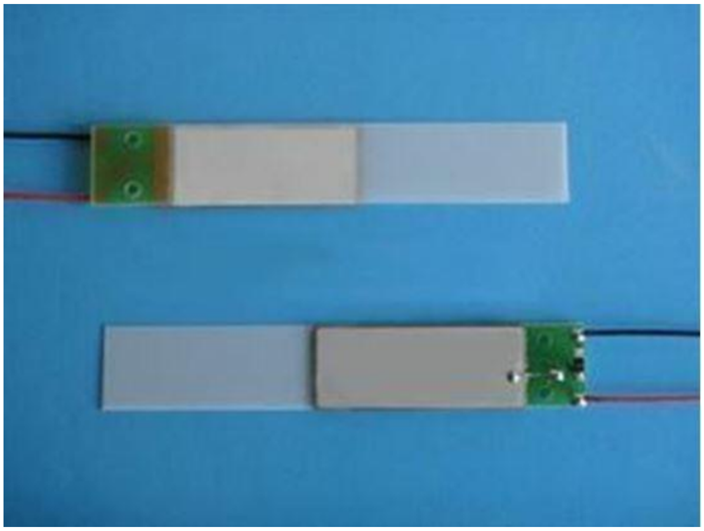

Figure 1.1 Typical piezoelectric fans (image obtained from steminc.com). Two main components of a piezoelectric fans, namely piezoelectric actuator and the flexible cantilever plate, are clearly distinguishable in the image.

1.2 Applications of piezoelectric fans

1.2.1 Personal cooling devices

Wearable personal cooling/heating devices have recently gained considerable attention in the energy conservation field as they enable huge energy savings by localizing the thermal management to a small area around the occupants' body rather than the entire building. Heating, Ventilation, and Air Conditioning (HVAC) account for 13% of the energy consumed in the U.S. and about 40% of the energy used in a typical U.S. residence, making it the largest energy expense for most residential and industrial buildings. These wearable technologies can reduce HVAC energy consumption by 15%. In addition, by reducing the power consumption of buildings, we open a path towards more sustainable heating and cooling architectures by possibly replacing their energy sources with renewable counterparts such as solar and wind. This, in turn, has huge environmental benefits as the heating and cooling of buildings generate about 13% of the U.S. domestic greenhouse gas emissions.

Due to their strict size and weight requirements, these devices are very limited in energy storage capacity (battery size). Consequently, regular rotary fans are not suitable choices to be used in their design due to their high power consumption. Piezoelectric fans, on the other hand, provide a power-efficient thermal solution for this application. An example of such devices is personal cooling shoes. Figure 1.2 shows the simple operation of these shoes. Excess heat is navigated to the sole of the feet via numerous blood vessels that act as the body's thermal regulators. This heat is then transferred to a working liquid that circulated in the insole. This liquid, in turn, rejects the heat to the small heat sinks at the bottom.

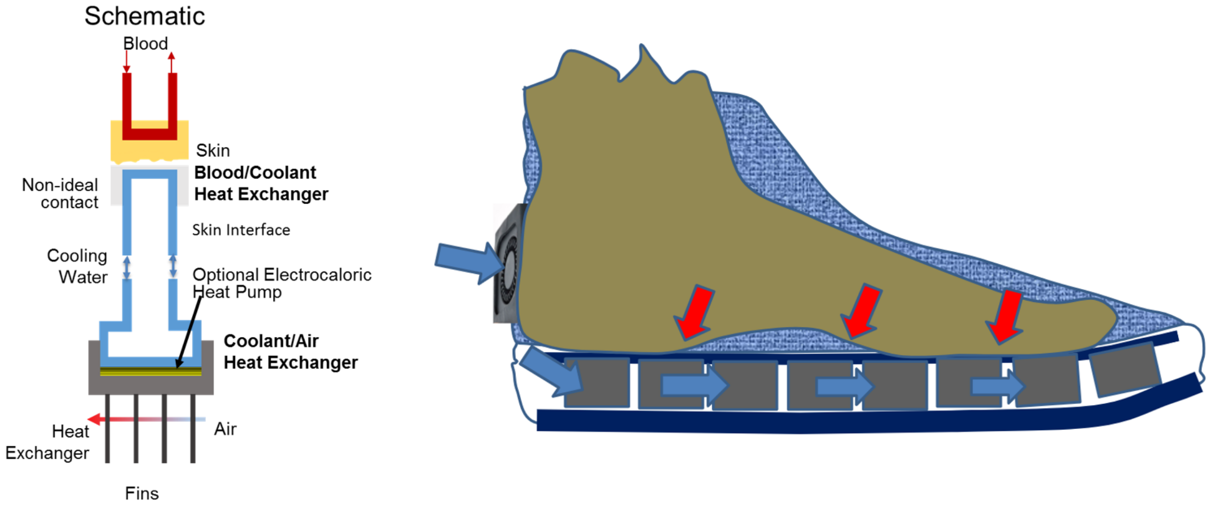

Figure 1.2 operation principle of shoes with integrated cooling system (courtesy of ReBOOT project, SRI). Piezoelectric fans can be used in the heat exchanger section to enhance the heat dissipation to the environment with minimum power consumption.

1.2.2 Electronics cooling

Another area of research around piezoelectric fans is their application in portable consumer electronic devices such as laptops, virtual reality and augmented reality goggles, and stationary electronic devices such as PCs and gaming consoles. In addition to their low power consumption, a feature that makes these fans interesting choices for these applications is their low noise due to their frictionless operation. The small amount of noise generated by these fans is attributed to the vibrations of the pitching plate and its imperfections. Therefore, many of these noise sources can be reduced or eliminated by a better choice of plate material. Acikalin et al. [4] performed a feasibility study of piezoelectric fans for small scale electronics cooling. They investigated the thermal performance and noise generation of the fans when used in a commercially available laptop. They reported that the noise level of the fan was not measurable in their office environment. They also observed a ~6^{o}C temperature drop in the components close to the location of the piezoelectric fan. They concluded that although these fans are not intended to replace rotary fans in high-power electronics, such as laptops, they can be used to provide supplemental cooling in hot spots where rotary fans cannot be used due to their inefficiency or form factor.

Up to now, the main challenge in using piezoelectric fans for consumer electronic products remain to be the reliability issues related to the frequency shift and piezo material fragility. In the last chapter of this dissertation, practical recommendations are made to alleviate these issues.

1.3 Background

1.3.1 Heat transfer study of piezoelectric fans

As discussed earlier, most of the literature about piezoelectric fans focus primarily on their thermal performance. Past studies [5], [6], [4], [7]–[12] examined the effects of various parameters on the heat transfer performance of piezoelectric fans. These parameters include the gaps between blade tips and surrounding surfaces; the relative thickness and mechanical modulus of piezoelectric and blade materials; the blade length and width; and the amplitude and frequency of vibration. In their study of the effects of side and tip gaps, Sufian *et al*. [7] observed a considerable reduction in the convective heat transfer coefficient as the tip gap is increased. However, very minor influence from the side gaps was observed. Figure 1.3 shows the measured heat transferred coefficients in their work along with their experimental setup.

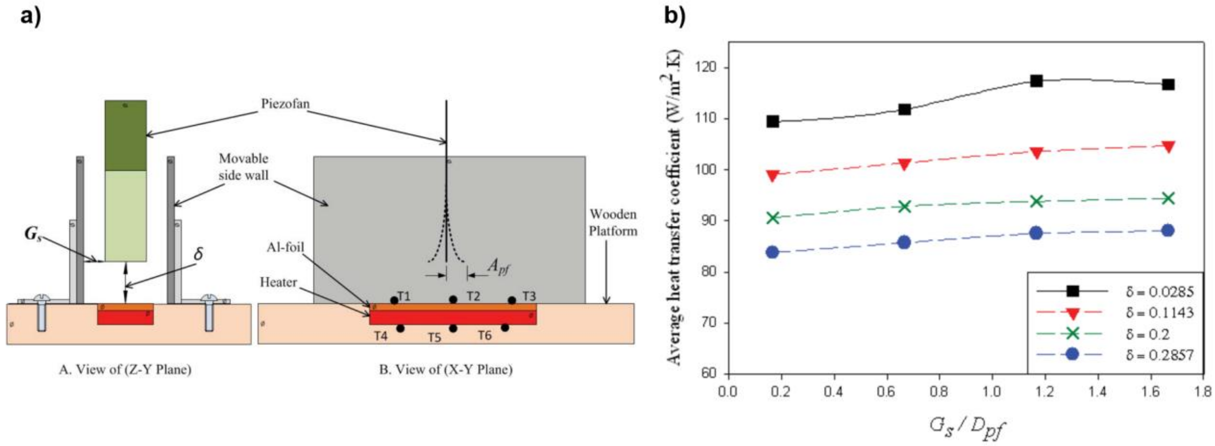

Figure 1.3 (a) experimental setup used by Sufian et. al [7] to investigate the effect of side and tip gaps on the heat transfer performance of the fans (b) average convective heat transfer coefficients reported in the same study as a function of side and tip gaps.

In another study by Acikalin *et al*. [10], authors concluded that the amplitude of oscillations and the shift from resonance frequency are prominent factors in the thermal performance of the piezoelectric fans with fixed tip gap to the heat source.

Huang *et al*. [13] used 3D numerical simulation in conjunction with an inverse design technique to determine the optimum position of a fan blade for maximum heat transfer performance. A similar approach was used to find the optimal positions and phase angle of a dual piezoelectric fan assembly [14]. Petroski et al. [15] attempted to tailor airflows created by piezoelectric fans using complex geometric features to improve cooling performance. They proposed a geometrically complicated heatsink design that conforms to the complex 3D flows generated by piezoelectric fans. Although these past studies provide valuable insight into the thermal performance of the piezoelectric fans in different situations, they don’t clearly correlate the thermal performance to the power consumption of these fans.

1.3.2 Power consumption study of piezoelectric fans

Power consumption is an important aspect of piezoelectric fans, especially, for applications with limited access to energy sources. There are very few studies in the literature that investigate the power consumption of a complete piezoelectric fan (i.e. actuator and plate). Most of the available studies focus on the power consumption in either the actuator or the oscillating plate separately. Liang et al. [16] reported an impedance method for calculating electrical power dissipation in piezoelectric beams. The advantage of this method is its simplicity and ease of use in mechanical models. This model, however, was developed for linear piezoelectric actuators and cannot be generalized for piezoelectric fans that comprise bimorph cantilever actuators. Cho et al. [17] extended this work and developed a five-port equivalent electric circuit model, where power dissipation in piezoelectric bimorphs was represented in terms of a 5×5 impedance matrix. This model, however, is unnecessarily complex for the case of piezoelectric fans and yet does not consider the aerodynamic effects of the plate.

Electrical losses in the actuator, however, represent only a portion of power dissipation in piezoelectric fans. Mechanical losses due to mechanical hysteresis in shims and interfacial bonding materials, for example, can be appreciable. In a related study, Sheu et al. [18] observed that the hardness and thickness of bonding materials can have significant effects on vibration amplitudes, and hence, the power consumption. Wait et al. [19] experimentally studied the electromechanical coupling factors (EMCF) of piezoelectric fans and concluded that the highest EMCF could be achieved at the 1st resonant natural frequency as opposed to higher-order resonant frequencies. The

EMCF is a measure of the efficiency of the fans in converting electrical energy to mechanical energy. Their study was one of the first studies that measured the total power consumption of a complete piezoelectric fan. However, more systematic studies are required to characterize and categorize different portions of power consumption in a piezoelectric fan in order to enable power-optimized and efficient designs.

1.3.3 Fluid dynamics study of piezoelectric fans

The fluid dynamics of piezoelectric fans, and pitching plates in general, have been widely investigated in the literature. These studies proceeded classic investigations of vibrating cylinders in water [20]–[22] which revealed different vortex regimes in the wake of a cylinder at different vibration frequencies and amplitudes and examined their impact on the drag and lift forces.

In their 2D study, Koochesfahani [23] and Bohl *et al.* [24] reported vortical patterns resulting from sinusoidal and non-sinusoidal pitching airfoils under varying free stream conditions. They observed that changes from negative (drag) to positive (thrust) force coefficients or from velocity deficit to velocity excess occur at specific frequencies and amplitudes that nearly correspond to changes in vortex patterns. Similarly, Schnipper *et al.* [25] experimentally demonstrated different vortex patterns in the wake of a pitching airfoil in a uniform free stream flow and reported a phase diagram in the dimensionless frequency and amplitude space. Figure 1.4 shows sample vortex patterns observed by Schinpper *et al.* and the constructed regime map.

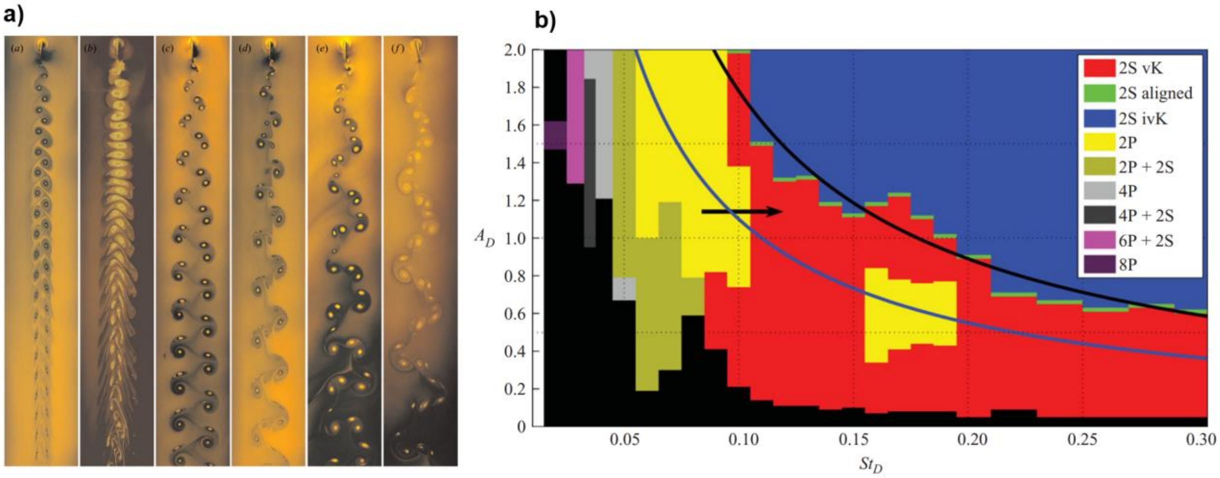

Figure 1.4 (a) Observed vortex patterns in the wake of an oscillating airfoil. (b) Phase diagram of vortex synchronization regions spanned by the width-based Strouhal number and the dimensionless amplitude. Figures are extracted from Schnipper *et al.* [25].

Buchholz *et al.* [26]–[28] investigated the wake structure of a series of low-aspect-ratio pitching plates in a non-zero freestream environment and found that with decreasing the aspect ratio or increasing the Strouhal number, the vortex pattern in the wake changes from 2S, 2 single vortex per cycle, to 2P, where two pairs of vortices are shed in each cycle. The above-referenced studies, however, cannot be generalized to vibrating cantilever plates operating in air, such as piezoelectric fans, which involve zero freestream velocity and operate at higher Reynolds numbers.

Lai [29] studied a plunging airfoil in quiescent water, but no observations on associated vortex patterns were reported. Heathcote *et al.* [30] examined flexible flapping beams in a quiescent fluid to analyze the effect of the beam amplitude and stiffness on the thrust generation. This study was again performed at low Reynolds numbers and the vibration amplitudes at the leading edge were comparable with those at the trailing edge, as opposed to the piezoelectric fans.

Kim *et. al.* [31]–[34] studied flow fields generated by vibrating flat beams in air both numerically using the moving mesh method and experimentally using the PIV and smoke visualization techniques. These results helped elucidate the mechanisms of vortex generation and transport, but only a single frequency and a narrow range of amplitudes were considered. In fact, as we shall show later in chapter 3, for the particular frequency used, the transition band between different vortical regimes is narrow and thus, difficult to capture. Figure 1.5 shows a sample of their PIV results. Eastman *et al.* [35] studied the thrust force generation by vibrating cantilever plates and proposed a correlation between the thrust and the vibration amplitude and frequency. The frequency range used in this study, however, was again rather narrow (59 – 63 Hz).

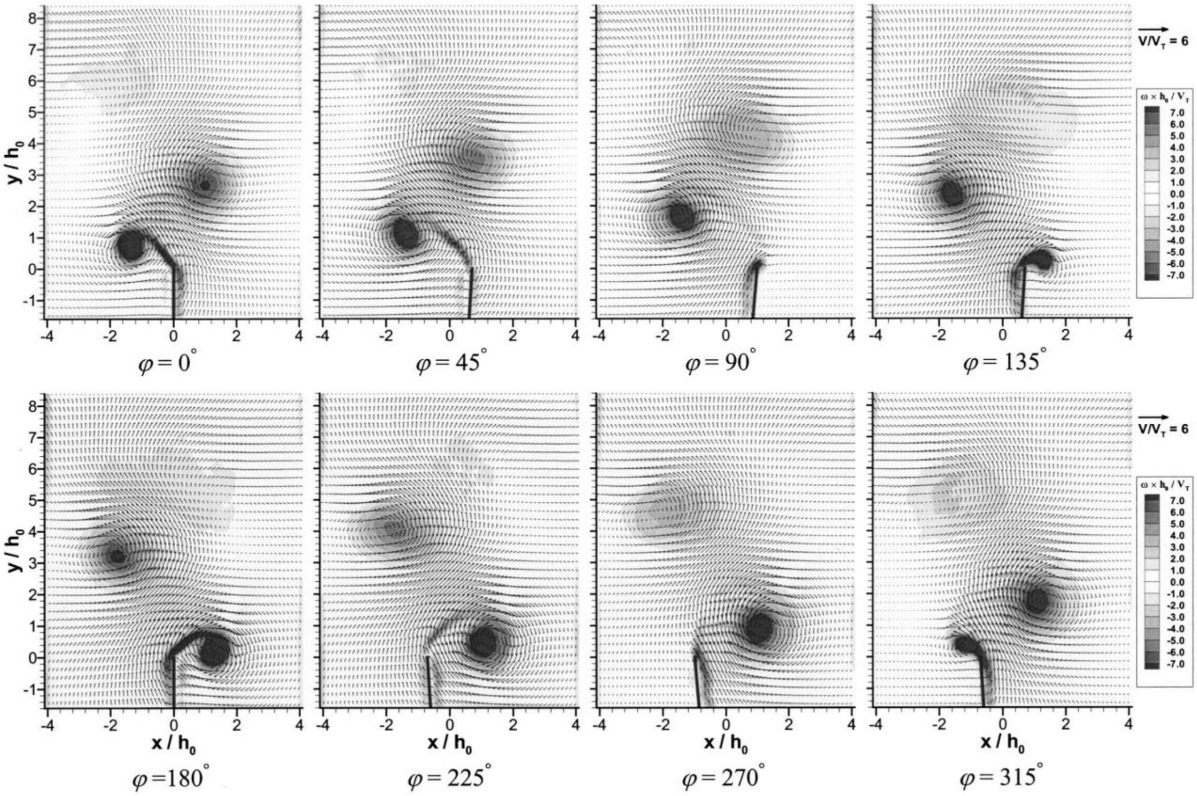

$\varphi = 0^\circ$ $\varphi = 45^\circ$ $\varphi = 90^\circ$ $\varphi = 135^\circ$

$\varphi = 180^\circ$ $\varphi = 225^\circ$ $\varphi = 270^\circ$ $\varphi = 315^\circ$

Figure 1.5 Sample PIV results in a full cycle of piezoelectric fan oscillations, demonstrating two opposite-signed vortices created in each cycle of oscillations. Figures are extracted from Kim et al. [31].

Shrestha *et al.* [36] proposed a 2D vortex regime map for a vibrating cantilever plate in the dimensionless frequency and amplitude domain. This past study was, however, concerned with flows generated from the lateral sides of a vibrating cantilever plate, as opposed to the downstream of its trailing edge, because the primary focus of the study was the relation between aerodynamic drag forces and observed vortex patterns. The reported results were also limited to a cantilever plate of fixed geometry.

Past 3D studies demonstrated that the vortices shed from the trailing and lateral edges of a pitching plate form horseshoe structures in the wake that interact with each other as they propagate downstream with the flow. Buchholz *et al*. [26], [27], [37]–[39] observed that each horseshoe is significantly deformed under the influence of two subsequent horseshoes: an opposite-sign interaction with the horseshoe shed immediately after and a like-sign interaction with the horseshoe that follows with 2π phase difference. This interaction is best demonstrated in figure 1.6. Green *et al.* [40]–[42] performed 3D PIV combined with a Lagrangian Coherent Structure (LCS) analysis on trapezoidal pitching plates in free stream and provided 3D graphical representations of the vortex structures in the wake, confirming the aforementioned interactions. Taira and Colonius [43] used numerical simulations to investigate the transient structures shed from a pitching plate in a free stream starting from rest. By studying the three-dimensional horseshoe vortex structures emanating from a pitching plate in a quiescent fluid, Agarwal *et al.* [44] showed that the complex interactions reported in the previous studies are highly influenced by free stream flows and that they are largely absent in quiescent fluids. Oh *et al.* [34], [45] used moving mesh 3D numerical simulations to analyze the vortex structures and flow field in the wake of a pitching plate in a quiescent fluid confined by two end walls. They demonstrated for the first time the unconventional 3D shape of the mean jet downstream of a pitching plate. The shape of the jet downstream of piezoelectric fans is analyzed in more depth in chapter 4.

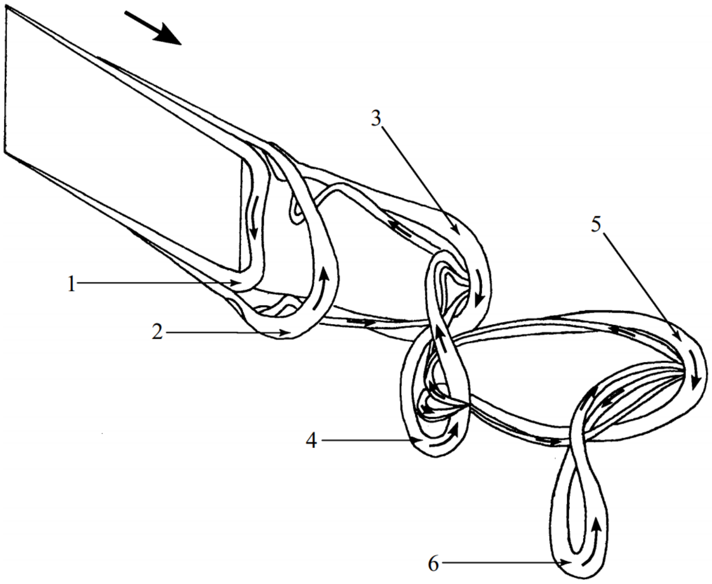

Figure 1.6 Schematic of 3D vortex structures in the wake of a pitching plate with aspect ratio of *AR* = 0.54, Strouhal number of *St* = 0.23, and Reynold number of *Re* = 640 (Buchholz and Smits [26]). Different numbers represent the order of horseshoe structures that are generated in each half cycle, with the lowest number being the newest structure.

1.4 Objective of the present work

In the present study, we aim to provide a comprehensive investigation of the power consumption mechanisms, complex fluid dynamics, and heat transfer performance of piezoelectric fans with the goal of facilitating the optimized design of these fans for a variety of applications. Our efforts in the current work are focused on (i) providing a simple and experiment-backed analytical model for the power consumption of the piezoelectric fans and propose a guideline for selecting optimal fan operating conditions for maximum power efficiency, (ii) investigating the vortex regimes in the wake of thin cantilever plates of systematically varied geometries, resonant frequencies and amplitudes oscillating in quiescent air in order to understand their correlation with downstream flow generation, (iii) revealing the three-dimensional characteristics of the time-averaged air jet downstream of the piezoelectric fans and its complex dependence on the vibrational and geometrical parameters of the fan, (iv) and proposing various methods to enhance the power efficiency of these fans through systematic changes to the plate geometry or the heated surface roughness.

1.5 Organization of the document

The rest of this dissertation is organized as follows. In chapter 2 we report a combined experimental and modeling study to help elucidate power dissipation mechanisms in piezoelectric fans. We examine three main sources of power dissipation: dielectric loss within a piezoelectric actuator; mechanical hysteresis loss; and viscous dissipation in induced airflows. We use independently validated mechanical models together with experimentally measured data to estimate the contribution from each source of power dissipation. Convective heat transfer coefficients and normal forces due to the fan's operation are then correlated with the component of power directly related to induced air flows, referred to as air flow power. An optimal bias voltage for maximum power efficiency, as characterized by the ratio of the air flow power to the total consumed power, is then determined using our model. Lastly, we relate the air flow power, and hence indirectly the heat transfer coefficient and normal force, to the blade's geometrical parameters to facilitate systematic optimization of the blades for both cooling performance and power efficiency.

Chapter 3 provides our two-dimensional experimental and numerical study of the vortex regimes present in the wake of a harmonically oscillating thin cantilever plate in a quiescent fluid (which can be very well generalized to the piezoelectric fan flows) and their effect on the flow generation downstream. We perform particle imaging velocimetry (PIV) experiments together with numerical simulation based on the immersed boundary method (IBM) to characterize vortex generation and propagation and to compare the temporal decays of vortices generated in different regimes.

In chapter 4, we investigate the three-dimensional characteristics of the time-averaged induced jet in the wake of an unconfined pitching cantilever plate in a quiescent fluid and correlate these characteristics with transient vortex structures in the wake and their temporal evolution. We perform 2D and 3D PIV experiments together with three-dimensional immersed boundary numerical simulations to visualize and extract wake structures downstream of plates of different vibrational (frequency and amplitude) and geometric (width and length) parameters and provide a guideline to predict the shape of the jet.

In chapter 5, we investigate the effect of the plate geometry on the flow generation capability, power consumption and thermal performance of the piezoelectric fans as a means of improving their efficiency.

Lastly, chapter 6 includes our study of the effect of the heat source roughness on the thermal and power performance of the piezoelectric fans as another means of improving their efficiency.

Chapter 2. Power dissipation mechanisms in piezoelectric fans

2.1 Background

Understanding the power consumption mechanisms in piezoelectric fans is a crucial step towards optimizing their performance. Any change in the motion or geometry of the plate or the surface properties of the heated object is considered improvement only if it delivers the same thermal performance with less power consumption. The power consumption of the piezoelectric fans and their correlation with flow generation and thermal performance have not received adequate attention in the relevant literature. As previously pointed out in Chapter 1, only a handful of studies have delved into the power consumption in piezoelectric fans [16], [17], [19]. These studies, however, do not answer some questions that are critical for systematic design and optimization of these fans. For instance, what are different mechanisms of power consumption in these fans? What is the amplitude and frequency dependence of each source? what are the contribution of each of these sources of power loss, or in other words, how much improvement do we get if we reduce the power consumption of each source? Which mechanism(s) is (are) directly related to the flow generation and thus, the heat transfer performance and which ones are parasitic losses? How can we increase the power efficiency of these fans? In the following chapter, we try to provide an in-depth investigation of the power consumption in piezoelectric fans and answer the above questions.

2.2 Nomenclature

A_{act}	Amplitude of the actuator, m	$P_{\mathrm{dielectric}}$	Dielectric loss in the actuator, mW
A_{blade}	Amplitude of the blade, m	P_{flow}	Airflow power, mW
C_1	Structural damping of the actuator, kg/s	P_{total}	Total power consumption of the fan, mW
$C_{2,\mathrm{a}}$	Aerodynamic damping of the blade, kg/m	Q_{heater}	Heater Power, W

C_{act}	Actuator coefficient, m/V
C_{blade}	Blade coefficient, dimensionless
C_{H}	Hysteresis coefficient, N/V
C_{Y}	Dielectric loss coefficient, J/V^4
d	Location of the added mass, m
d_{e}	Piezoelectric displacement factor, m/V
E	Young’s modulus, GPa
F	Force on an opposing surface, mN
F_0	Equivalent force at the tip of the actuator, N
f	Frequency, Hz
H	Hysteresis factor, N
h_{total}	Total (free and forced) convection heat transfer coefficient, W/m^{2}K
k_1	Bending stiffness of the actuator, N/m
k_2	Bending stiffness of the blade, N/m
k_{air}	Thermal conductivity of air, W/mK
L	Length of the heated surface, mm
l_{b}	Length of the blade, mm
l_{p}	Length of the actuator, mm
m_0	Original mass, kg
$m_{\text{e},1}$	Effective mass of the actuator, kg
$m_{\text{e},2}$	Effective mass of the blade, kg
Nu_{total}	Total (free and forced) Nusselt number, dimensionless
P_{actuator}	Power consumption in the actuator, mW

Q_{loss}	Heat loss, W
Re	Reynolds number, dimensionless
$\text{Re}(Y)$	Real part of the actuator admittance, 1/Ω
S	Area of the heated surface, m^2
T	Period of oscillations, s
t	Time, s
t_{b}	Thickness of the blade, mm
$tan\delta$	Tangent loss factor of the actuator, dimensionless
u_{tip}	Blade tip velocity, fA_{blade}, m/s
V	Amplitude of the bias voltage, V
V_{max}	Bias voltage for maximum efficiency, V
V_{rms}	RMS voltage, V
w_{b}	Width of the blade, m
z	State variable, m

Greek symbols

α	Aerodynamic and geometrical parameter, J s^2/V^3
α_{p}	Parameter related to the shape of the hysteresis curve, dimensionless
β	Mechanical loss parameter, J /V^2
β_{p}	Parameter related to the shape of the hysteresis curve, dimensionless
γ	Hysteresis loss parameter, J /V^4
γ_{p}	Parameter related to the shape of the hysteresis curve, dimensionless
ω	Angular frequency, rad/s

2.3 Experimental setup

We use commercial piezoelectric fans (Steminc, Inc.) modified in-house for the present study. The piezoelectric actuator in each of the fans consists of two 185 μm-thick piezoelectric ceramic film (Pb ($Zr_{0.53}Ti_{0.47}$) O_3; PZT - 4) with a 142 μm-thick copper shim sandwiched in between. The other geometric parameters of the piezoelectric fans (figure2.1) and their natural resonant frequencies are listed in table 2.1. The blades of different thicknesses are made by bonding different numbers of Kapton sheets, each with a thickness of 0.127 mm. The blade width w_b is kept 12 mm. The actuators are clamped at the base to realize a cantilever configuration, as confirmed optically from the negligible slope of the actuator base during operation.

Table 2.1 Experiment variables

Control variable	l_b **(mm)**	t_b **(mm)**	*d* **(mm)**	**Frequency (Hz)**	**Voltage amplitude (V)**
blade length	63 - 20	0.26	-	30 - 188	70 - 140
blade thickness	32	0.13 - 0.5	-	35 - 119	70 - 140
location of mass	32	0.26	0 (no extra mass) - 17	62 - 20.7	50 - 190

We use a high-speed camera with a maximum frame rate of 16000 fps and a video zoom lens to measure the amplitude of both blade and actuator vibrations. The uncertainty in the measured vibration amplitudes is estimated to be approximately 7 µm, representing less than 5% of the typical values of the measured vibration amplitudes of the actuator. The mechanical hysteresis and structural damping in piezoelectric fans is characterized in a vacuum chamber at a pressure of approximately 1cm Hg where the effects of aerodynamic damping can be neglected [46].

A function generator (Model 33220A, Agilent) is used to generate small amplitude (0.4V - 2V) pure sinusoidal voltage waves, which are then amplified using a high-voltage amplifier with a current monitor output (Model PZD700A, TREK). The uncertainty due to voltage and current measurements are estimated to be 2 V and 0.041 A, or approximately 2% and 7% in typical measurements. The total power dissipation in a piezoelectric fan is obtained by numerically integrating the product of the measured voltage and current profiles (sampling rate 5000 Hz), with an estimated uncertainty of 0.5 mW, approximately 8% of typical measured powers.

Figure 2.2a schematically shows our experimental setups to characterize the heat transfer coefficient and normal aerodynamic force on flat surfaces. Convective heat transfer coefficients over a flat surface are measured using an aluminum block (2.5 cm × 2.5 cm × 0.48cm) that has a thin-film electric heater of the same lateral dimensions attached to its back. The aluminum block-heat assembly is enclosed in a Styrofoam insulation to minimize parasitic heat loss through the side and back surfaces. The front surface of the aluminum block is coated with a black paint (Kylon Colormaster No.1602) to achieve uniform controlled emissivity. Five K-type thermocouples are attached to the aluminum block at four corners and in the middle to monitor its temperature (figure 2.2 b). The spatial variations in the measured temperature rises, relative to the ambient temperature, are less than 5%. For all the experiments reported in the present manuscript, we keep the distance of the fan blade tip to the heated surface constant at 20 mm. The major paths of heat loss are conduction through the insulation layer on the back and side surfaces and radiation from the heated front surface. Heat loss is thus estimated by knowing the emissivity of the coating on the front surface and measuring the temperature profile of the back and side surfaces, using $Q_{\text{loss}} = [\int k_{\text{ins}} (T_i - T_o(x,y))/l \, dS\ ] + [\ \varepsilon\sigma S(T_s^4 - T_\infty^4)]$, where ε, σ, k_{ins}, l, S, T_o , T_s and T_∞ are the emissivity of the coating on the aluminum surface (0.95), the Stephan-Boltzmann constant, the thermal conductivity of insulation, the length of heat transfer (insulation thickness), the area of the heated surface, the insulation temperature, front surface temperature and the room temperature respectively. The estimated total heat loss rate through the insulation is approximately 13% of the typical heater power used in the present study. The values of total (combined free and forced) convection is then calculated from $h_{\text{total}} = (Q_{\text{heater}} - Q_{\text{loss}})/S(T_s - T_\infty)$. The reliability of the estimated values of h_{total} is validated by comparing the experimental results obtained for natural convection (with the fan being off) with the existing empirical correlations where we observed good agreement within 10% over the range of surface temperatures relevant to this study. The estimated uncertainties in total heat transfer coefficients and Nusselt numbers are ~3 W/m^{2}K and 5, respectively, approximately 12% of the typical values.

A weight scale (Model Adventurer Pro, Ohaus) with a resolution of 0.0001 g is used to measure the force exerted by a piezoelectric-fan-generated airflow on an opposing flat surface (figure 2.2c).

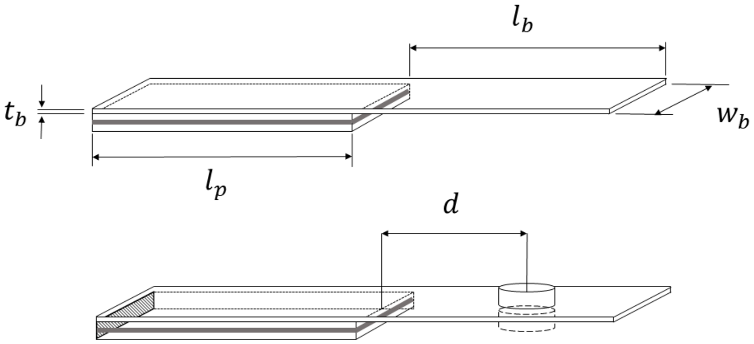

Figure 2.1 The length (l_b), the thickness (t_b) and the location of the center of mass (d) of the blades are varied in different sets of experiments. The width of the blade is fixed.

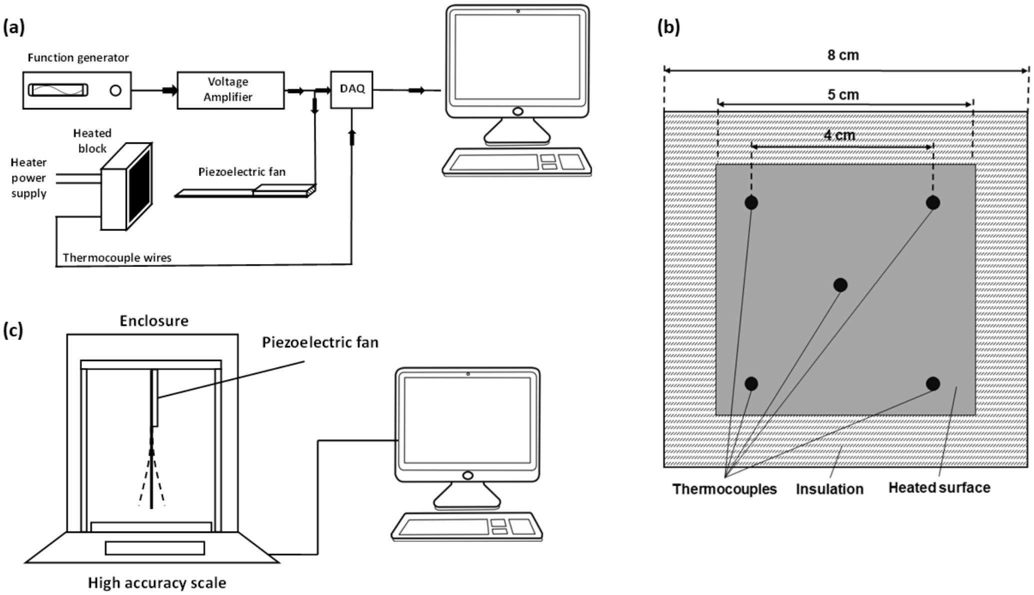

Figure 2.2 Schematic of a) the heat transfer and power measurement setup, b) the location of the thermocouples and c) the aerodynamic force measurement setup used in the present study.

2.4 Results and discussions

2.4.1 Models for power dissipation

Piezoelectric bimorph actuators – Actuators often used in piezoelectric fans are bimorph cantilevers with a metal shim sandwiched between two piezoelectric layers. In a piezoelectric fan operating at its resonance frequency, a considerable portion of power can be consumed in the actuator itself. We first consider power dissipation in the actuator, which can be divided into two main categories: 1) electrical losses and 2) mechanical losses. The electrical loss is due primarily to dielectric loss in the piezoelectric materials [47] whereas the mechanical loss is due to hysteresis loss in the shim and bonding layers [16], [18] and structural damping.

The dielectric loss is calculated using

$$P_{dielectric} = V_{rms}^2 \, Re(Y) \tag{2.1}$$

where Y is the electrical admittance of the piezoelectric material and V_{rms} is the RMS value of the applied sinusoidal voltage. The admittance in turn is a function of the tangent loss factor, $\tan \delta = j2\pi f[\varepsilon_r\varepsilon_0(1 - j\tan\delta)]\frac{l\,w}{2t}$. Here f, ε_r and ε_0 are the frequency, the dielectric constant and the vacuum permittivity, respectively. l, w, and t are the length, width and thickness of the piezoelectric material, respectively. We use the values reported in the literature for the tangent loss factor of the piezoelectric material used in the present study (PZT-4) [48], [49].

To quantify power dissipation due to mechanical hysteresis, we adapt a model reported by Low and Gou [50]. They introduce a state variable z, coupled with the equation of motion of the actuator:

$$\dot{z} = \alpha_p d_e \dot{V} - \beta_p|\dot{V}|z - \gamma_p \dot{V}|z|$$

$$m_{e,1}\ddot{y} + C_1\dot{y} + k_1 y = k_1(d_e V - z) \tag{2.2}$$

Here, α, β and γ are parameters related to the shape of the hysteresis loop, V is the excitation voltage amplitude, $m_{e,1}$ is the effective mass of the actuator (= 33/140 m_0), k_1 is the mechanical stiffness of the actuator beam, and F_0 is the equivalent force applied to the tip of the actuator. m_0 is the mass of the actuator and C_1 is the structural damping coefficient for the actuator.

We substitute V in Eq. (2.2) with a sinusoidal signal, $V = V_0 \sin(\omega t)$ and solve the first equation for the state variable z using representative values of α, β and γ reported in a previous study for piezoelectric actuators [29]. The predicted temporal variation in z, shown in figure 2.3, can be approximated with a step function, that is, a constant value with alternating signs tracking $\cos(\omega t)$, or the direction of the oscillation velocity.

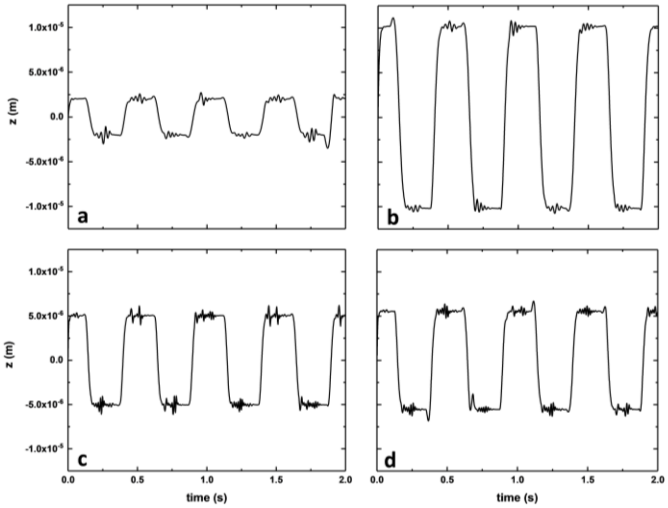

Figure 2.3 Calculated values of z for a sinusoidal excitation voltage with a) α=1×10^{-1}, β=5×10^{-2}, γ=-1×10^{-3}, d_e=1×10^{-6} b) α=5×10^{-1}, β=5×10^{-2}, γ=-1×10^{-3}, d_e=1×10^{-6} c) α=5×10^{-1}, β=1×10^{-1}, γ=-1×10^{-3}, d_e=1×10^{-6} d) α=5×10^{-1}, β=1×10^{-1}, γ=-1×10^{-2}, d_e=1×10^{-6}

For sinusoidal bias voltages and the ranges of vibration amplitudes considered in the present study, the model can be well-approximated by replacing the terms $k_1 d_e V$ and $k_1 z$ in Eq. (2.2) with the equivalent force F_0 due to bending of the actuator at the tip and the hysteresis parameter H, respectively.

$$m_{e,1}\ddot{y} + C_1\dot{y} + k_1 y + H\, sign\,(\dot{y}) = F_0 sin\,(\omega t) \tag{2.3}$$

Figure 2.4 shows the schematic representation of the mechanical model captured in Eq. (2.3).

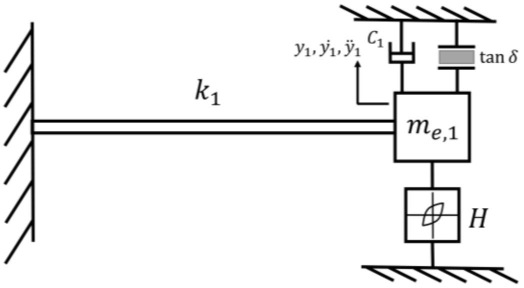

Figure 2.4 Schematic of the proposed mechanical model for the piezoelectric bimorph actuator that accounts for mechanical hysteresis (H) and structural damping (C_1).

The hysteresis parameter H has the unit of force and can be interpreted as a measure of the opposing force arising from mechanical hysteresis under harmonic excitation [18], [50].

To determine the hysteresis parameter, H, we experimentally obtain hysteresis loops of our piezoelectric actuators. Figures 2.5a-c show example hysteresis loops we obtain from our piezoelectric actuators for 3 different bias voltage amplitudes (50 V, 70 V, 120 V). Each loop is approximated using a parallelogram that conserves the area [51]. The intersections of the parallel top and bottom sides with the displacement axis, labeled z^+ and z^-, are obtained and averaged ($\bar{z}$). The hysteresis parameter is then calculated as $H = k_1 \bar{z}$, The values thus obtained are normalized with the corresponding equivalent tip bending force F_0 and listed in table 2.2 together with values reported in the literature for comparison. Measurements performed at two different actuation frequencies, 60 Hz and 150 Hz, show relatively small frequency dependence of the hysteresis parameter. We note that the piezoelectric fans are operated near the resonance frequencies of the blades (20 ~ 120 Hz). These are well below the resonant frequency of the actuator (~300 Hz), around which rate dependency of hysteresis causes significant deviation from quasi-steady condition [51]–[53]. Note that the extracted hysteresis parameter is approximately a linear function of the vibration amplitude and hence the bias voltage amplitude, consistent with the observation of the earlier study [51].

Table 2.2 H parameter (in N) obtained from hysteresis loop

	50 V	**70 V**	**120 V**	$H_{ave.}/F_0$	**Literature** [51]
60 Hz	0.039	0.062	0.092	0.46	0.4
150 Hz	0.041	0.074	0.095	0.48	0.51

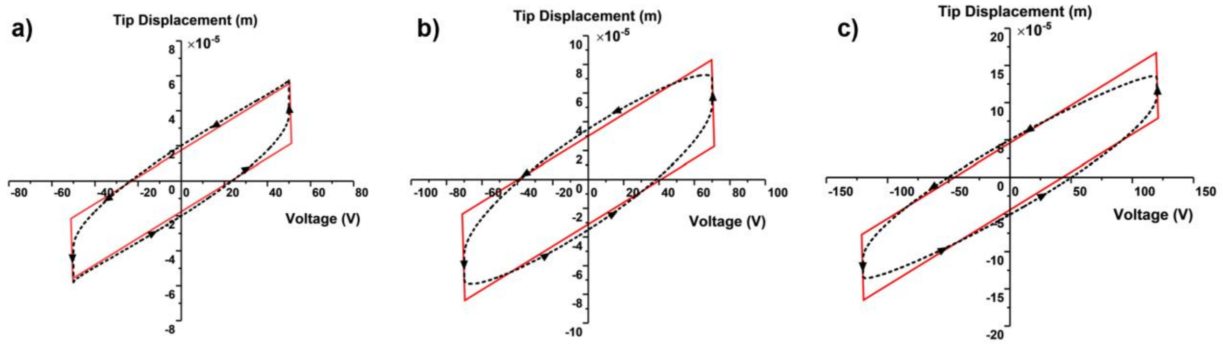

Figure 2.5 The measured hysteresis loop (black dashed lines) for a bimorph piezoelectric actuator subject to (a) 50 V (b) 70 V and (c) 120 V sinusoidal voltage at 60 Hz (resonance frequency of the piezoelectric fan). The solid line shows a parallelogram approximating the hysteresis loop.

The hysteresis parameter H can also be estimated independently by fitting the frequency-dependence of the vibration amplitudes of harmonically excited actuators measured in vacuum using Eq. (2.3) with H as the free parameter in a genetic algorithm [54]. Representative data of the tip vibration amplitudes normalized with respect to the static tip deflection (δ_{static}) are shown in figure 2.6 as a function of the normalized actuation frequency. Here, ω_{n} is the first resonant frequency of the actuator. The values of H obtained using this method agree with the values obtained using the hysteresis curves discussed above to within 15%. Also shown for comparison are the curve fits obtained without accounting for mechanical hysteresis (Eq. (2.3) with $H = 0$). The frequency-dependence of vibrational amplitudes cannot be captured properly without considering mechanical hysteresis.

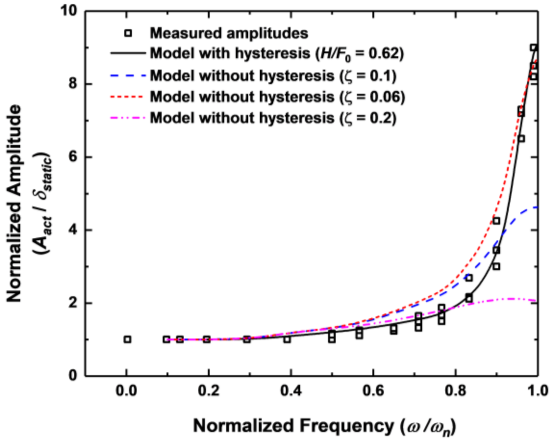

Figure 2.6 The normalized tip vibration amplitudes in vacuum as a function of the normalized frequency for a piezoelectric bimorph actuator. The solid line represents the model predictions that account for mechanical hysteresis and the dashed, short-dashed, and dash-dotted lines show the model fit without accounting for the mechanical hysteresis. ξ is the damping factor used for each case.

The power consumption in the actuator can be calculated using the following expression:

$$P_{actuator} = 4H|A_{actuator}|f + V_{rms}^{2}\,Re(Y) + 2\pi^{2}C_{1}|A_{actuator}|^{2}f^{2} \tag{2.4}$$

Here, $A_{actuator}$ is the vibration amplitude of the tip of the actuator and f is the vibration frequency. The last term represents dissipation due to structural damping. To determine power dissipation due to structural damping in piezoelectric actuators, we measure the step response of actuators under vacuum. We apply and then turn off a sinusoidal bias voltage of amplitude 100 V to an actuator. The resulting damped oscillations are then recorded and fitted with Eq. (2.3) to characterize structural damping (figure 2.7). The average damping coefficient of 0.071 kg/s, thus obtained, translates into a relatively small power consumption of ~ 0.05 mW (less than 1% of the typical power consumptions).

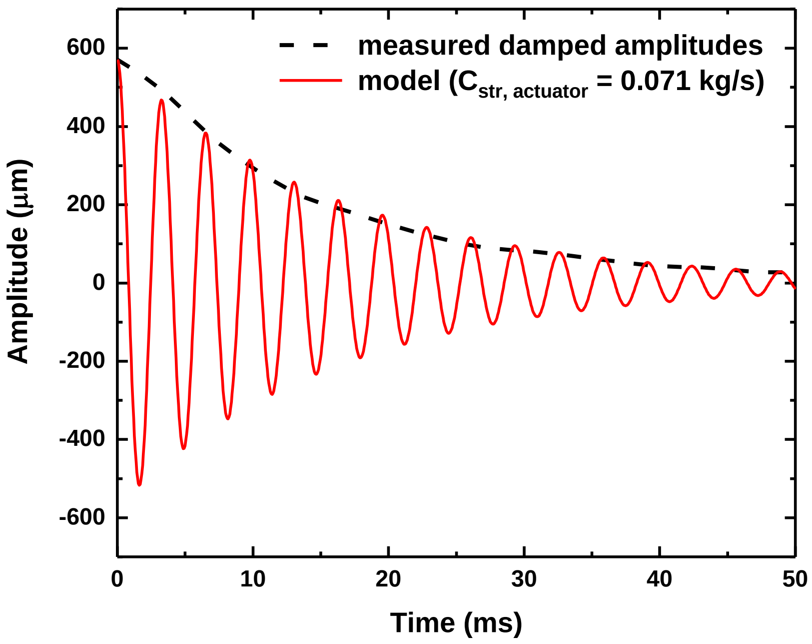

Figure 2.7 A representative step response of a bimorph actuator to characterize structural damping of the actuator.

Figure 2.8 shows the experimentally measured and predicted power dissipation in the actuator. For a fixed applied voltage amplitude, the power dissipation increases nearly linearly with the frequency. At a relatively low voltage amplitude (60 V), the dielectric loss is negligible [48], [49] and the mechanical hysteresis loss dominates the total power dissipation. At a higher voltage amplitude (100 V), the dielectric loss becomes more important. Under actuation conditions tested here, the mechanical hysteresis accounts for over 70% of the power dissipated in the actuators. The power dissipation predicted using our model agrees well with the experimental results. We emphasize that all the parameters used in the model, especially the hysteresis factor *H* and the dielectric loss factor *tan* δ, are obtained independently. Previous studies suggested approaches to reduce mechanical hysteresis loss [55][56][57].

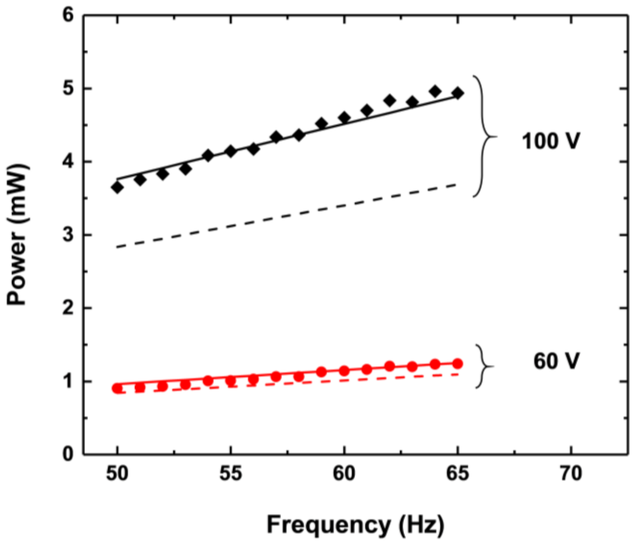

Figure 2.8 Power dissipation in the piezoelectric actuator under different applied voltages: 60 V (red) and 100 V (black). The experimentally measured values are shown as the symbols, the predicted mechanical loss as the dashed lines, and the sum of the predicted mechanical and electrical losses as the solid lines.

Complete piezoelectric fan – We next extend our model to consider total power dissipation in piezoelectric fans equipped with flexible blades. Figure 2.9 shows our mechanical model for a complete piezoelectric fan. Baker et al. [46] identified viscous dissipation in air flows generated by a vibrating beam as a major mechanism of power consumption in the system. For large-amplitude vibrations, where the tip displacements are comparable to the dimensions of the blade, previous studies ([46] [58]) showed that the rate of viscous dissipation is approximately proportional to the tip velocity squared. We characterize the structural damping of blades in the piezoelectric fans (figure 2.10) using a similar method described for the actuator. The associated power consumption is again relatively small, approximately 0.5 mW, accounting for less than 10% of typical total power consumption in the present study. In view of this, we neglect structural damping in the model as a separate source of dissipation for mathematical simplicity.

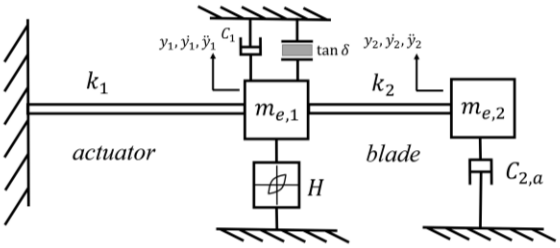

Figure 2.9 Schematic of the mechanical model we use to describe a complete piezoelectric fan.

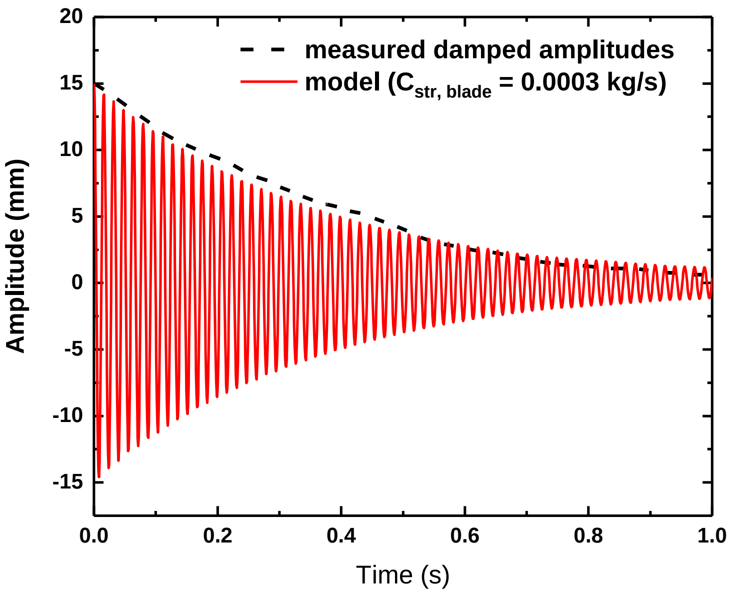

Figure 2.10 A representative step response of a blade in a piezoelectric fan to characterize structural damping.

The equation of motion of the complete mechanical system is:

$$\begin{bmatrix} m_{e,1} & 0 \\ 0 & m_{e,2} \end{bmatrix}\begin{bmatrix} \ddot{y}_1 \\ \ddot{y}_2 \end{bmatrix} + \begin{bmatrix} C_1 & 0 \\ 0 & 0 \end{bmatrix}\begin{bmatrix} \dot{y}_1 \\ \dot{y}_2 \end{bmatrix} + \begin{bmatrix} 0 & 0 \\ 0 & C_{2,a} \end{bmatrix}\begin{bmatrix} \dot{y}_1|\dot{y}_1| \\ \dot{y}_2|\dot{y}_2| \end{bmatrix} +$$

$$\begin{bmatrix} H & 0 \\ 0 & 0 \end{bmatrix} sign\left(\begin{bmatrix} \dot{y}_1 \\ \dot{y}_2 \end{bmatrix}\right) + \begin{bmatrix} (k_1+k_2) & -\mathrm{k}_2 \\ -k_2 & k_2 \end{bmatrix}\begin{bmatrix} y_1 \\ y_2 \end{bmatrix} =$$

$$\begin{bmatrix} F_0\, sin(\omega t) \\ 0 \end{bmatrix} \tag{2.5}$$

Here, $m_{e,2}$ is the effective mass of the blade, which is determined by transforming the distributed inertial force into a point force acting on the center of pressure [59], [60]. From the observation of negligible difference in resonance frequency between the ambient condition and vacuum, Bidkar et. al. [58] concluded that the added mass effect from air is negligible for typical piezoelectric fans.

The damping factor $C_{2,a}$ captures the aerodynamic damping of the blade vibration, which is a dominant source of power dissipation near the resonance. We fit the measured vibration amplitudes of the blades using Eq. (2.5) to determine C_{2a}. A representative result is illustrated in figure 2.11.

The rate of viscous dissipation, also referred to as the airflow power, is

$$P_{flow} = \frac{32\pi^2}{3} C_{2a} |A_{blade}|^3 f^3 \tag{2.6}$$

when averaged over one period. Here, A_{blade} is the vibration amplitude of the blade at its center of pressure and is linearly related to A_{tip}, the vibration amplitude at the tip of the blade.

Note that the blade tip velocity $u_{tip} = f A_{tip}$. The airflow power P_{flow} then scales as

$$P_{flow} \sim {u_{tip}}^3 \tag{2.7}$$

The total power dissipation in the piezoelectric fan is estimated by summing P_{flow} and $P_{actuator}$, while neglecting the structural damping of the actuator:

$$P_{total} = P_{actuator} + P_{flow} =$$

$$4H|A_{actuator}|f + V_{rms}^{2}\,Re(Y) + \frac{32\pi^{2}}{3}C_{2a}|A_{blade}|^{3}f^{3} \qquad (2.8)$$

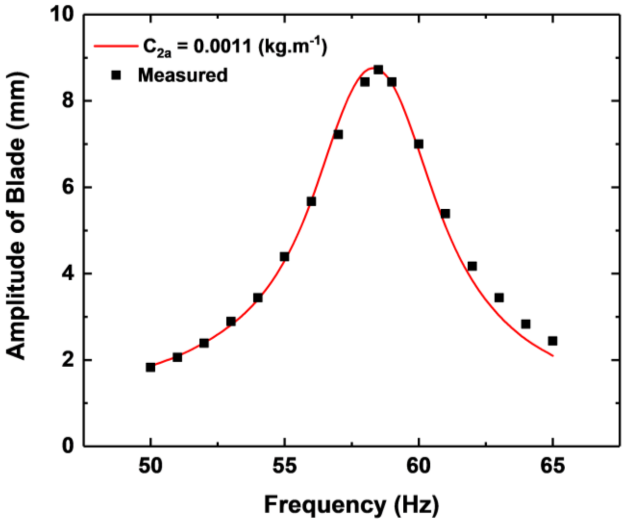

Figure 2.11 A representative result showing the measured vibration amplitude at the blade tip as a function of the excitation frequency (the black symbols) and the fit with our mechanical model (the solid line).

Figure 2.12 shows the experimentally measured and predicted power dissipation for a piezoelectric fan operating near its first resonance frequency. Also shown is the power dissipation in the actuator, which is obtained from a nominally identical piezoelectric fan but with its blade cut off. The applied voltage amplitude is 80 V.

Away from the resonance, the vibration amplitude of the blade tip is small. The power dissipation in the piezoelectric fan is then dominated by the mechanical hysteresis and dielectric loss in the actuator.

In contrast, at or near the resonance frequency (58 Hz), there is a peak in the power dissipation for the piezoelectric fan. The difference between the piezoelectric fan and the actuator (without the blade) can be accounted for by the airflow power, P_{flow}. It is this portion of the power dissipation that should correlate with the heat transfer performance. The total power dissipation predicted using Eq. (2.8) with independently determined parameters matches the experimental data well.

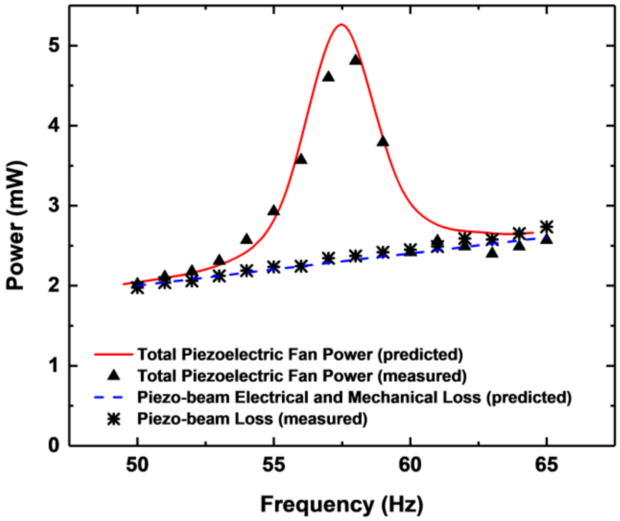

Figure 2.12 Power dissipation in a piezoelectric fan and in a bare actuator (with the blade cut off). The measured powers (triangles) peak at the resonance frequency of the fan (~58 Hz). The predicted powers are also shown as the red solid line and the blue dashed line.

2.4.2 Heat transfer performance and power dissipation

To examine relationships between the heat transfer performance of piezoelectric fans and the power dissipation, specifically the airflow power, we perform several sets of experiments using piezoelectric fans of different geometric parameters (Table 2.1).

Figure 2.13 shows the Nusselt numbers ($Nu_{L,\text{total}} = h_{\text{total}}L/k_{\text{air}}$) obtained from all the piezoelectric fans and the operating conditions summarized in Table 2.1. Here, L is the length of the heated surface and k_{air} is the thermal conductivity of air. The results from these piezoelectric fans and operating conditions correlate reasonably well with the airflow power.

At first glance, this result appears to suggest that changing the geometric parameters of the blade (length, thickness, and center of mass) has a limited effect on the power efficiency of the fans. That is, any enhancement in the heat transfer coefficient may need to be accompanied by corresponding increase in power dissipation. This is somewhat misleading, however, as the total power dissipation also includes contributions from the dielectric loss and mechanical loss as discussed in Section 3.

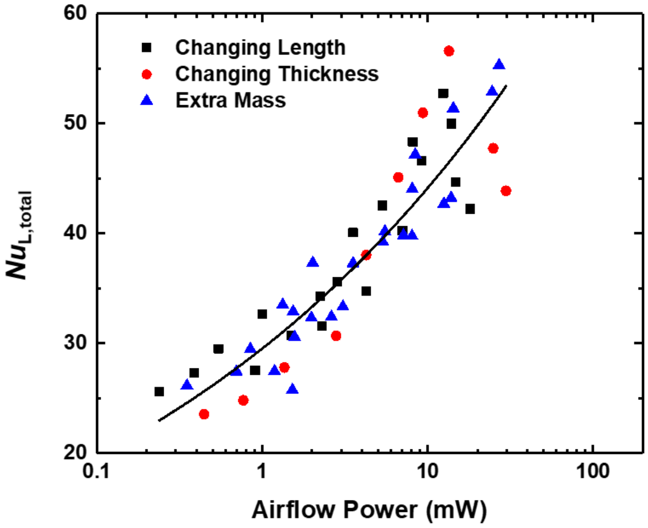

Figure 2.13 The Nusselt number as a function of the airflow power for all the piezoelectric fans and operating conditions used in the present study. The solid line is a guide to the eye to illustrate a positive correlation between the heat transfer coefficient and the airflow power. The general relation between $Nu_{L,total}$ and Re_L can be indirectly approximated as $Nu_{L,total} = 0.98\ Re_L^{0.525}$.

The data shown in figure 2.13 can be fitted using an empirical relation of the form

$$Nu_{L,total} \sim P_{flow}{}^{0.175} \tag{2.9}$$

Using Eq. (2.6) for P_{flow} and the Reynolds number defined in terms of the tip velocity u_{tip}

$$Re_L = \frac{u_{tip}\, L}{\nu}, \tag{2.10}$$

we can re-write the above correlation in terms of the two dimensionless parameters:

$$Nu_{L,total} \sim Re_L^{0.525} \tag{2.11}$$

The above correlation is consistent with those reported in [61] and [62] for heat transfer performance of jets impinging on a flat surface. These earlier correlations reveal similar dependence of $Nu_{\mathrm{L,total}}$ on Re_{L}, namely $Nu_{\mathrm{L,total}} \sim Re_{\mathrm{L}}^{\ a}$ with $0.4 < a < 0.8$.

Note that the experimental data from piezoelectric fans of different blade thicknesses deviate more from the general trend than those from the other fans. We suspect that this larger deviation may have to do with additional structural damping in the thicker blades. Blades of different thicknesses were prepared by bonding different layers of Kapton sheets together. This may have led to different degrees of structural damping in different blades, which was not taken into account in our model for power dissipation.

To further help elucidate the physical origin of the airflow power, we perform a separate set of experiments where we measure the normal force exerted on an opposing flat surface by airflows generated by the piezoelectric fan. The opposing surface is located in the same relative orientation with respect to and at the same distance from the fan as our heated surface. The general trend once again can be captured in terms of the Reynolds number (shown in figure 2.14):

$$F \sim Re_L^{2.36} \tag{2.12}$$

This is again consistent with a correlation reported earlier for the thrust force exerted by piezoelectric fans, $F \sim A_{blade}^{\ 2.38} f^{\ 2.19}$ [35].

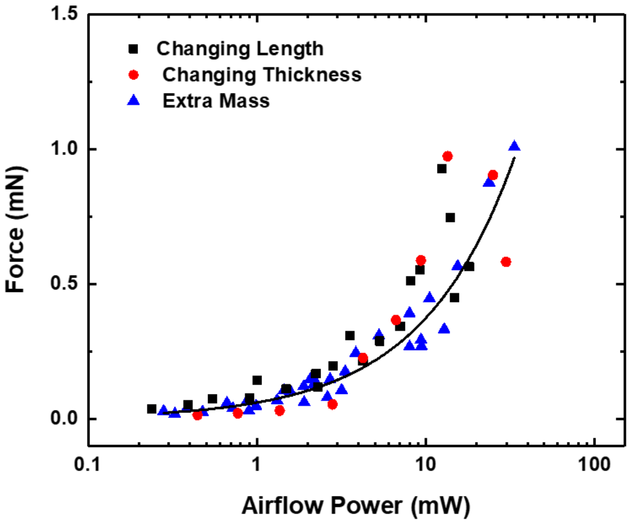

Figure 2.14 The aerodynamic force exerted on an opposing surface by a piezoelectric fan as a function of the airflow power. The solid line is a guide to the eye to illustrate a positive correlation between the aerodynamic force and the airflow power. The general relation between nondimensionalized force, F/F', where $F' = \frac{1}{2} \rho_{air} u_{tip}^2 L^2$, and Re_L can be indirectly approximated as $F/F' = 8.9 \times 10^{-2} Re_L^{0.36}$.

Figure 2.15 shows the airflow power as a function of the total power dissipation. For our particular set of fans, the airflow power accounts for approximately 30 to 80% of the total power dissipation. This fraction generally increases with increasing vibration frequencies because the airflow power exhibits stronger frequency-dependence than the dielectric and mechanical losses. Piezoelectric fans with longer blades, for example, can have worse overall power efficiencies than fans of shorter blades. However, merely trying to design a piezoelectric fan with a highest resonant frequency may lead to excessive reduction in the vibration amplitude of the blade tip, which can be detrimental to cooling performance.

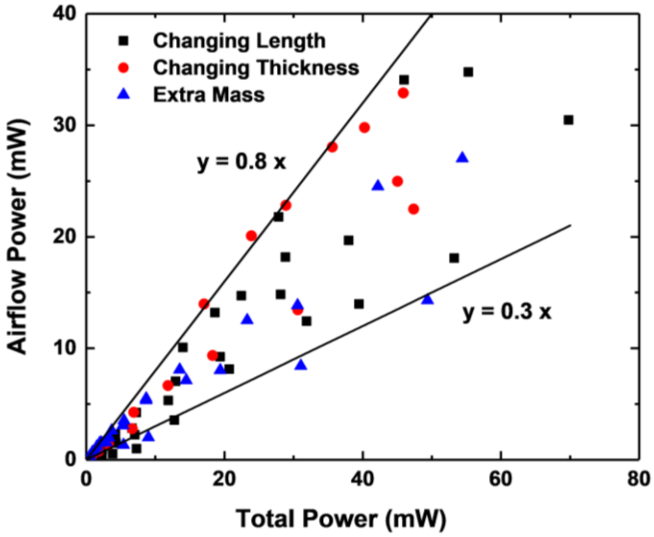

Figure 2.15 Airflow power vs. total power consumption. Airflow power accounts for 30 to 80% of the total power dissipation in the piezoelectric fan.

A useful figure of merit for characterizing the power efficiency of piezoelectric fans is the ratio between the flow power P_{flow} and the total power P_{total}. This ratio is represented as the slope in figure 2.15. The ratio, hereafter referred to as the cooling power efficiency, can be expressed using parameters from our power dissipation model as

$$\frac{P_{flow}}{P_{total}} = \frac{\frac{32\pi^2}{3} C_{2a} |A_{blade}|^3 f^3}{4H|A_{actuator}| f + V_{rms}^2\, Re(Y) + \frac{32\pi^2}{3} C_{2a} |A_{blade}|^3 f^3} \tag{2.13}$$

Since the airflow power has the strongest frequency dependence, we expect the cooling power efficiency increases as the frequency increases. To help explore the bias voltage amplitude dependence of the cooling power efficiency, we represent those parameters in the above equation that depend on the bias voltage amplitude V as

$$A_{actuator} = C_{act}V \tag{2.14}$$

$$A_{blade} = C_{blade}\, A_{actuator} = (C_{blade}\, C_{act})V \tag{2.15}$$

$$H = C_H V \tag{2.16}$$

$$Re(Y) = C_Y V^2 f \tag{2.17}$$

$$V_{rms} = \frac{\sqrt{2}}{2}V \tag{2.18}$$

The coefficients C_{act}, C_{blade}, C_{H} and C_{Y} are determined either experimentally or obtained from literature. Note that parameters A_{actuator}, A_{blade}, C_{H} and tan δ (via Y) in Eqs. (2.14) – (2.17) are assumed to be independent of the actuation frequency under the conditions of our experiments [48].

The cooling power efficiency can then be rewritten as

$$\frac{P_{flow}}{P_{total}} = \frac{\overbrace{\left[\frac{32\pi^2}{3}C_{2a}{C_{blade}}^3{C_{act}}^3\right]}^{\alpha}V^3f^3}{\underbrace{[4C_H C_{act}]}_{\beta}V^2f + \underbrace{\left[\frac{C_Y}{2}\right]}_{\gamma}V^4f + \underbrace{\left[\frac{32\pi^2}{3}C_{2a}{C_{blade}}^3{C_{act}}^3\right]}_{\alpha}V^3f^3} \tag{2.19}$$

Here, the parameter group α captures the aerodynamic and geometrical properties of the blade, the group β mechanical loss in the actuator, and the group γ dielectric loss in the actuator.

Figure 2.16 shows the cooling power efficiency as a function of the bias voltage amplitude V for five different actuation frequencies. For each actuation frequency, the cooling power efficiency exhibits a peak value. To the left of these peaks, the blade vibration amplitude and the air flow power are small. The mechanical hysteresis loss, which scales as V^2, is the dominant source of power dissipation in this region. Since the air flow power scales as V^3, the cooling power efficiency first increases with increasing bias voltage amplitudes. As the bias voltage amplitude is increased further, the dielectric loss, which scales as V^4, becomes more significant. The increase in the air flow power cannot keep up with the increase in the dielectric loss and the cooling power efficiency begins to decrease with further increase in the bias voltage amplitude. At still higher values of V, the amplitude of blade vibration tends to saturate while the airflow power stays almost constant, leading to a further gradual decrease in the cooling power efficiency. This decrease is more pronounced at lower actuation frequencies.

The bias voltage amplitude where the maximum cooling power efficiency occurs is mathematically obtained by equating the first derivative of Eq. (2.19) with respect to V to zero:

$$V_{max} = \sqrt{\frac{\beta}{\gamma}} \tag{2.20}$$

For the piezoelectric actuators used in the present study, we estimate $V_{\max}$ to be 101 V. The data shown in figure 2.15 with the high cooling power efficiencies (as high as 0.8) are obtained with bias voltages 90 ~ 120 V, consistent with this value of $V_{\max}$. Note that this voltage amplitude only depends on β and γ, which in turn depend only on the geometry and material properties of the actuator and not those of the blade or actuation frequency. Although $V_{\max}$ itself is a function only of the actuator characteristics, the value of the maximum cooling power efficiency is a function of the blade characteristics and actuation frequency:

$$\left.\frac{P_{flow}}{P_{total}}\right)_{max} = \frac{\alpha\left(\frac{\beta}{\gamma}\right)^{3/2} f^3}{2\frac{\beta^2}{\gamma} f + \alpha\left(\frac{\beta}{\gamma}\right)^{3/2} f^3} \tag{2.21}$$

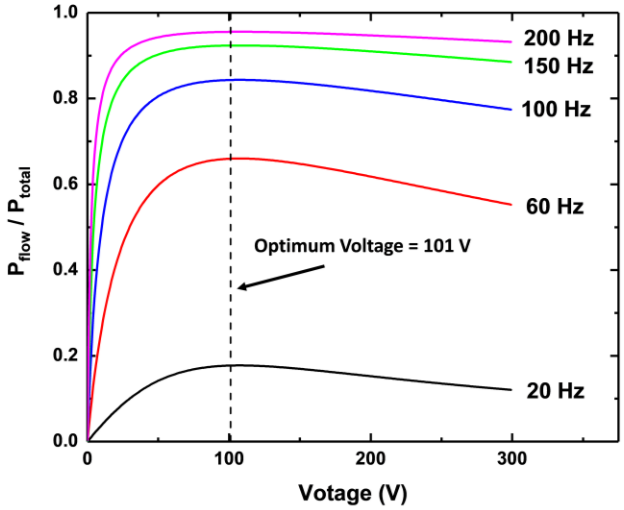

Figure 2.16 The cooling power efficiency obtained from our model as a function of the bias voltage amplitude at different frequencies. Note that the voltage amplitude that corresponds to the peaks in the cooling power efficiency does not change with the frequency over the range considered in the present work.

In designing or selecting piezoelectric fans, one must consider both the power efficiency and the absolute heat transfer performance, which we have shown to correlate with the air flow power. To facilitate such design processes, we next present an approximate relation between the air flow power and the geometric parameters of fan blades.

We first rewrite Eq. (2.6) explicitly in terms of the blade parameters. The resonance frequency is first expressed as [59], [60]:

$$f_{res.} \sim \left(\frac{E}{\rho_{blade}}\right)^{0.5} \frac{t_b}{l_b^2} \tag{2.22}$$

The aerodynamic damping coefficient, $C_{2,a}$ is linearly proportional to the area of the blade, *lw* [58]:

$$C_{2,a} \sim \rho_{air}\, l_b w_b \tag{2.23}$$

The amplitude of the blade is linearly dependent on the amplitude of the actuator tip (Eq. (2.15)). From the experimental data and mathematical model, we relate C_{blade} with the mass densities:

$$C_{blade} \sim \left(\frac{\rho}{\rho_{air}}\right)^{0.5} \tag{2.24}$$

Substituting Eqs. (2.22) – (2.25) into Eq. (6), we obtain:

$$P_{flow} = C^{*} \frac{E^{1.5}}{{\rho_{air}}^{0.5}} \left\{ \frac{w_b\, t_b^3}{l_b^5} (C_{act} V)^3 \right\} \tag{2.25}$$

where C^* is a proportionality constant.

We compare the air flow powers we extract from the experimental data with the predicted trend from Eq. (2.25) to determine the proportionality constant, $C^{\,*}$, for our piezoelectric fans. The experimental values and the fit are shown in figure 2.17. Given that the air flow power is obtained indirectly and has appreciable uncertainty, we consider the quality of the fit to be overall reasonable. We note that the model represented in Eq. (2.25) does not account for possible non-linearity in the mechanical behavior of blades and their structural damping.

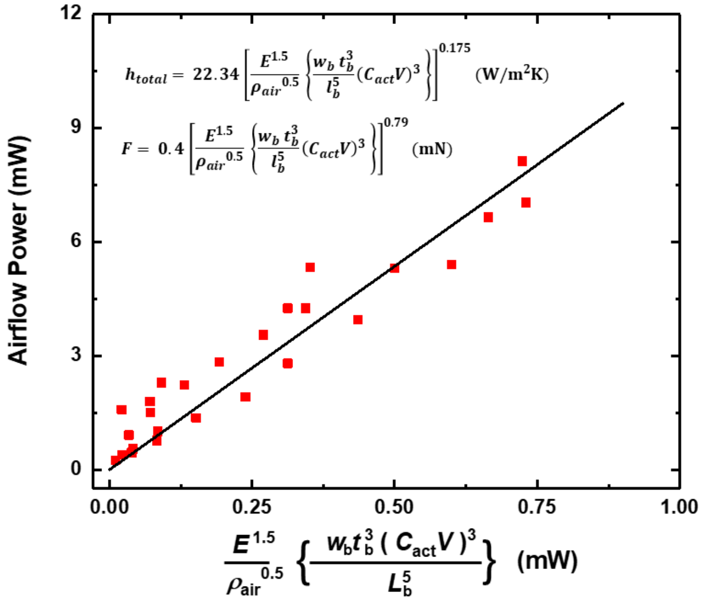

Figure 2.17 A linear fit to the air flow power obtained from the experiments (red symbols) to determine the proportionality constant C^* (10.7) in Eq. (2.25). The average deviation between the data and the curve fit is approximately 25% of the mean value of the airflow power over the range considered. Approximate analytic expressions for the heat transfer coefficient and the normal aerodynamic force on an opposing surface may be obtained in terms of the geometrical parameters of the blades by substituting Eq. (2.25) into the least-square fits to the experimental data: $Nu_{L,\text{total}} = 29.51\,P^{0.175}$ and $F = 0.062\,P^{0.79}$ (mN). The average deviation between the data and the fit is approximately 10% (for the heat transfer coefficient) and 20% (for the aerodynamic force) of the respective mean value.

2.5 Summary

Optimizing the power efficiency of piezoelectric fans requires a deeper understanding of the mechanisms involved in their power consumption. In this chapter, we reported a combined experimental and modeling study to help elucidate different power dissipation mechanisms in piezoelectric fans and obtain an optimal operating condition for maximum power efficiency. We measured power dissipation in fans of different blade lengths, thicknesses and mass distributions as functions of the frequency and magnitude of sinusoidal bias voltages. Models that account for dielectric loss, mechanical hysteresis, and aerodynamic damping from generated air flows were used to partition power dissipated in the fans.

Our data and model analyses showed that the mechanical hysteresis loss and the dielectric loss are dominant sources of parasitic power dissipation in the actuators. Our measurements showed that 30 to 80% of the total power consumed stem for generated air flows. The experimentally determined average heat transfer coefficients and aerodynamic thrust forces on flat surfaces correlate generally well with the air flow power, further verifying the fluid dynamics origin of this portion of dissipated power.

We introduced the power ratio as a useful indicator of the portion of total power that is used to generate air flows and thereby contributes to convective cooling. Using our mechanical models, we investigated the frequency and voltage dependence of the power ratio and determined an optimal bias voltage amplitude that maximizes the power ratio, and hence power efficiency, by balancing the mechanical hysteresis loss and the dielectric loss with respect to the air flow power.

Finally, we related the air flow power and hence heat transfer performance to the blade's geometrical parameters to assist overall design or selection of fan blades.

The results presented in this chapter reveal, for the first time, the importance of the dissipative aerodynamic forces acting on the oscillating blade (and their associated power consumption) in the overall performance of the fans. To improve our understanding of the operation of piezoelectric fans and facilitate their more systematic optimization, a better understanding of the fluid dynamics and vortex behavior of these fans is required. In the next two chapters, we aim to perform a deep study on the two-dimensional and three-dimensional properties of the downstream flows created by piezoelectric fans.

Chapter 3. Vortex regimes downstream of piezoelectric fans

3.1 Background

In the previous chapter, it was shown that the flow power resulting from the aerodynamic forces acting on the oscillating plate constitutes a considerable portion of the total power consumption within a piezoelectric fan. In this chapter, we perform a deeper investigation of the fluid dynamic mechanisms that convert the oscillatory motion of the plate to a streamwise flow. We do this through a comprehensive study of the fluid-solid interactions at the trailing edge of the plates and the resulting vortex patterns in the wake.

Interactions between vibrating cantilever plates and surrounding fluids have been the subject of many studies. These structures have continued to gain attention due to a variety of applications, such as piezoelectric fans for electronics cooling [12], [63], [64], electrostatic [65] and electromagnetic [66] fluid accelerators, energy harvesting using vortex induced vibrations [67]–[69], micro air vehicles (MAVs) [70], ionic polymer metal composites (IPMCs) [71]–[74], and micro-mixers and aerosol collectors [75]. Applications that require net flow generation, such as piezoelectric fans, rely primarily on vortex generation at the trailing edges. Understanding the mechanisms and patterns of vortex generation and propagation is critical for the systematic design and optimization of vibrating plates in these applications.

Kim *et al.* [31] performed a comprehensive study on the mechanisms of vortex generation and propagation in piezoelectric fans. They revealed phase-resolved vorticity contours, trajectory and circulation of the vortex pairs generated in each cycle of oscillations. However, this study considered a limited range of amplitudes and a fixed frequency, and therefore may not be representative of all piezoelectric fans' operational range, especially, because vortex dynamics are very nonlinear and unpredictable in nature. Shrestha et al. [36], in fact, observed several lateral vortex regimes that directly affect the forces on the plate. The presence of similar vortex patterns in the wake of the pitching plate (downstream the trailing edge), however, is missing in the literature.

In the present chapter, we investigate wake vortex regimes for thin cantilever plates of systematically varied geometries, resonant frequencies and amplitudes oscillating in quiescent air and examine their correlation with downstream flow generation. The rest of the chapter is organized as follows. In Section 3.2 we describe the parameters and experimental setup used in the present study. Section 3.3 provides the detailed description of the geometry, time-space discretization, solver properties and validity of the numerical simulations reported in this study. Section 3.4 contains the results and discussions regarding the vortex patterns observed in the experiments and numerical studies. Summary and conclusions are presented in Section 3.5.

3.2 Experimental setup

The vibration characteristics of the cantilevers are described by their frequency, *f*, and amplitude, *A*. The tip characteristic velocity is given as $u_{\text{tip}} = fA$. The main length scale in the problem is the length of the cantilever, L_c. The aspect ratio, w_c/L_c, and the thickness of the plates only have secondary effects on the vortex generation and propagation along the centerline. We introduce two independent dimensionless parameters: a normalized amplitude, α and an oscillatory Reynolds number for the cantilever, Re_c:

$$\alpha = \frac{A}{L_c} \tag{3.1}$$

$$Re_c = \frac{u_{tip}\, L_c}{\nu} = \frac{f\, A\, L_c}{\nu} \tag{3.2}$$

where v is the kinematic viscosity of the fluid. We refer to Re_c simply as the Reynolds number throughout the rest of the paper. It is sometimes convenient to remove the amplitude in one of the dimensionless parameters. This can be done by using the ratio Re_c/α

$$\frac{Re_c}{\alpha} = \frac{f\, L_c^{\,2}}{\nu} \tag{3.3}$$

As we are dealing with oscillating plates in an otherwise quiescent fluid, the Strouhal number cannot be defined.

A piezoelectric actuator (Steminc Inc., SMPF61W20F50) is employed in the present study to oscillate cantilevers at their resonance frequencies. The piezoelectric actuator consists of two 185 μm-thick piezoelectric ceramic films ($Pb\,(Zr_{0.53}Ti_{0.47})\,O_3$; PZT-4) and a 142 μm-thick copper shim sandwiched in between. It is 20 mm wide and 23 mm long (figure 3.1a). Flexible blades of different materials and geometries are made in-house and attached to the actuator using cyanoacrylate glue. Table 3.1 lists the geometric parameters of the blades along with the resonance frequencies, f, and the ranges of vibrational amplitudes, A, used in the present study.

A function generator (Model 33220A, Agilent) is used to generate sinusoidal voltage waves of amplitude 0.05 V – 2 V, which are then amplified by a factor of 100 using a high-voltage amplifier (Model PZD700A, TREK) before being fed to the actuator (figure 3.1c). The vibration amplitudes are measured optically with an uncertainty of approximately 10 μm, less than 5% of the minimum amplitude used in this study. Different resonance frequencies for the same cantilever are obtained by changing the mass distribution using a method reported in a previous study [76]. We verified that the different cantilevers used exhibit similar modal shapes at different frequencies (figure 3.1b).

The PIV setup (figure 3.1c) comprises a 500 mW continuous wave laser (Hercules, LASERGLOW Technologies) with a wavelength of 532 nm. The laser beam is shaped into a light sheet using a cylindrical lens (plano-concave lens, f = -3.9 mm, ThorLabs). We use a high-speed camera (Phantom VEO-640L) capable of recording 16-bit, 4-megapixel images to capture the motion of particles suspended in the air. The frame rate is chosen such that at least 100 frames are captured per full period of the oscillations. A shutter speed of 80 μs is considered adequate for eliminating the effects of motion blur in these experiments.

PIV experiments are conducted in a sealed box made of transparent acrylic plates (30 cm × 20 cm × 8 cm), large enough to reduce interference from the side walls [77]. Seeding particles are generated by heating a solution of water and glycerin (30% glycerin in volume). They are allowed to settle for about a minute before conducting any recording to minimize initial disturbance from previous experiments. The particle motions due to buoyancy are measured separately in the absence of an oscillating plate and deducted from velocity fields.

An open-source software package [78], [79] is used to analyze the captured video images. This software utilizes the Advanced Discrete Fourier Transform technique in which smaller sub areas of two successive frames are cross-correlated to obtain the direction and magnitude of particles' displacements in the sub-areas. The calculated velocity fields are next post-processed by manually filtering the outlier data and replacing them with interpolated equivalents in areas where improper lighting condition leads to inaccurate displacement vectors. An algorithm based on penalized least squares method [80] is employed to reduce the noise in the flow fields.

The PIV setup and image processing procedure are validated using several benchmarks in [81]. An uncertainty of 0.14 pixel is estimated for the displacement vectors, which translates into an uncertainty in velocity of 0.016 m/s in our experiments.

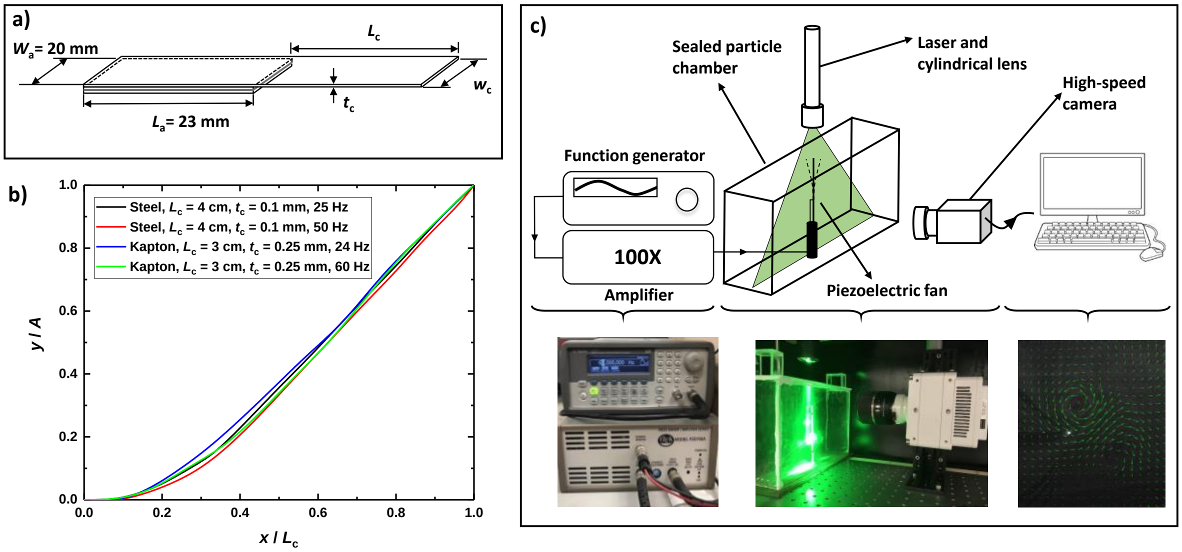

Figure 3.1 (a) Schematic of the piezoelectric actuator and the attached blade, forming a vibrating cantilever plate (b) normalized modal shape of the cantilevers with blades of different materials and resonance frequencies (c) schematic of the PIV visualization setup.

Table 3.1 Characteristics of the cantilevers used in the experiments and the corresponding oscillatory Reynolds numbers Re_c.

Material	**t_c (mm)**	**L_c (mm)**	**w_c (mm)**	**f (Hz)**	**A (mm)**	**$Re_c = L_c f A/\nu$**
steel	0.1	15	30	90	0.18 - 2	16 - 172
	0.1	15**	30	155**	0.26 - 2.5	39 – 371
Kapton	0.127	20	30	72	0.3 - 4.6	28 – 422
	0.127	20	30	96	0.5 - 2	61 – 245
	0.127	30*	30	20*	0.3 - 3.6	11 – 138
	0.127	30	30	29	0.3 - 3.9	17 – 216
	0.127	30**	30	39**	0.3 - 4.2	22 – 313
polyester	0.03	20	30	21	0.5 - 2.9	13 – 78
	0.03	20	30	30	0.4 - 3	15.3 - 114
	0.03	20*	30	45*	0.5 - 3.6	29 - 207

3.3 Numerical simulations

We perform two-dimensional numerical simulations using a commercial computational fluid dynamics package (Ansys CFX) to help interpret our experimental results. We use the Immersed Boundary Method [82] to avoid computational overheads associated with re-meshing in moving mesh methods. Table 3.2 summarizes the flow conditions simulated. The flow field generated downstream of an oscillating cantilever plate is inherently three-dimensional and more complex than can be captured in a two-dimensional simulation [5], [34], [41], [83], [84]. However, the velocity field and vortex generation on the mid-plane normal to the cantilever (figure 3. 2a) can be approximated as two dimensional [31].

Table 3.2 Conditions used in numerical simulation

L_c (mm)	f (Hz)	A (mm)	$Re_c = L_c f A/\nu$
20	45	0.3 - 3.5	17 – 201
20	21	0.5 - 3.5	13 – 94
30	29	0.3 - 3.7	17 – 205
30	39	0.3 - 3.2	22 – 239

The simulation domain is chosen to be of size $3L_c \times L_c$ based on our experimental observations, such that it is large enough to capture vortex propagation while avoiding any complicating effect at the boundaries. To help resolve the details of vortex propagation, we use meshes of spatially varying sizes: $0.005L_c$ in a circle of a radius of $0.25L_c$ around the cantilever tip, $0.01L_c$ in an intermediate circle with a radius of $0.45L_c$, and $0.025L_c$ in the rest of the domain (figure 3.2b). To confirm mesh independence, a representative case is run 10 full cycles to reach stable flows [33] using different mesh sizes. Halving the mesh sizes from the chosen values results in less than 5% changes in the peak and average velocities at mid-points between two successive vortices propagating downstream while increasing the run time from 40 minutes to 50 hours on a workstation (Intel® Xeon® 2.30 GHz, 32 GB RAM).

An open boundary condition is specified on the outer walls of the simulation domain (figure 3.2a). This boundary condition allows fluid motion in both directions normal to the boundary. The relative pressure on the walls is specified as zero. The deformation of the cantilever plate is approximated as an immersed solid prescribed to rotate rigidly about a pivot point at its base; this simplification is justified by the predominance of the lowest-order vibration mode (see figure 3.1b). Our approximation is also reasonable because there is no incident flow from upstream to be affected by the details of the plate mounting. We also would like to emphasize that it is the motion at the trailing edge and its vicinity that are most important for establishing the wake profile and its thrust or drag signature. This is inherent, for example, in the asymptotic approach known as local interaction theory, in which the behavior of the boundary layers approaching the trailing edge is reconciled with the near wake. This led to a number of papers that espoused a “triple-deck” structure to reconcile these two regions (see [85]). Furthermore, in Lighthill’s elongated body theory in aquatic propulsion (see for instance [86]), all of the momentum generated by the intermediate motion along the body is canceled by reciprocal motions, except at the trailing edge.

The first-order upwind scheme is used for advection terms and the second-order backward Euler scheme is used in time to discretize the governing equations. For each numerical simulation, the time step is chosen such that the Courant number remains lower than one in computational cells.

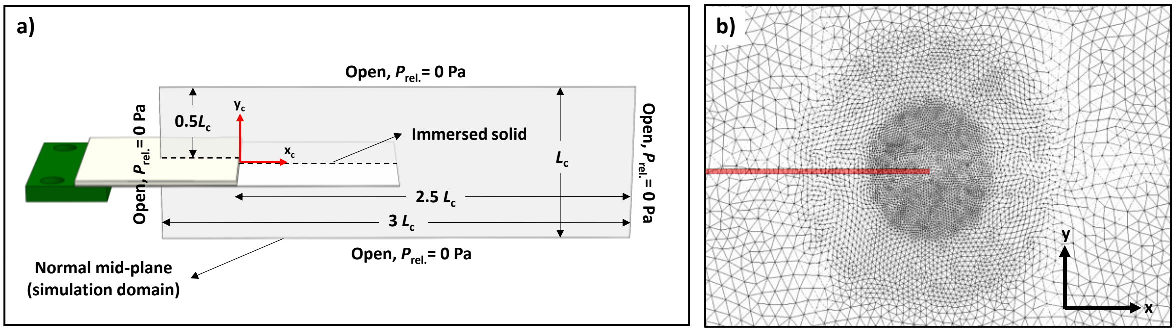

Figure 3.2 (a) Simulation domain (b) typical mesh used in the present study (images are not to scale).

3.4 Results and discussions

In pitching airfoils and oscillating cantilever plates, the entire vorticity originates in the boundary layer due to the no slip condition. In the presence of an external flow, the non-zero free stream modulates the development of the boundary layer and can facilitate vortex shedding from the leading edge or mid-body besides the trailing edge. The frequency of vortex shedding in this case is influenced by the free stream velocity and can be different from the frequency of the oscillations, creating complex vortex patterns in the wake of the oscillator (up to 16 vortices in a period at high freestream velocity and low oscillation frequencies reported in [25]). This mechanism is absent without the free stream and the frequency of vortex shedding is the same as the frequency of the oscillations, *f*. As a result, only two counter-rotating vortices in each cycle are shed from the trailing edge [31], [87]. Our observations from the PIV experiments identify three distinct regimes of vortex generation and propagation in the wake of an oscillating flat plate.

3.4.1 Non-propagating vortex regime

At low Reynolds numbers ($Re_c < 37$), counter-rotating vortices are generated at the tip during each cycle: a clockwise vortex in the up stroke and a counter-clockwise vortex in the down stroke. The vortices remain attached to the cantilever in this regime and do not propagate downstream. Each of these counter-rotating vortices lasts only approximately half a cycle and disappears with the generation of a next vortex. Only a single vortex is effectively visible at a given instant. Figure 3.3 shows the time sequence of vortex formation in a representative PIV experiment, and figure 3.4 depicts the corresponding numerical simulation results.

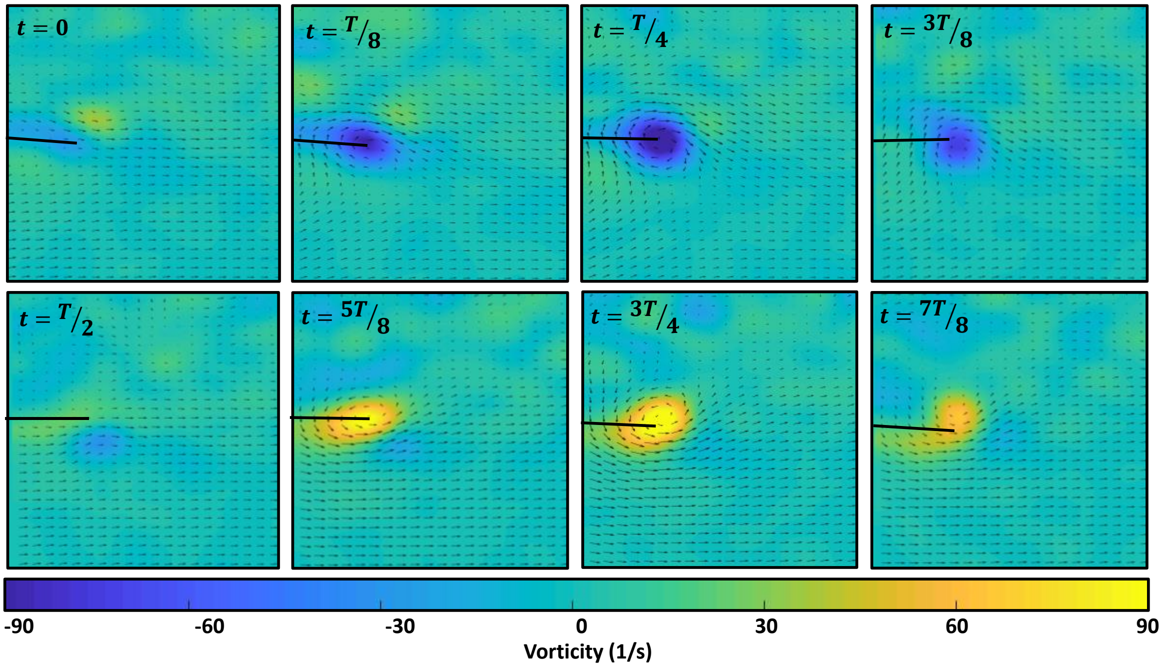

Figure 3.3 The time sequence of vortex generation and evolution over a full cycle for a representative case in the non-propagating regime: $Re_c = 25.12$ and $\alpha = 0.015$ ($L_c = 30$ mm, $f = 39$ Hz, $A = 0.453$ mm)

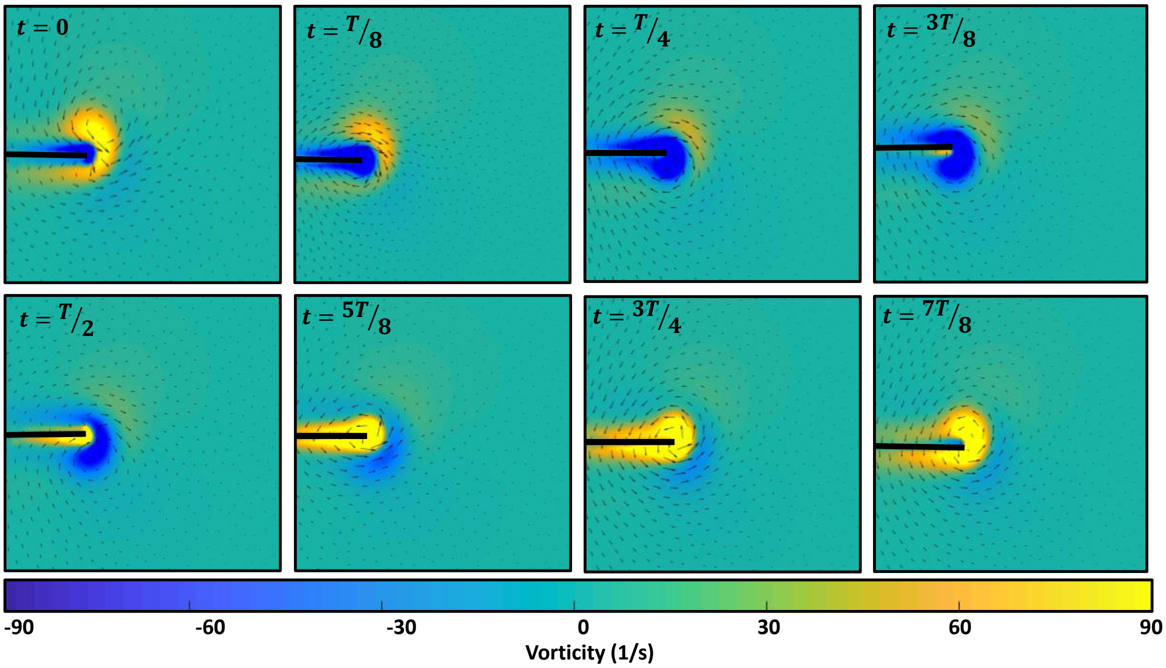

Figure 3.4 The time sequence of vortex generation and evolution obtained from numerical simulation under the conditions of the experiment shown in figure 3.3.

Our PIV experiments and numerical simulation show that, in this regime, forward flow generation due to a vortex attached on one side of the plate is essentially canceled out by reverse flow generation on the other side of the plate, leading to a negligible mean jet. The fluid motion along the length of the cantilever is essentially just upward or downward, and the velocity component in the forward direction is negligible. This is somewhat reminiscent of the flow regime observed by Shrestha *et al.* [36], where isolated attached vortices are observed at low amplitudes and frequencies with no significant convection on the lateral side of a vibrating cantilever. We previously observed poor performance of piezoelectric fans operating in this regime [88]. A similar behavior was reported in [89] for a piezoelectric fan operating at low amplitudes, where the so-called viscous streaming flows are created on the top and bottom of a thin oscillating plate.

3.4.2 Intermediate vortex regime

At moderate Reynolds numbers ($37 < Re_c < 70$), we observe a transitioning behavior, that is, vortices detach from the cantilever tip and propagate downstream. In this regime, a forward flow generated on one side of the plate overcomes a reverse flow generated on the opposite side, resulting in a net forward flow. The detached vortices, however, have low strength and their fast dissipation makes them very susceptible to deformation by subsequently generated vortices, significantly tilting the induced flow and limiting its spatial range. Due to the rapid dissipation of the vortices generated, two fully detached vortex are not observed at the same time. Figures 3.5 and 3.6 show the sequence of vortex shedding in this regime obtained from the PIV experiments and numerical simulation.

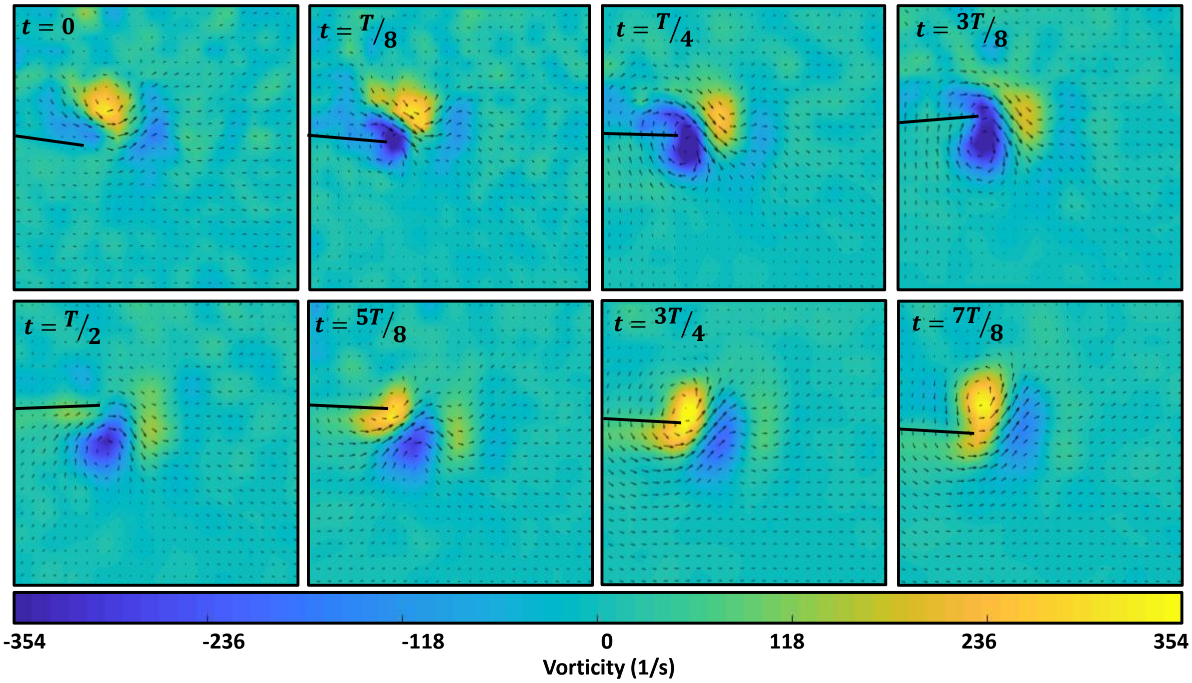

Figure 3.5 The time sequence of vortex generation and evolution over a full cycle for a representative experiment in the intermediate regime: $Re_c = 37.43$ and $\alpha = 0.022$ ($L_c = 30$ mm, $f = 29$ Hz, $A = 0.675$ mm)

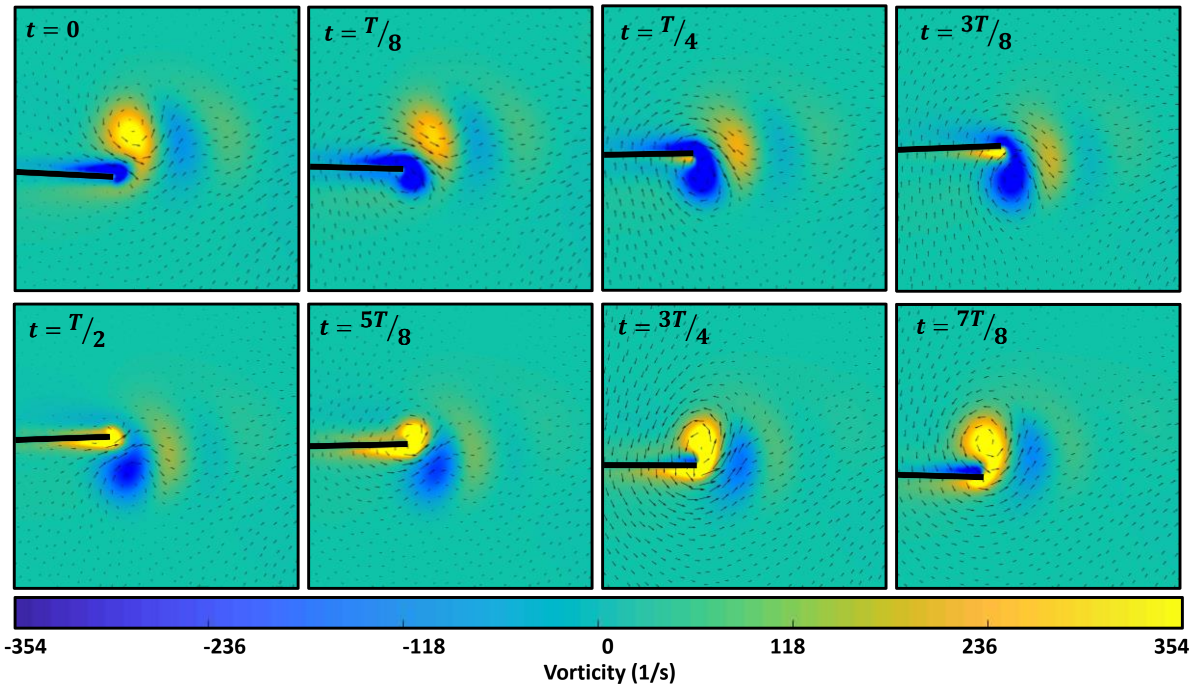

Figure 3.6 The time sequence of vortex generation and evolution obtained from numerical simulation corresponding to the conditions of the experiment shown in figure 3.5.

3.4.3 Propagating vortex regime

At still higher Reynolds numbers ($Re_c > 70$), we observe propagating vortices. In contrast to the intermediate regime, a vortex generated in this regime does not dissipate as completely after a half cycle and thus two counter-rotating vortices are observed propagating downstream. Figures 3.7 and 3.8 illustrate the vortex generation and propagation in this regime. Contrary to the non-propagating regime, the propagating vortices move completely to one side of the plate immediately upon creation. The forward velocity component on one side of a new vortex is augmented by its preceding vortex, and a high-velocity region is created in the space between the two adjacent vortices as they move downstream. These vortices resemble a thrust producing inverse Von Kármán vortex street observed in the wake of a pitching airfoil in [23], [25].

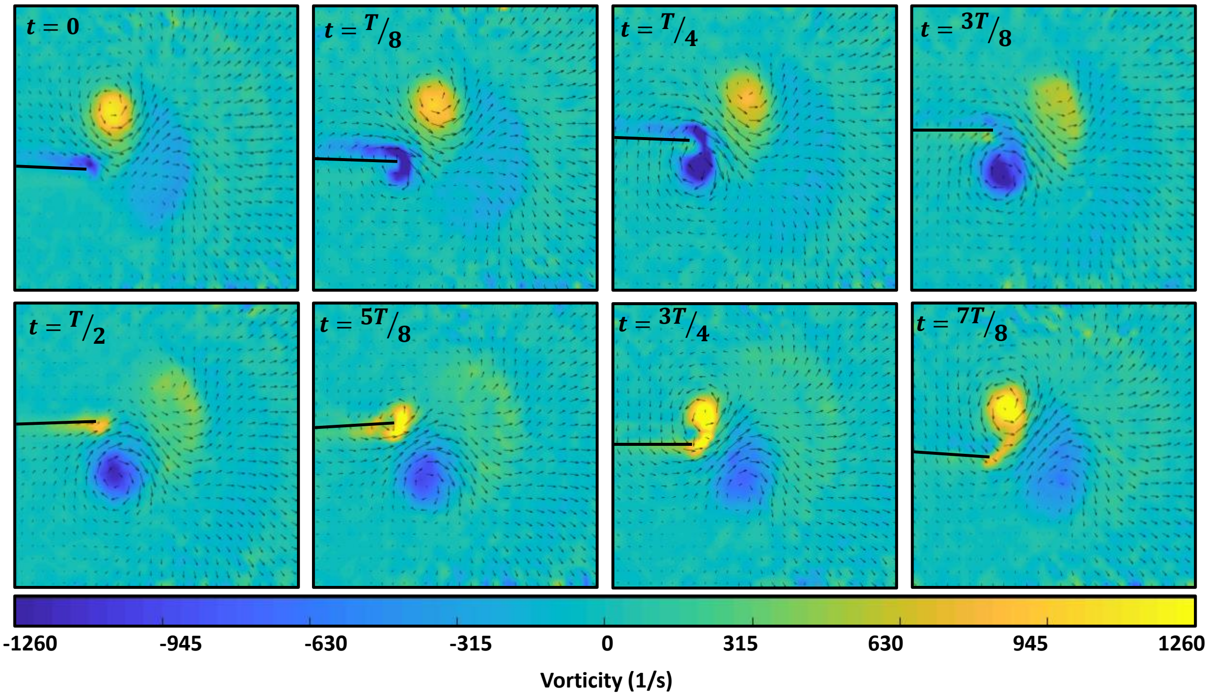

Figure 3.7 The time sequence of vortex generation and evolution over a full cycle for a representative experiment in the propagating regime: Re_c = 87 and α = 0.039 (L_c = 30 mm, f = 39 Hz, A = 1.2 mm)

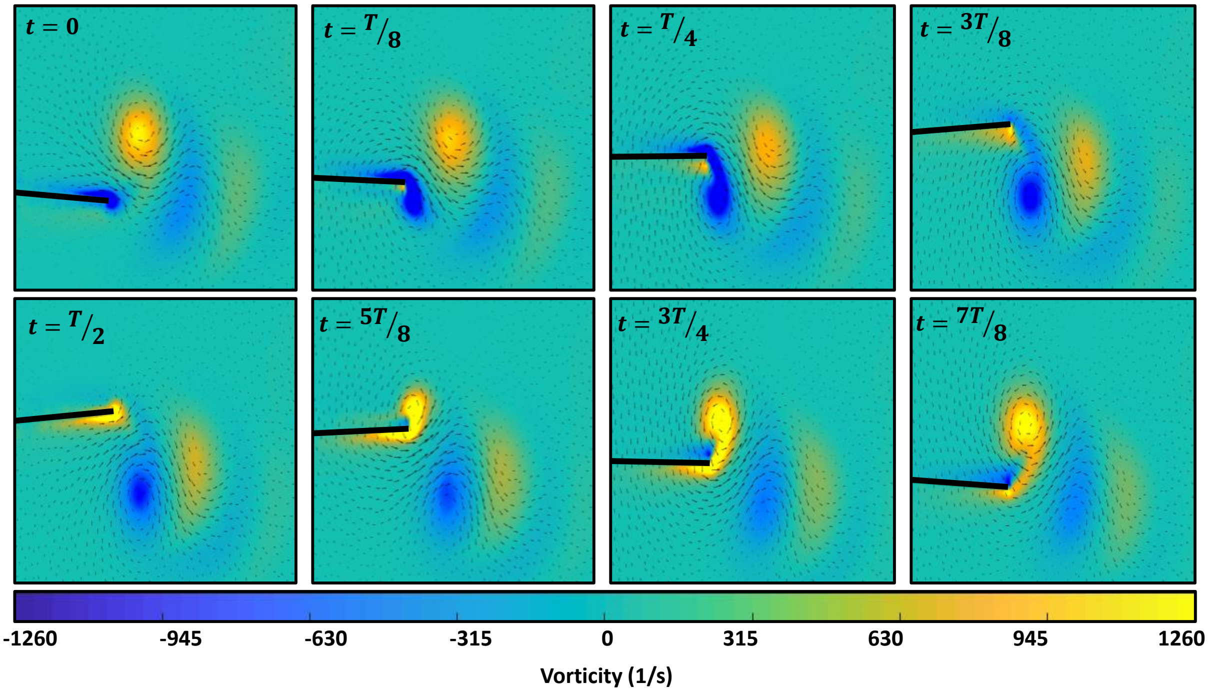

Figure 3.8 The time sequence of vortex generation and evolution obtained from numerical simulation under the conditions of the experiment shown in figure 3.7.

To further investigate vortex evolution in different regimes, we plot the ratio $\Gamma(t)/\Gamma_{\max}$ as a function of the normalized time t/T for a counter-clockwise vortex (figure 3.9a). Here, $\Gamma(t)$ is the circulation contained in the vortex core at time t, measured using the area integral of the vorticity in the vortex core, and $\Gamma_{\max}$ is the maximum circulation in a full cycle. The vortex core in a 2D flow field is identified using an algorithm reported in Graftieaux *et al.* [90]. The experimental results reported by Kim *et al.* [31] are also shown in the graph for comparison. In their work, the propagating regime at higher Reynolds numbers ($Re_c \sim 400$) was investigated.

Figure 3.9a shows that for all the cases investigated here, the vortex generation starts slightly earlier than the beginning of the vibration cycle. The circulation then increases almost linearly and peaks at $t/T \sim 0.25$, approximately when the tip passes its neutral position. After this point, the circulation contained in the vortex core starts to decay. The rate of decay is different for different regimes: the circulation decreases rapidly in the non-propagating regime, approaching nearly zero at half the cycle ($t/T \sim 0.5$), and the vortex effectively dissipates when the next vortex is formed. In the intermediate regime, the circulation decays immediately after reaching the peak, but at a lower rate. The circulation drops by approximately 40% at half the cycle and reaches 30% of its peak strength by the time a subsequent clock-wise vortex reaches its maximum circulation ($t/T \sim 0.75$). In the propagating regime, the circulation remains approximately constant after reaching the peak until it begins to gradually decrease at $t/T \sim 0.5$ - 0.6.

We can attribute the high decay rates in the non-propagating and intermediate regimes to vorticity annihilation, that is, the succession of oppositely-signed vortices canceling each other. This effect is more pronounced for these regimes because each generated vortex does not travel far from a subsequently generated vortex. Conversely, in the propagating regime, vorticity annihilation is less effective as vortices are further separated from each other. As a result, vortices are mostly influenced by vorticity diffusion rather than annihilation in the propagating regime. For a two-dimensional vortex in the presence of diffusion, such as Lamb – Oseen, the strength of the vortex core remains approximately constant because the core radius and the vorticity diffusion scale similarly with time ($\sim t^{1/2}$) [91]. This explains the flatness of the temporal profiles of $\Gamma(t)$ after the peak in the propagating regime. The circulation does decrease as a subsequent oppositely-signed vortex catches up eventually.

For flow conditions well within the non-propagating or propagating regime, the temporal circulation decay exhibits nearly universal behavior and is approximately independent of Re_c (the red symbols/curves and the blue symbols/curves in figure 3.9a). In contrast, as the flow condition approaches and crosses the non-propagating regime boundary ($Re_c \sim 37$), we observe rapid changes in the circulation decay curves as the Reynolds number is increased.

To help quantitatively compare the relative abruptness in these changes, we define the approximate linear decay rate of the normalized circulation. This decay rate is obtained as the negative slope of a fit to an approximately linear portion of each circulation decay curve from figure 3.9a at $t/T \geq 0.3$. Figure 3.9b illustrates the normalized decay rate thus obtained as a function of Re_c. Additional numerical simulations were performed right near the regime boundaries.

Figure 3.9b shows that the approximate linear decay rate is nearly constant away from the first regime boundary ($Re_c << 37$). It then decreases rapidly as the flow condition approaches and then crosses this regime boundary. Once the flow condition enters the intermediate regime, the approximate linear decay rate decreases much more gradually with increasing Reynolds numbers. We remind the reader that the intermediate regime does not represent a distinct primary flow regime, but rather a transition band within which hybrid vortical behavior and flow characteristics are observed. In the intermediate regime, vortices detach and propagate from the trailing edge but dissipate rather quickly. As we approach the boundary between the intermediate and propagating regimes (Re_c ~ 70), the decay rate once again undergoes more rapid changes but not as rapid as near the first regime boundary (Re_c ~ 37). For flow conditions well within the propagating regime (Re_c >> 70), the linear decay rate is approximately constant at a small value.

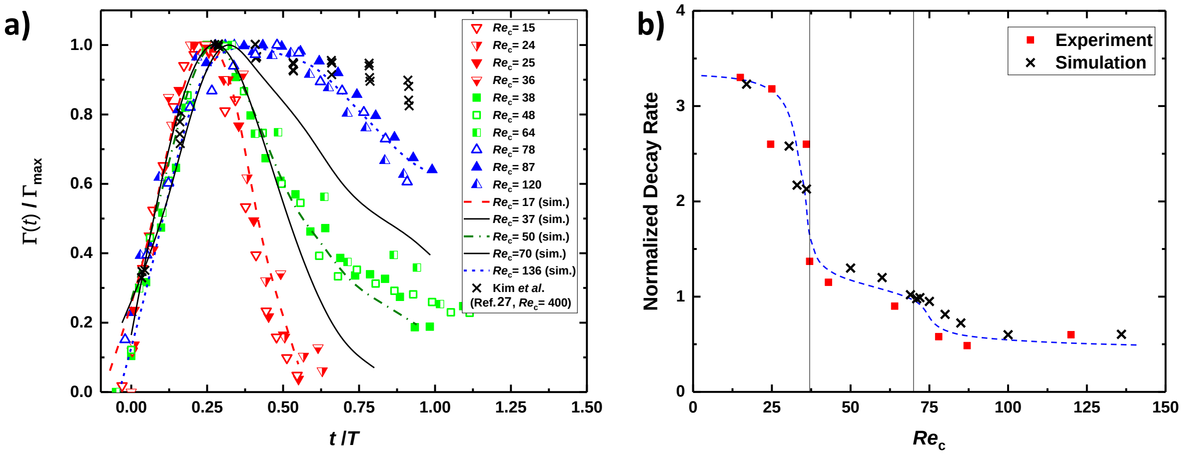

Figure 3.9 a) Normalized circulation in a cycle of oscillations. The data corresponding to regime boundaries are indicated by solid black lines. b) Approximate linear decay rate of the normalized circulation as a function of Re_c. The blue dashed line is a guide to the eye. The solid vertical lines correspond to the regime boundaries (Re_c = 37, 70).

3.4.4 Average velocity profiles and streamlines

The evolution of the vortices generated at the tip of a cantilever governs the velocity profile downstream of the cantilever plate. Figures 3.10a – 3.10c show the velocity profiles averaged over one cycle for each regime along with the associated streamlines.

In the non-propagating regime (figure 3.10a), the absence of vortex shedding and the presence of a single vortex at each half cycle results in a weak and short-range net flow generation in the forward direction. In the intermediate regime (figure 3.10b), the forward velocity is increased. In propagating regime (figure 3.10c), the presence of two vortices leads to a high-velocity region in the middle as the two counter-rotating vortices augment each other.

The curvature of the streamlines and their concentration in front of the cantilever is another indicator of the influence of vortex shedding on the surrounding fluid. Facci *et al*. [84] used the orientation and curvature of the streamlines at different cross-sections of their cantilever plates to investigate the aerodynamics loads in their three dimensional numerical simulations. As illustrated in figure 3.10a, the streamlines in the non-propagating regime are barely deformed and the streamlines in front of the plate are sparse compared with the other two cases. The transitioning nature of the intermediate regime can be recognized from the deformation of the streamlines around the cantilever tip in figure 3.10b, where the streamlines tend to form closed loops. In contrast, the streamlines around the tip of the cantilever form concentric lines under the influence of the propagating vortices in figure 3.10c. We believe that the slight asymmetry observed in figure 3.10 is caused by imperfections in the cantilever plates, such as slight misalignment in the mounting or built-in bias in cantilever deflections. These were also considered in [31], [33] as potential reasons for asymmetric velocity profiles in front of the cantilever.

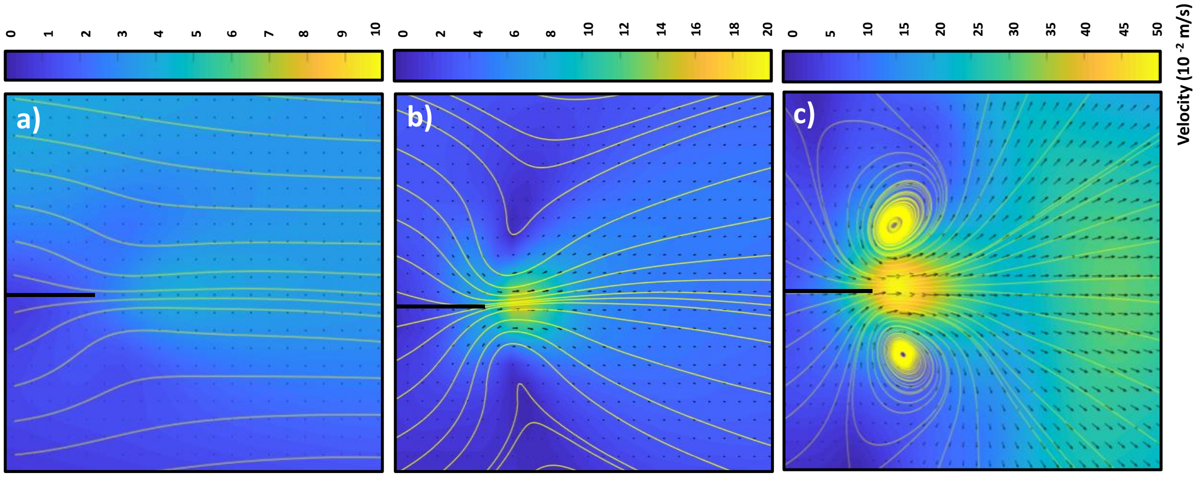

Figure 3.10 The average velocity field obtained from PIV experiments over one period of vibration and the corresponding stream lines for (a) the non-propagating (b) the intermediate and (c) the propagating regime shown in figures 3.3, 3.5 and 3.7, respectively. The velocity vectors have the same scale in the figures.

3.4.5 Vortex regime map and correlation with airflow generation

We construct the vortex regime map in the (α, Re_c/α) plane ($0 < \alpha < 0.2$ and $500 < Re_c/\alpha < 2500$) by systematically increasing the vibration amplitude while observing the resulting flow patterns. Corresponding results from our numerical simulations are also shown, but with a slight shift to the right to avoid overlap.

For each value of Re_c/α, the vortex pattern starts in the non-propagating regime. As the value of α is increased (corresponding to moving up in the regime map), the vortices start to detach from the cantilever tip and form the intermediate vortex pattern described earlier. As figure 3.11 suggests, this transition band is wider for smaller Re_c/α and narrower at larger Re_c/α. Increasing α further past the transition band, we observe the propagating vortex patterns. Two sets of data for $Re_c/\alpha = 1150$ and $Re_c/\alpha = 2200$ are obtained using different combinations of geometric and vibrational parameters indicated by * and ** in table 3.1. The vortex patterns observed in the numerical simulations agree well with the experiments. Our results show that the transition band is confined between the lines of constant Re_c ($Re_c = 37$ and $Re_c = 70$). The lines of constant Re_c were also observed to demark transition between the von Kármán and reverse von Kármán vortex regime in a previous study [25]. More specifically, they observed that the transition from von Kármán to reverse von Kármán in a non-zero freestream velocity medium around a pitching airfoil takes place at a constant tip characteristic velocity *Af* for a fixed cord length. Shrestha *et al.* [36] reported a critical value of $Re_c \sim 21$ for the transition from the symmetric to asymmetric vortex regime for the lateral vortex generation of a submerged flat cantilever plate in water.

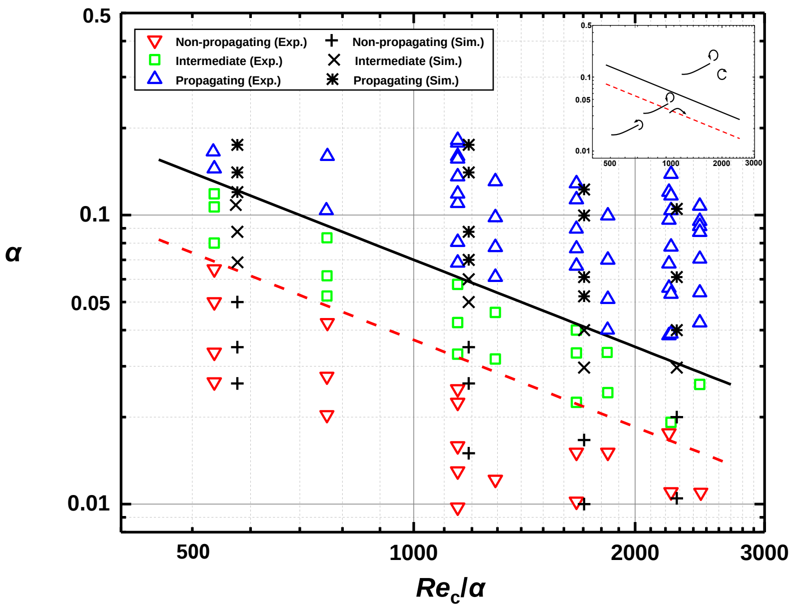

Figure 3.11 The vortex regime map. Separating lines of constant Re_c are shown with dashed (corresponding to $Re_c = 37$) and solid (corresponding to $Re_c = 70$) lines. Simulation data points are shown with a slight shift to the right to avoid overlap.

In many applications, such as cooling enhancement using piezoelectric fans, the average flow generation in the streamwise direction due to the cantilever vibrations is of great interest. To investigate the effect of the observed vortex patterns on downstream flow generation capability, we define a Reynolds number associated with the produced jet, Re_{jet}, as

$$Re_{jet} = \frac{\bar{u}_m \, A}{\nu} \tag{3.4}$$

where $\bar{u}_m$ is the momentum-averaged velocity of the jet, calculated from

$$\bar{u}_m = \left(\frac{\int_{-\infty}^{+\infty} \left(u(x_c, y)\right)^2 dy}{2A} \right)^{\frac{1}{2}} \tag{3.5}$$

Here, $u(x_c,y)$ is the velocity profile in front of the cantilever tip at $x = x_c$. Figure 3.12a schematically shows the procedure to obtain Re_{jet}. The location at which the velocity profile is taken has a minor influence on Re_{jet} because the fluid momentum is conserved along the x direction. In fact, our experimental results show that Re_{jet} remains essentially constant up to a distance equal to 4A downstream of the cantilever tip. Figure 3.12b shows the Re_{jet} obtained from the measured velocity profiles at different locations in front of the cantilever plate for each vortex pattern together with the Re_{jet} obtained from corresponding numerical simulations.

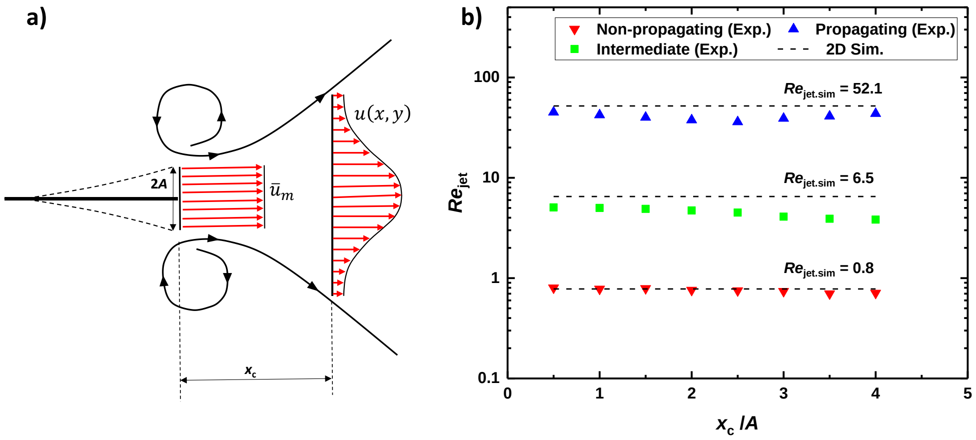

Figure 3.12 (a) Schematic illustrating the procedure of obtaining Re_{jet} in front of the cantilever tip (b) Re_{jet} as a function of the distance in the streamwise direction from the cantilever. The symbols and the black dashed lines represent the PIV results and corresponding numerical simulation results, respectively.

Figure 3.13 shows Re_{jet} as a function of Re_c. The different regimes are represented in different colors. In the propagating regime (blue), Re_{jet} increases almost linearly with Re_c with a slope of ~ 0.8. The non-propagating regime (red) shows a weaker dependence on Re_c, with a slope of ~ 0.1. These trends are consistent with the fact that vortex propagation is critical for long-range net forward flow generation. We indeed observed a precipitous drop in the performance of piezoelectric fans operating in the non-propagating regime [88]. These fans had a relatively high power consumption due to increased dielectric and hysteresis losses at high frequencies, but poor heat transfer performance as a result of weak net forward flow generation. Data in the intermediate regime do not follow a distinct trend but rather are scattered between the two trend lines. The data presented in this figure are also in-line with the findings of Peterson *et al.* [71], where inappreciable thrust was measured in IPMC cantilevers at Reynolds numbers below 60.

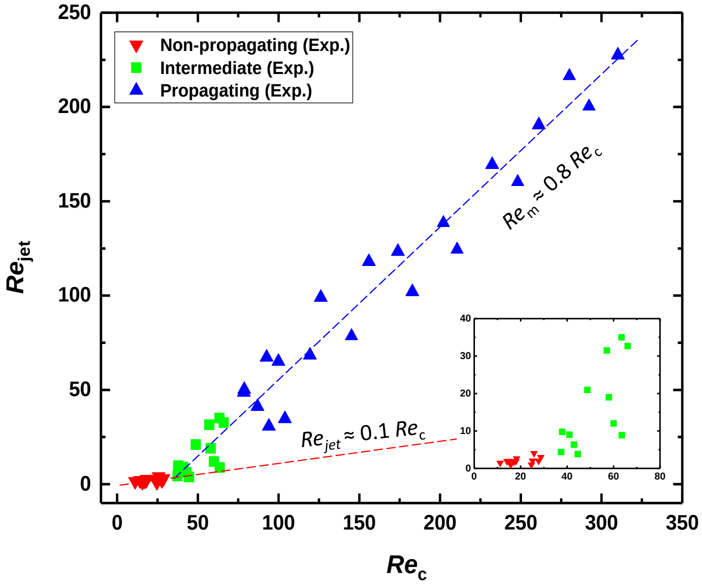

Figure 3.13 Jet Reynolds number, Re_{jet}, as a function of the oscillatory Reynolds number, Re_c. The red and blue dashed lines serve as guides to the eye, representing the linear trend of the data points in the non-propagating regime and the propagating regime, respectively.

3.4.6 Correlation between vortex regimes and thermal performance

To examine the relationships between the observed vortex propagation patterns and the power efficiency of the piezoelectric fans, we perform several sets of experiments using piezoelectric fans of different geometric parameters listed in Table 3.3.

The power consumption in a piezoelectric fan is categorized into three main sources: 1) dielectric loss 2) hysteresis loss 3) airflow power. The first two sources take place in the piezoelectric actuator as a result of the electrical and mechanical coupling. The airflow power represents the portion of power transferred to the surrounding air to generate flows and hence are more directly related to the cooling performance of the fan. We use the method we reported earlier [76] to extract the airflow power from the measured total power.

Table 3.3 Piezoelectric fan plate properties.

Control Variable	**Length, l_b (mm)**	**Thickness, t_b (mm)**	**Location of mass, d (mm)**	**Resonance Frequency, f (Hz)**	**Amplitude, A (mm)**
blade length	60 - 20	32	-	30 - 188	0.67 – 15
blade thickness	32	0.13 - 0.5	-	35 - 119	0.84 – 9
location of mass	32	0.26	0 (no extra mass) - 17	62 - 20.7	5 – 16

Figure 3.14a shows the total Nusselt numbers ($Nu_{\text{total}} = h_{\text{total}}L/k_{\text{air}}$) we obtain from all the piezoelectric fans and operating conditions summarized in Table 3.3. Here, L is the length of the heated surface and k_{air} is the thermal conductivity of air. Overall, the results from these piezoelectric fans and operating conditions correlate reasonably well with the airflow power. However, there exist cases (hollow symbols) that deviate from the general trend. These anomalous cases correspond to operations at high frequencies and low amplitudes.

To help further elucidate the physical origin of the anomalous behavior in the heat transfer performance at different airflow powers, we perform a separate set of experiments where we measure the normal force exerted on an opposing flat surface by airflows generated by the piezoelectric fan. The opposing surface is located in the same relative orientation with respect to and at the same distance from the fan as our heated surface. Similar anomalous behavior is observed for the normal force (figure 3.14b), providing further evidence to the fluid mechanical origin of the anomaly.

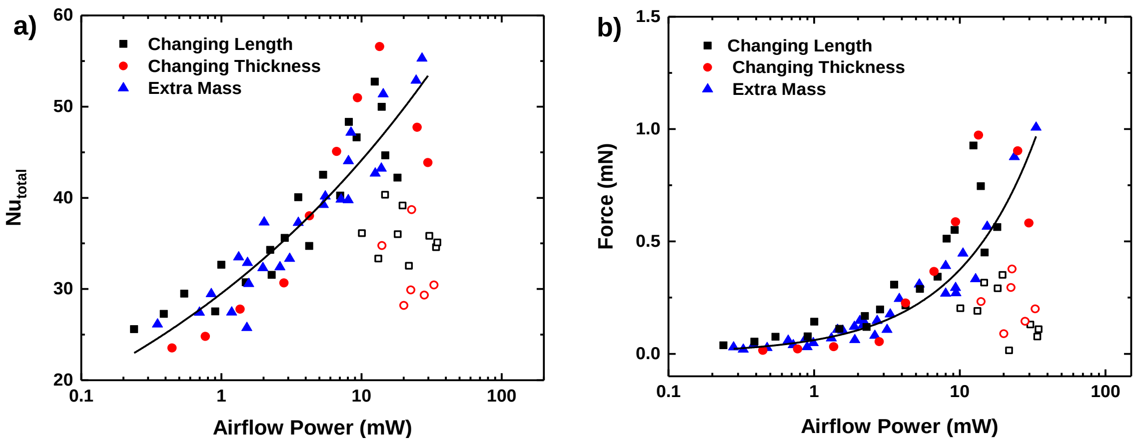

Figure 3.14 a) The experimentally measured Nusselt number as a function of the airflow power for all the piezoelectric fans and operating conditions used in the present study. Some anomalous behavior (hollow symbols) is observed where the heat transfer performance deviates from the general trend. b) The experimentally measured normal force on an opposing surface as a function of the airflow power. Similar anomalous behavior (hollow symbols) is also observed.

3.5 Summary

We investigated the vortex regimes present in the wake of a harmonically oscillating cantilever plate in a quiescent, incompressible, viscous fluid and analyzed their effect on the mean fluid jet downstream. More than 100 cantilever plates were examined over a wide range of Reynolds numbers ($10 < Re_c < 300$) using Particle Image Velocimetry and Immersed Boundary numerical simulations. Based on the qualitative features of the vortex shedding from the trailing edge, we identified three distinct vortex regimes in the wake, namely non-propagating, intermediate and propagating. We further demonstrated that these vortical patterns can be presented in a regime map in the parameter space of α and Re_c/α, with lines of constant Re_c as transition lines between adjacent regimes. At low Reynolds numbers ($Re_c < 37$) vortices do not propagate downstream and disappear with the generation of the next vortex (non-propagating regime). Increasing the Reynolds number ($37 < Re_c < 70$) enables the vortices to detach from the trailing edge and propagate downstream. These vortices, however, have low strength and dissipate quickly as the next vortex is formed (intermediate regime). At higher Reynolds numbers ($Re_c > 70$), vortices do not dissipate as completely after a half cycle and thus two counter-rotating vortices are observed propagating downstream. Comparing the temporal decay of the vortex strength in each regime, as quantified by the circulation contained in the vortex core, further revealed that the non-propagating and intermediate vortices are primarily influenced by the destructive effect of the subsequent vortex. This effect is less pronounced for the propagating cases as the vortices are more isolated.

Our qualitative and quantitative analysis of the flow on the normal mid-plane revealed that these vortex regimes significantly affect the mean fluid jet downstream of the thin plate. In the non-propagating regime, Re_{jet} is comparably lower and exhibits a weaker dependency on Re_c ($Re_{jet} \sim 0.1\, Re_c$), suggesting a low flow generation efficiency in this regime. In the propagating regime, Re_{jet} increases almost linearly with Re_c with a slope of ~ 0.8. We did not notice a clear trend for intermediate vortices.

The present study improves our understanding of the vorticity generation and transport in oscillating cantilever plates operating in quiescent fluids. Findings from this study are of significant importance in the applications such as piezoelectric cooling enhancement that highly rely on the airflow generation in front of the cantilever plates. Operation of such devices in non-propagating regime may result in a weak cooling performance and low power efficiency. The novel regime map introduced here provides a useful guide for selecting optimal operating conditions of similar devices. These results, however, were obtained in the midspan plane of the plates and do not provide a clear picture of the three-dimensionality of the flow. In the next chapter, we discuss this three-dimensionality and the associated unconventional shape of the jet downstream of pitching plates.

Chapter 4. 3D characteristics of the air jet downstream of piezoelectric fans

4.1 Background

In chapter 3, we revealed the different vortex regimes present in the wake of a pitching plate. As will be discussed in more detail in this chapter, these regimes are not unique along the span of the plate. In fact, the vortex generation and the associated flows downstream of a pitching plate exhibit extreme three-dimensionality.

The three-dimensional characteristics of flows generated by vibrating thin plates have been studied extensively in the past, due in part to their importance in understanding the natural behavior of aquatic and flying species. They also have enabled innovative employments of biomimetic structures in applications such as piezoelectric fans [63], [76] for thermal management of electronics [92], [93], micro air vehicles (MAVs) [70], swimming robots [94], fluid acceleration using the ionic polymer metal composites (IPMCs) [71]–[73], and energy harvesting [69], [95]. In applications that require net flow generation, such as fluid acceleration using piezoelectric fans or IPMCs, understanding the complex three-dimensional geometry of induced time-averaged jets and underlying transient wake vortex structures is critical for systematic designs of such devices.

Buchholz et al. [26], [27], [37]–[39] performed a comprehensive study of the 3D vortex structures in the wake of a pitching plate in the presence of a free stream. They observed that the vortices shed from the trailing and lateral edges of a pitching plate form horseshoe structures in the wake that interact with each other as they propagate downstream with the flow. Complementary to the previous works, Green et al. [40], [41] performed 3D PIV analysis on the pitching plates in a free stream and provided a valuable insight into the vortex structure topology and diffusion processes in the wake of an oscillating plate, however, not much was discussed in terms of flow fields and jet geometry, which are especially important for piezoelectric fan applications.

Although these past studies provided useful pictures of transient 3D vortex structures, detailed quantitative investigation of different factors affecting the shapes and other characteristics of downstream jets and their underlying mechanisms have been largely lacking. In the present chapter, we investigate the three-dimensional characteristics of the time-averaged induced jet in the wake of a pitching cantilever plate in a quiescent fluid and correlate these characteristics with the transient vortex structures in the wake and their temporal evolution. The rest of the chapter is organized as follows: In Section 4.2 we describe the parameters and experimental setup used in the present study. Section 4.3 provides a detailed description of the geometry, time–space discretization, solver properties and validity of the numerical simulations reported in this study. Section 4.4 contains the results and discussions regarding the fluid jet and wake vortex structures observed in the experiments and numerical studies. Summary and conclusions are presented in Section 4.5.

4.2 Experimental setup

The vibration characteristics of a plate are described by its frequency, *f*, and amplitude, *A*. We limit ourselves to small amplitude vibrations and represent oscillation of the trailing edge position y as

$$y = A\cos(\overbrace{2\pi f t}^{\phi}) \tag{4.1}$$

where $\varphi=2\pi ft$ is the phase of the oscillations. The characteristic trailing edge (or "tip") velocity in this study is defined as $u_{\mathrm{tip}} = fA$. The main length scale relevant to the 3D vortex shedding from the trailing edge is the width of the plate, w. The thickness of the plate, *t*, only has secondary effects on the vortex generation at the trailing edge. As we shall discuss later in section 4.4.2, the length of the plate, L, also has relatively small influence on the characteristics of downstream jet flows for the plates considered in the present study. The aspect ratio of the plate is defined as *AR* = *w*/*L*. The normalized amplitude, α, which represents the aspect ratio of the oscillation envelope (equivalent to Keulegan–Carpenter (KC) number in similar studies [96], is defined as

$$\alpha = \frac{A}{w} \tag{4.2}$$

and the oscillatory Reynolds number, *Re*, is defined as

$$Re = \frac{u_{\text{tip}}\, w}{\nu} = \frac{fAw}{\nu} \tag{4.3}$$

We use a commercial piezoelectric actuator (Steminc Inc., SMPF61W20F50) to oscillate cantilevers about their resonance frequencies. The actuator is 20 mm wide and 23 mm long (figure 4.1a). Flexible thin plates made of mylar with different dimensions are prepared in-house and attached to the actuator using cyanoacrylate glue. Table 4.1 lists the geometric parameters of the blades (width, *w*, and length, *l*, thickness, *t*) along with their vibrational characteristics (frequency, *f*, and amplitudes, *A*) used in the present study. Different resonance frequencies for the same cantilever (cases 7 and 8 in table 4.1) are obtained by changing the plate's mass distribution using a method reported in a previous study [76].

Small-amplitude sinusoidal voltage waves from a function generator (Model 33220A, Agilent) are amplified using a high-voltage amplifier (Model PZD700A, TREK) before being fed to the actuator (figure 4.1b). The desired vibration amplitudes were obtained by tuning the input voltage and measured optically with an uncertainty of ± 0.1 mm less than 10% of the minimum amplitude used in this study.

The 1 mm-thick illumination sheet for our PIV experiments (figure 4.1b) was generated using a 500 mW continuous wave laser (Hercules, LASERGLOW Technologies) with a wavelength of 532 nm. Successive frames were recorded using a high-speed camera (Phantom VEO-640L) capable of acquiring 16-bit, 4-megapixel images. The frame rate in each experiment was set to capture at least 70 frames per each full period of plate oscillation, equivalent to framerates > 6300 fps. A shutter speed of 80 μs was used to reduce the effects of motion blur.

PIV experiments were conducted in a large sealed transparent chamber made of acrylic plates (30 cm × 20 cm × 8 cm) to reduce interference from the side walls [77]. Seeding particles were generated by evaporating a solution of water and glycerin (30% glycerin in volume). The particles were then allowed to settle for about a minute before conducting any experiment to minimize initial disturbance from particle injection or previous experiments. Secondary fows due to the buoyant motion of the particles are estimated to be approximately 0.015 m/s in the streamwise (+x) direction. The chamber was mounted on a linear translation stage with a resolution of 0.01mm in order to move the plate relative the illumination sheet (figure 4.1b).

An open-source MATLAB software package, PIVlab [78], is used to analyze the captured video images. 64×64-pixel windows with 50% overlap are cross-correlated in two successive frames using the Advanced Discrete Fourier Transform technique embedded in the package to obtain the direction and magnitude of particles' displacements in the sub-areas. The calculated velocity fields are next post-processed by manually filtering the outlier data and replacing them with interpolated equivalents in areas where improper lighting condition leads to inaccurate displacement vectors. An algorithm based on penalized least squares method [80] is employed to smooth the flow fields.

The PIV setup and image processing procedure are validated using several benchmarks in [81]. In general, the bias error from window deformation and random errors from the cross-correlation algorithms are the main sources of uncertainty in the image processing steps. But for three-dimensional flows, the out-of-plane velocities are generally a larger source of error. These out-of-plane flows cause seeding particles to leave the illumination sheet in-between successive images, leading to random error. Assuming a very conservative estimate for the out-of-plane velocity of 1 m/s (of the same order as the maximum expected streamwise velocities) and a minimum framerate of 6300 fps, particles are projected to travel at most 0.16 mm or 16% of the illumination sheet thickness between successive frames. This is considered an acceptable error, as other works in the literature have reported out-of-plane displacements of 50% the light sheet thickness [41]. An overall uncertainty of 0.14 pixel is estimated for the displacement vectors obtained in our PIV experiments. Considering other uncertainties, such as pixel to distance conversion and camera framerate accuracy, we estimate a total uncertainty in velocity measurements of 0.016 m/s.

To construct 3D vortex structures from the results of our PIV experiments, we first extract 2D PIV data from 21 planes uniformly spaced 1 mm apart along the span of the plate (normal to the z axis, figure 4.1c). The identified vortex cores in each plane are then interpolated to form 3D vortex structures. A similar technique was reported in [41] and [42]. Further discussion of this technique is provided in Sec.4.

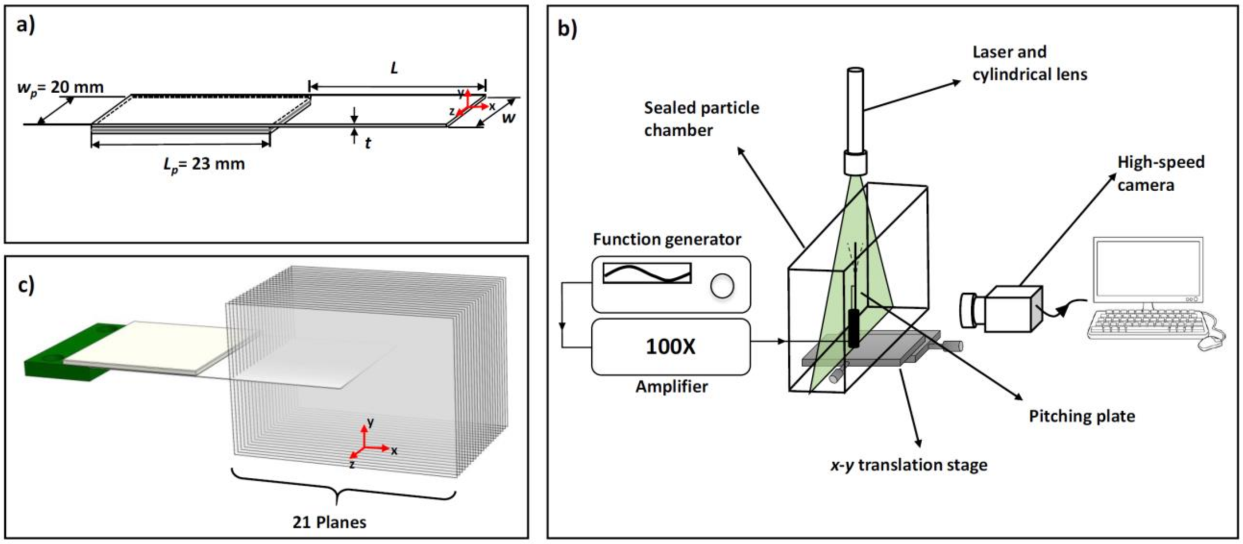

Figure 4.1 (a) Schematic of the piezoelectric actuator and the oscillating plate. (b) Schematic of the PIV experiment setup. (c) Visualization planes for the 3D PIV data extraction used in the present study.

Table 4.1 Geometric and vibrational characteristics of the plates used in the present study and the corresponding dimensionless parameters. The two last columns indicate whether PIV or numerical simulation results are available for each case. The vibration amplitude *A* is varied among Cases 1 and 2 for otherwise identical plates; the plate width *w* for Cases 1, 3 and 4; the plate length *l* for Cases 1, 5 and 6; and the vibration frequency *f* for Cases 1, 7, and 8.

Case No.	***l* (mm)**	***w* (mm)**	***t* (mm)**	***f* (Hz)**	***A* (mm)**	**α**	***Re***	***AR***	**PIV**	**Sim.**
1	20	20	0.2	70	2.5	0.123	230	1	•	•
2	20	20	0.2	70	1.4	0.07	131	1	•	•
3	20	12.7	0.2	70	2.5	0.194	146	0.64	•	•
4	20	30	0.2	70	2.5	0.082	344	1.5	•	•
5	15	20	0.2	70	2.5	0.123	230	1.33	•	•
6	30	20	0.2	70	2.5	0.123	230	0.67	•	•
7	20	20	0.2	40	2.5	0.123	131	1	•	•
8	20	20	0.2	100	2.5	0.123	328	1	•	•
9	15	20	0.2	70	1.8	0.092	172	1.33	×	•
10	30	20	0.2	70	3.7	0.185	345	0.67	×	•

4.3 Numerical simulations

Three-dimensional numerical simulations are performed using a commercial computational fluid dynamics package (Ansys CFX). We use the Immersed Boundary Method to circumvent the computational overheads associated with re-meshing and distorted nodes in moving mesh methods. The dimensions of the simulation domain are $3w \times 2w \times w$ (figure 4.2a), large enough to capture the desired properties of the wake while avoiding any complicating effect at the boundaries. This was verified using PIV visualization and a domain size independence study. The open boundary condition is specified on the outer walls of the computation domain to allow free fluid motion in directions normal to the domain boundaries. The relative pressure on these boundaries is specified as zero.

We use tetrahedral meshes of spatially varying sizes along the trailing edge: $0.005w$ in 7 spheres of radius $0.125w$ centered along the trailing edge, $0.01w$ in 3 intermediate spheres of radius $0.25w$, and $0.025w$ in the rest of the domain (figure 4.2b). To confirm the mesh independence of our numerical simulation results, a representative case is run with different grid sizes. The predicted time-averaged velocity (from cycle 11 to 20) on the midspan line ($x/A = 0.8$) changed by less than 5% for mesh sizes half the chosen set of values.

The cantilever plate is approximated as an immersed solid prescribed to rotate rigidly about a pivot point at its base. This approximation is justified by the predominance of the lowest-order vibration mode. Figure 4.2c compares an actual plate deflection obtained from one of our experiments with that from the rigid body approximation at an exaggerated amplitude. The slope at the trailing edge estimated from the rigid body assumption differs by less than 1% from the slope obtained experimentally. Based on Lighhill's theory of elongated bodies[97], it is the motion of the trailing edge and its vicinity that primarily determines the wake properties and thrust/drag signature and not intermediate motions along the plate. This approximation was also shown to successfully predict the characteristics of a two-dimensional jet from a cantilevered plate [98].

The first-order upwind scheme is used for advection terms and a first-order backward Euler scheme is used for time marching. The time step in the computations is automatically adjusted such that the Courant number remains lower than one in all computational cells. Using second-order upwind scheme did not result in appreciable change in the predicted jet boundary. This is expected because for low Reynolds flows of this study, numerical damping is negligible when compared with viscous damping in the problem.

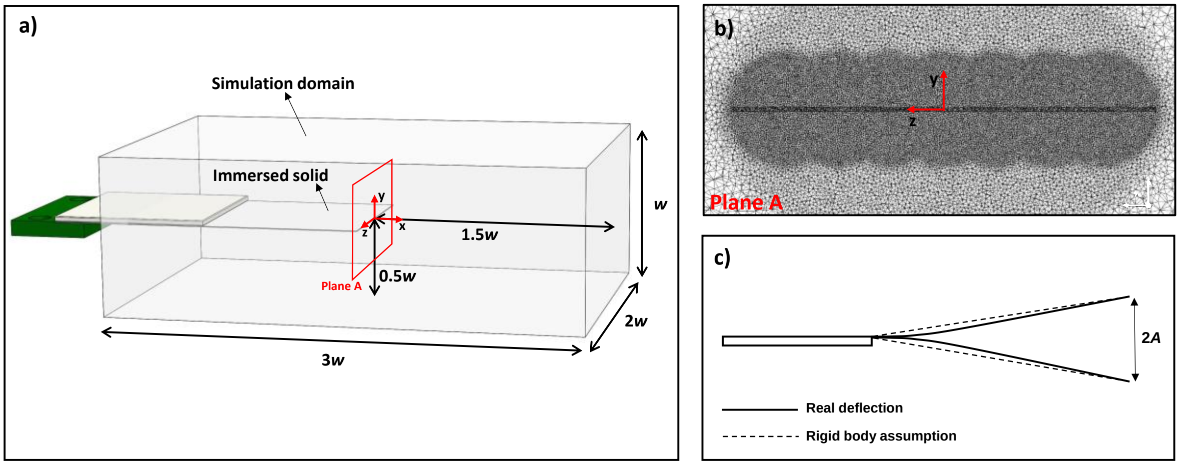

Figure 4.2 (a) Numerical simulation domain. (b) Mesh used in the present numerical simulation. (c) Comparison between the actual plate deflection and the rigid body approximation (images are not to scale).

4.4 Results and discussions

4.4.1 Time-averaged 3D jet

Figure 4.3a shows a typical time-averaged velocity profile of a pitching cantilever plate over 10 cycles of oscillations (cycles 11 to 20) obtained from numerical simulations (upper half) and PIV experiments (lower half) for Case 1 (Table 4.1). The first 10 cycles are not considered to allow the initial transients to settle and reach a steady periodic state. We define the jet boundary by identifying and interpolating the loci of flow entrainments (white circles along the streamlines on the *x*-*z* plane, lower left figure 4.3a) where the direction of the time-averaged velocity changes from +*x* to –*x*. The negative value of the average streamwise velocity outside the jet boundary is rather unique to jets produced by pitching plates and is not usually observed in 2D and 3D jets. Our definition of the jet boundary contrasts somewhat with typical studies of jets, in which the jet boundary is defined by a threshold value of streamwise velocity, e.g. 1% of the momentum-averaged velocity.

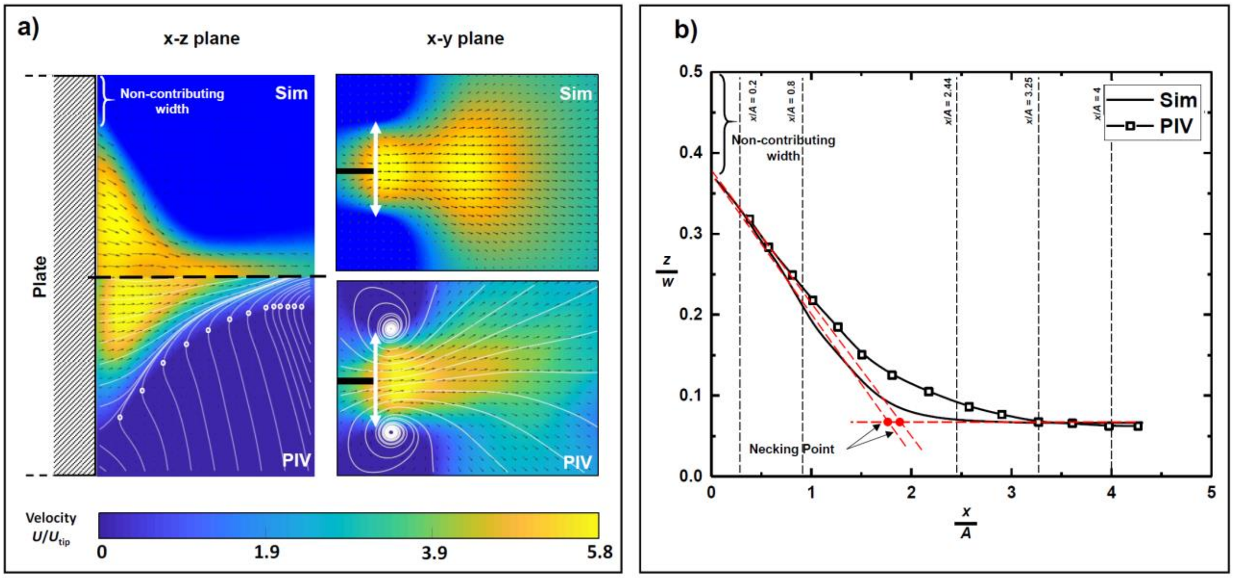

Figure 4.3 (a) Time-averaged velocity profile of a pitching cantilever plate in the *x-z* and *x-y* planes (Case 1). The thick white arrows indicate the tip-to-tip displacement of the trailing edge (= 2*A*). (b) Time-averaged jet boundary projected on the *x-z* plane.

Figure 4.3 suggests that the induced mean jet forms two distinct regions downstream. Close to the trailing edge, the mean jet boundary in the *x-z* plane shrinks linearly in the spanwise direction towards the midspan line as the flow proceeds in the +*x* direction, while being almost independent of *x* in the *x-y* plane. The average velocity in this region is nearly uniform, with small fluctuations around the average value, u_{ave} (figure 4.4a). The magnitude of this average velocity is approximately a linear function of the tip velocity with a slope of ~5.6, as shown in the inset of figure 4.4a. Further downstream, at approximately *x*/*A* ~ 1.7, the jet boundary stops shrinking in the *x-z* plane and forms two parallel lines. This coincides with an abrupt expansion of the jet boundary on the *x-y* plane, accompanied by a significant change in the direction of the velocity vectors. We refer hereafter to the borderline between the two regions as the “necking point”, defined approximately by the intersection of two tangent lines to the jet profile as shown in figure 4.3b. The streamwise location of the necking point is referred to as the necking length and serves as a quantitative measure of the streamwise extent of the jet.

The streamlines form two spiral curves on the top and bottom of the oscillation envelope in the *x*-*y* representation of figure 4.3a. The spiraling indicates a spanwise transport of flow toward the midspan. These two spiral streamlines confine the flow to a high velocity region between them and form the boundary of the jet in the *x*-*y* plane upstream of the necking point. As we shall show later, these spirals and the associated change in direction of the flow are related to the transient tilting of vortex structures shed from the trailing edge. Downstream of the necking point, the streamwise velocity component decreases significantly (figure 4.4a) due to the mixing facilitated by interactions of the vortices.

We also note from figure 4.3 (on the *x*-*z* plane) not all portions of the width of the plate contribute to the flow generation at the trailing edge. The two most outboard portions, referred to as the non-contributing width hereafter, are located at the sharp corners of the thin plate and experience a weakly negative streamwise velocity. In this study, we quantify the non-contributing width only based on the numerical results, because the velocity field close to the trailing edge in the PIV results is affected by the motion of the plate itself and by the reflection of the light from the surface, and hence, does not reliably represent the particles’ velocity. This fact is evident from the lower velocity of the PIV data in a narrow band (~32 pixels or overlapped portion of the cross-correlated windows) adjacent to the trailing edge in figure 4.3a.

Figure 4.4b shows the normalized streamwise average velocity profiles on the *x*-*z* plane (*y* = 0) at 5 different *x* locations. The jet boundary in this figure is evident at the locations were the velocity profiles change sign. We observe that the velocity profiles before the necking point (*x*/*A* = 0.2 and 0.8) exhibit two peaks on either side of the midspan line. In contrast, the velocity profiles after the necking point (*x*/*A* = 2.44, 3.25, 4) have only single peaks along the midspan line. These profiles after the necking point exhibit approximately the same shape outboard of *z*/*w* ~ ±0.05, in agreement with two nearly parallel lines defining the jet boundary after the necking point.

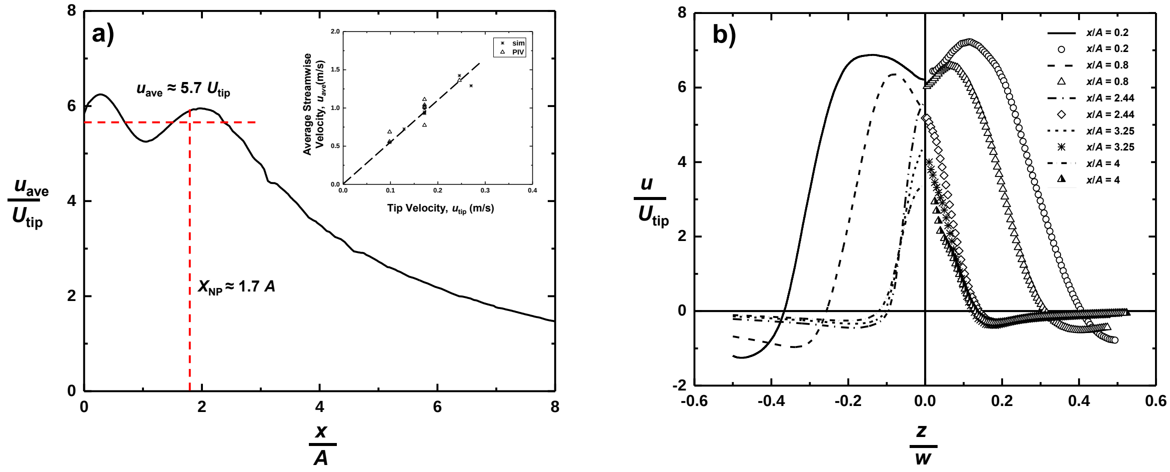

Figure 4.4 (a) Time-averaged streamwise velocity along the midspan line, *y* = 0 and *z* = 0 (Case 1) (b) The spanwise profile for the time-averaged streamwise velocity at 5 locations along the *x* direction shown in figure 4.3b.

The physics underlying the counter-intuitive geometry of the jet can be understood by considering the transient three-dimensional wake vortex structures shed from the trailing edge and side edges of the plate. Figure 4.5 shows such structures in a full cycle of oscillation as obtained from our PIV experiments and numerical simulations. The vortex cores are identified using the second invariant of the velocity gradient tensor ∇U, known as the Q-criterion [99]. For consistency, the threshold for the Q-criterion was set at a fixed value equal to approximately 10% of the maximum Q values at phase $\varphi = 0$. The color of the vortex structures in the numerical simulations represents the magnitude of the vorticity in the z-direction, ω_z, while in the PIV results only it manifests the vortex rotation sign (clockwise or counter-clockwise). We note that because our PIV results do not resolve the spanwise velocity component, vortices along the side edges are not captured in these representations.

Figure 4.5 shows that the vortex formation starts slightly earlier than $\varphi = 0$ with counter-clockwise vortices forming in the spanwise direction along the width of the cantilever. This was also confirmed in the 2D studies of Kim *et al.* [31] and Dehdari Ebrahimi *et al.*[98]. This spanwise structure is accompanied by two streamwise vortices at the cantilever side edges, that together form a horseshoe structure. The oscillation velocity of the pitching plate linearly increases with the chordwise distance from the leading edge. Therefore, the vortex strength of the legs of the horseshoe increases in the chordwise direction. In the same instant, the previously generated clockwise vortex still exists as a coherent structure. This structure is attached to the cantilever plate at the sharp corners and increasingly separated from the plate towards the midspan. As the cantilever plate continues its downstroke half-cycle towards the neutral position ($\varphi = \pi/2$), the counter-clockwise vortex structure grows and separates from the trailing edge in the midspan while still being attached to the corners. In addition, the clockwise vortex structure from the previous cycle breaks down from the midspan and the corners, forming two coherent sub-structures.

We emphasize that the vorticity does not actually disappear at the midspan and corners, but spreads and splits, forming a hairpin vortex that connects the two sub-structures. This hairpin vortex structure, however, is not shown as its strength is below the threshold Q value. The two vortex sub-structures are wrapped around the new spanwise vortex as they are convected downstream. This wrapping effect adds a y-direction component to the vorticity of the sub-structures, inducing a significant flow toward the midspan and a corresponding outward flow in the y-direction. This behavior leads to the abrupt expansion of the jet boundary on the x-y plane (figure 4.3a) discussed earlier. At $\varphi = \pi$, the clockwise vortex sub-structures travel further downstream while losing their core strength owing to diffusion. Due to the low strength of these vortex sub-structures, our PIV visualizations were not able to capture them beyond this instant. At the same instant, the counter-clockwise spanwise structure (shown in red) has gone through the same process and is ready to break. At $\varphi = 3\pi/2$, the counter-clockwise vortex structure breaks and the consequent sub-structures wrap around the new vortex in opposite directions, similar to $\varphi = \pi/2$.

The vortex breakdown and tilting in the wake of pitching plates was also reported by Green *et al.* [41]. However, due to the higher strength of their vortices, vortex breakdown was delayed until after two and a half cycles (as opposed to less than a cycle in the current study). Furthermore, the presence of a free stream in their experiments augmented the vortex transport such that the vortex breakdown and the subsequent jet boundary shrinkage only occurred at the end of their domain where the flow characteristics were not of significant importance.

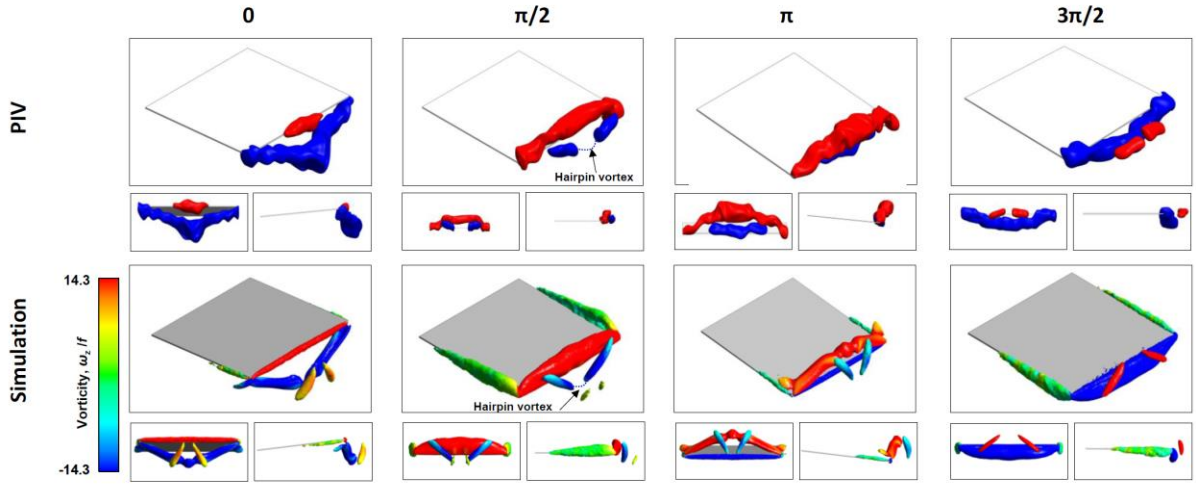

Figure 4.5 Three-dimensional vortex structures obtained from the experimental and numerical simulation results during one full cycle of oscillation (Case 1).

Figure 4.6 illustrates the temporal evolution of the *y* component of vorticity in *x*-*z* plane in a half pitching cycle. Due to symmetry, only half of the period of oscillations, 1/*f*, is shown in this figure. The projections of the vortex sub-structures described above are shown as high vorticity regions in this plane. These high vorticity regions are concentrated along the jet boundary and are the primary reasons for the spanwise shrinking of the jet shape. We note that, unlike our numerical simulations, the instantaneous PIV results are highly asymmetric about the midspan line. We believe that the reason for this asymmetry is the strong sensitivity of the flow to the introduced disturbances from the environment. Non-uniform deflections of the trailing edge due to the plate imperfections (such as uneven mass distribution of the pitching plate due to manufacturing or assembly flaws) and secondary flows in the visualization chamber are examples of factors contributing to these disturbances. However, we should point out that these disturbances do not significantly influence the mean behavior of the flow, as shown previously in figure 4.3.

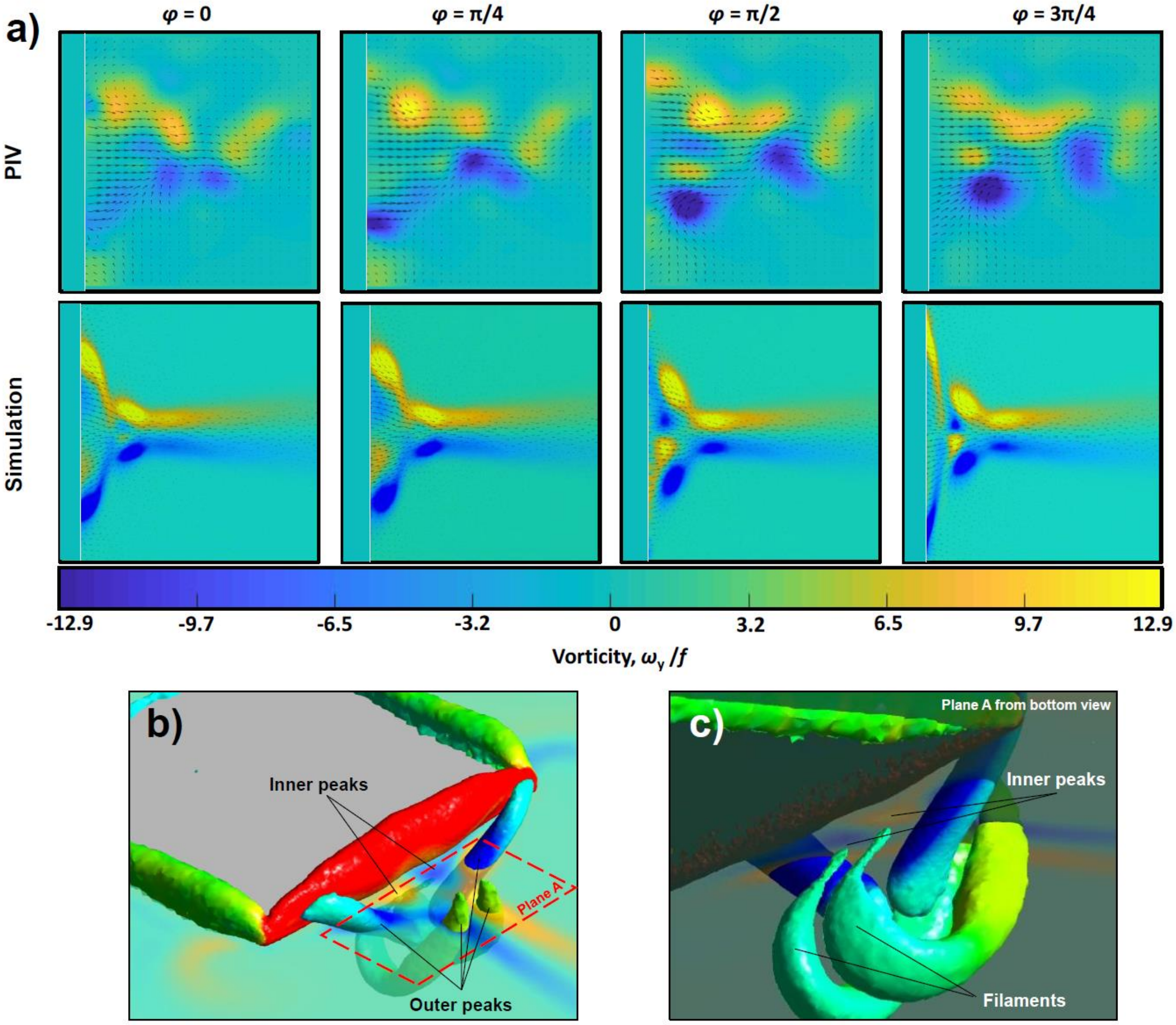

Figure 4.6 (a) The temporal evolution of the y component vorticity on the *x*-*z* plane over a half pitching cycle for case 1. (b) and (c) The source of the inner vorticity peaks clarified at $\varphi = \pi/2$. The inner vorticity peaks have lower strength compared with the outer peaks. For example, at $\varphi = \pi/2$, the vortex core circulation in the two outer peaks close two the trailing edge is 13.5 Af^2 and 11.6 Af^2 for PIV and simulation results, respectively. For the inner vorticity peaks, these values are 1.5 Af^2 and 1.4 Af^2 for the PIV and simulation results, respectively.

In figure 4.6, we also observe the presence of inner peaks in the vorticity contours. These inner peaks are projections of the vortex filaments stemming from the vortex shed one cycle before. These filaments are not shown in figure 4.5 due to their low strength. Figures 4.6b and 4.6c clarify the origin of the inner vorticity peaks. Although these vorticity peaks do not affect the jet boundary, we can attribute the dual peak behavior close to the trailing edge (corresponding to the profiles before the necking point in figure 4.4b) to the interactions between these vortices and the outer vortices. Vortices of opposite signs (each pair of inner and outer vortices on the same side of the midspan line) create a high-velocity region that forms the dual peak pro files of figure 4.4b. The inner vorticity peaks, and hence the dual peak profiles, dissipate after the necking point.

To further elucidate the three-dimensionality of vortex shedding from the trailing edge and clarify the presence of a non-contributing width, we compare the instantaneous spanwise vorticity contours in 2D PIV results along the span of the plate. Figure 4.7 demonstrates these contours and the velocity vectors at $\varphi = 3\pi/2$ on three different planes with indicated spanwise locations. Near the midspan ($z/w = 0$), the vortices have higher strength and are more separated from the trailing edge. These vortices exhibit features resembling the propagating vortices observed in previous work [98]. Towards the corners of the thin plate, the vortex is attached to the trailing edge, characteristic of the non-propagating regime reported in [98]. An appreciable decrease in the strength of the spanwise vortex component and the velocity magnitude is also evident. Similarly, Green *et al.* [41] observed a change from 2S thrust producing vortex alignment near the midspan to 2S drag producing alignment close to the corners for their trapezoidal pitching plates in moving water. We can attribute the existence of non-contributing portions close to the spanwise extremes of the pitching plate to the presence of such non-propagating vortices at the plate corners.

We note that the asymmetry in the vortex position relative to the plate at z/w = 0.25 and z/w = 0.45 is mirrored in the next half-cycle, which leads to tilting in the induced flow in the ± y-direction over each half-cycle. This effect, however, cancels out when averaged over a full cycle. Therefore, we believe that this up-down asymmetric behavior is different from the symmetry breaking phenomenon (also known as the bifurcating flows) observed in previous studies (see Godoy-Diana *et al.* [100] , Shinde & Arakeri [101], and Cleaver et al. [102]). In these symmetry breaking flows, the vortex pair in reverse von Karman street is skewed towards one side of the plate's neutral axis and propagates in the same direction. Therefore, the time-averaged velocity forms a finite angle with respect to the mid-span line. This feature is absent in our PIV results.

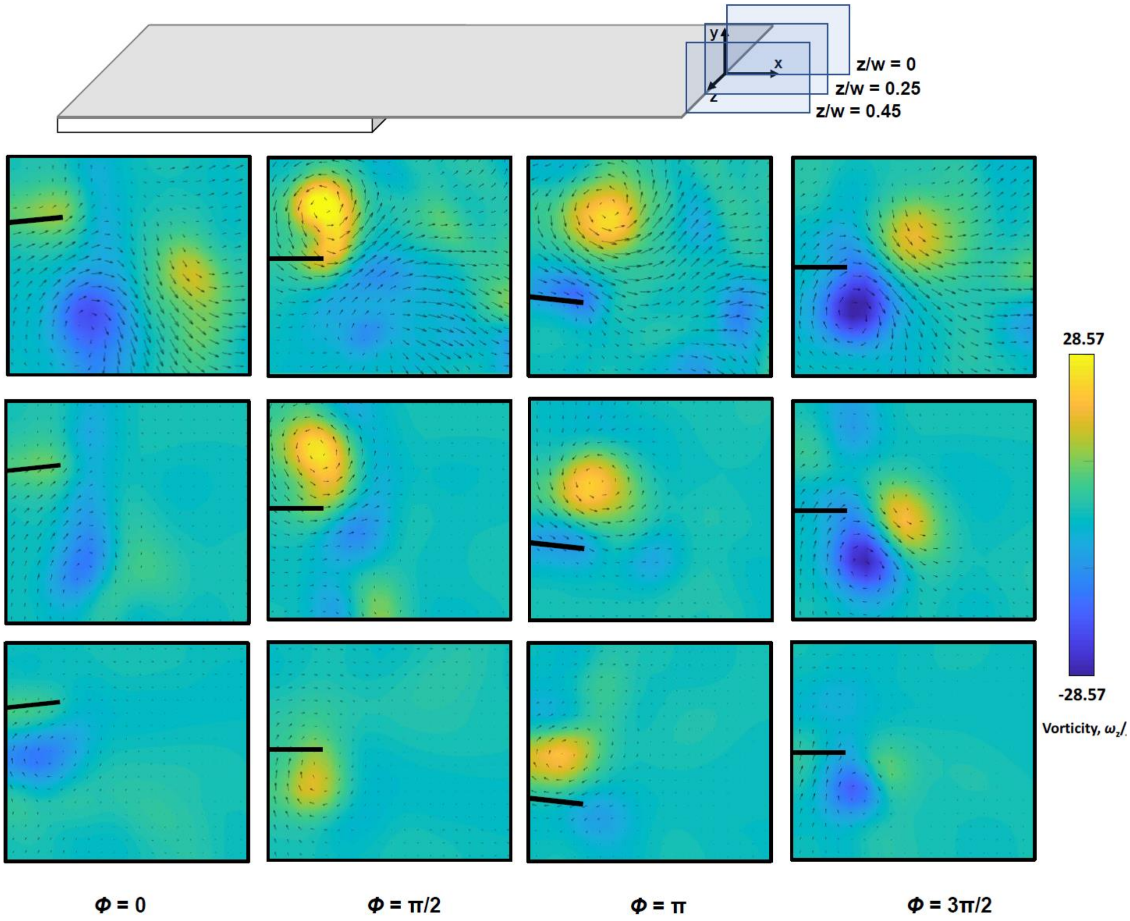

Figure 4.7 Spanwise vorticity contours at three different spanwise locations

4.4.2 Governing factors of the shape of the jet

In the following sub-sections, we investigate the effect of several vibrational and geometric factors on the three-dimensional shape of the jet and the vortex behavior at the trailing edge.

Effects of normalized amplitude, α – The two cases illustrated in figure 4.8, corresponding to cases 1 and 2 in table 4.1, differ only in their vibration amplitudes. The extent of the jet boundary in the streamwise direction, as quantified by the normalized necking length, x_{NP}/A, in figure 4.8, is dependent on *α*. The normalized necking length decreases from 2.3 for the smaller to 1.7 for the larger, representing 26% decrease for 75% increase in the normalized amplitude. The graphs also suggest a dependence of the normalized non-contributing width, *w**/*w*, on *α*. A more detailed discussion of the amplitude dependence of the necking length and the non-contributing width is presented in section 4.4.2.

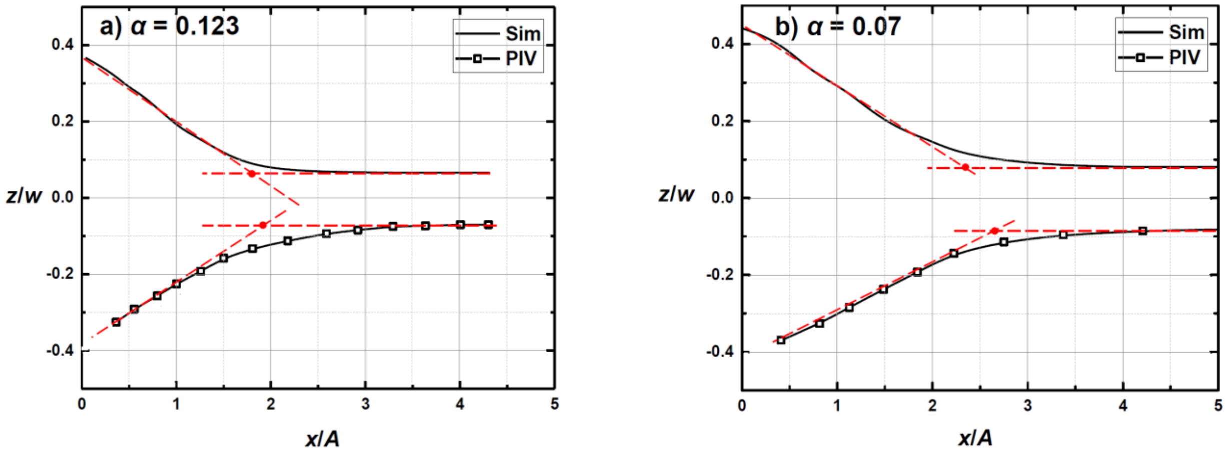

Figure 4.8 Effect of α on the jet boundary projected on the x -z plane for plates with different amplitudes corresponding to (a) Case 1 (*A* =2.5 mm) and (b) Case 2 (*A* = 1.4 mm).

Figure 4.9 shows the vortex core structures emanating from the trailing and side edges of the plate for the two cases presented in figure 4.8. In these cases, the maximum and minimum height of the vortex structures at the midspan approximately coincide with y= ±*A*. Furthermore, the vortex structures in both cases arch over the width of the plate and connect to the sharp corners regardless of the amplitude. As a result, the curvature (bending) of the vortex structure is more pronounced at the larger values of *α*.

In addition, the strength of the vortex structures increases with *α*, as indicated by the color of the structures, enabling them to travel further downstream before diffusing due to viscosity. The combination of these two effects, i.e. the increased curvature of the structures and the higher vortex strength causes the flow to stretch more in both the *x* and *y* directions at higher normalized amplitudes.

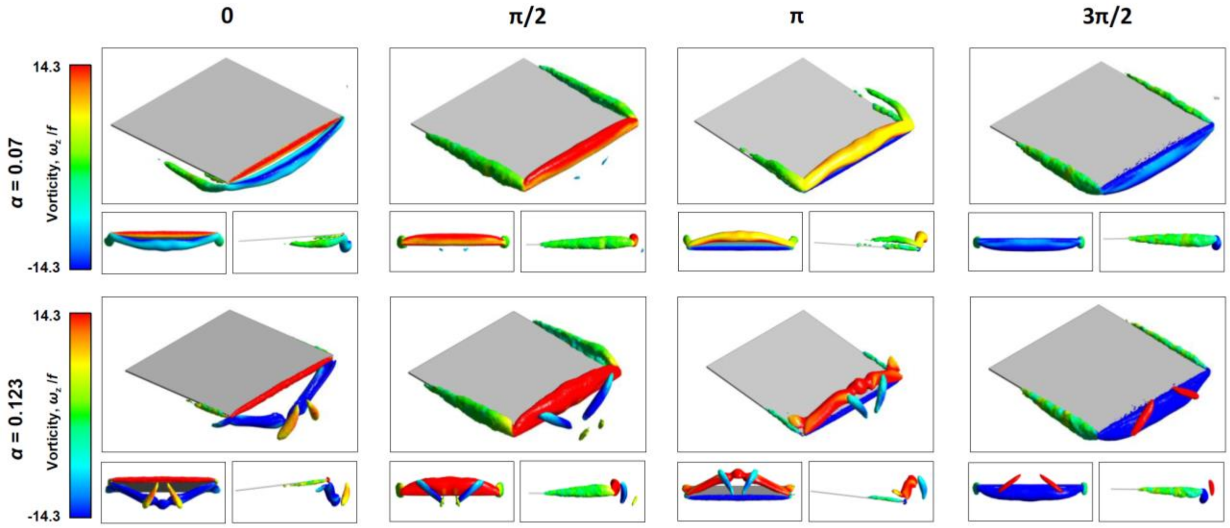

Figure 4.9 Three-dimensional vortex structures obtained from numerical simulation over one full cycle of oscillation at different values of for plates vibrating at different amplitudes (*A* =1.4 and 2.5 mm, corresponding to Cases 2 and 1) in the respective rows.

Figure 4.10 shows the jet boundary for the plates that only differ in their widths. The spanwise extent of the mean jet increases with the width of the plate, with an exception of areas close to the trailing edge, where the effect of the non-contributing width of the plate is more pronounced. Once again, we observe that w^*/w exhibits a strong dependence on α, increasing about 80% when α is increased 130% from 0.082 to 0.194. Figure 4.10 also confirms our previous observation that decreasing α elongates the streamwise extent of the mean jet, as indicated by the location of the necking point. x_{NP} /A for the smallest α is ~76% larger than that for the largest α.

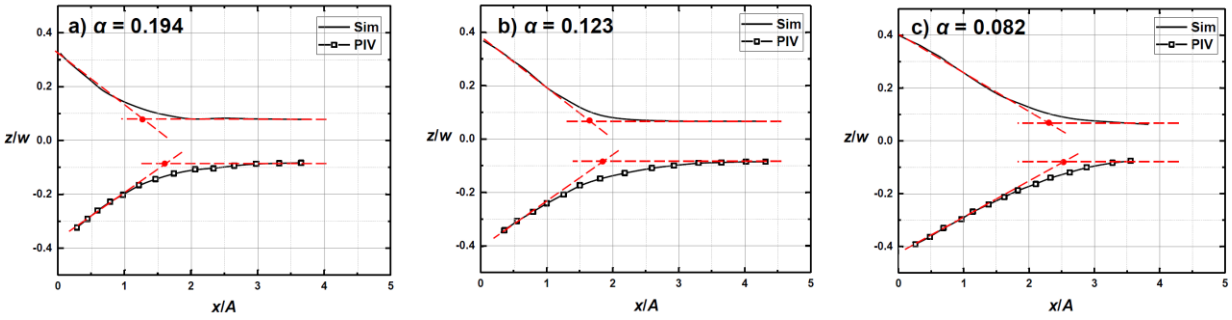

Figure 4.10 Effect of α on the jet boundary projected on the *x* -*z* plane for plates with different widths corresponding to (a) Case 3 (*w* = 12.7 mm), (b) Case 1 (*w* = 20 mm), and (c) Case 4 (*w* = 30 mm).

Figure 4.11 shows the downstream wake vortex structures for the plates of different widths. From the frontal views of the shed structures at $\varphi = 0$ and $\varphi = \pi$, we note that the maximum and minimum height of the vortex structures in the midspan are almost independent of the plate width, i.e. the vortex structures have the same normal distance from the trailing edge at the midspan. For the narrowest plate (*w* = 12.7 mm), the vortex structure has a relatively higher curvature, which in turn makes the two wrapped sub-structures in $\varphi = \pi/2$ and $\varphi = 3\pi/2$ closer to each other and oriented at a relatively small angle. For *w* = 20 mm, the vortex core structure is less curved, and thus, consecutive vortex sub-structures are further apart and oriented at a wider angle. For the widest plate (*w* = 30 mm), the vortex structure is at the midplane, such that at low values of α the flow near the trailing edge can be assumed as two-dimensional.

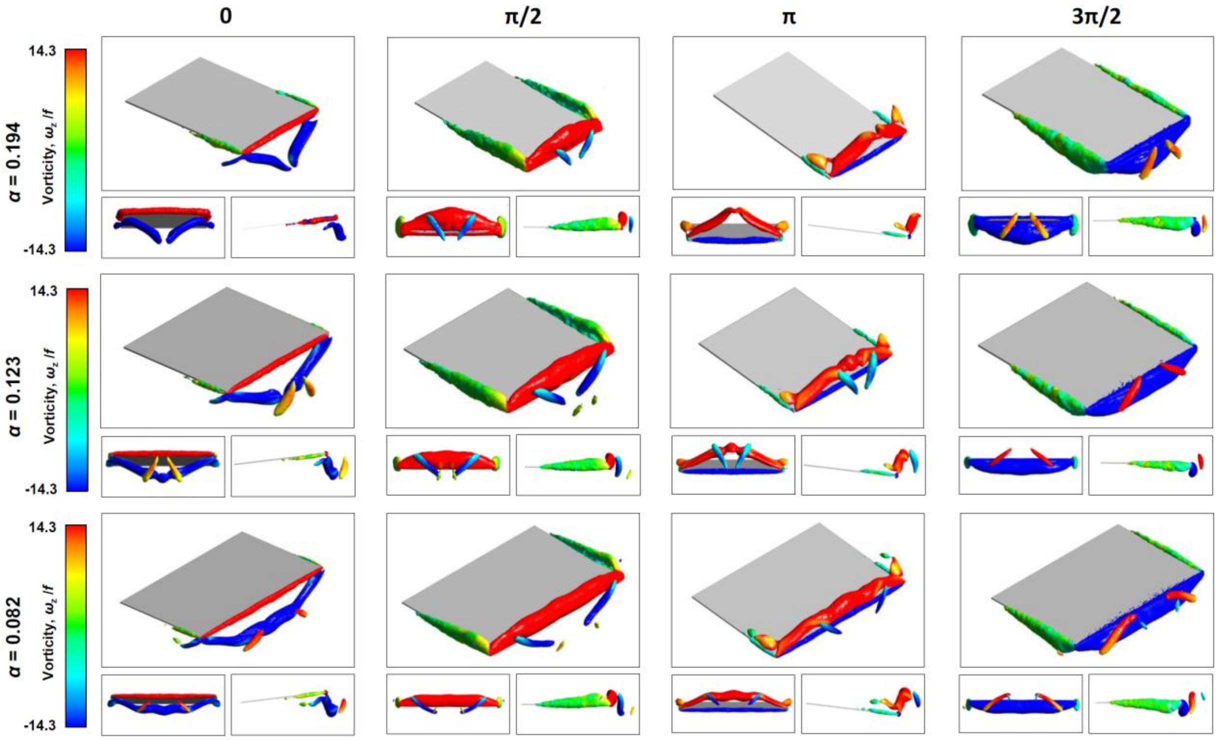

Figure 4.11 Three-dimensional vortex structures obtained from numerical simulation over one full cycle of oscillation with different values of for the plates with different widths w = 12.7mm (Case 3), 20 mm (Case 1), and 30 mm (Case 4).

Effects of plate aspect ratio, *AR* – Our experimental and numerical simulation results show that, for the plates considered in the present study, the plate aspect ratio has relatively small effects on the geometry of the jet. Figure 4.12 shows the jet boundaries downstream of the pitching plates of different aspect ratios, showing no significant change. Only 3% increase in the normalized necking length, $x_{\mathrm{NP}}/\mathrm{A}$, and 18% increase in the normalized non-contributing width, w^*/w, are observed when the plate aspect ratio is decreased by 100%.

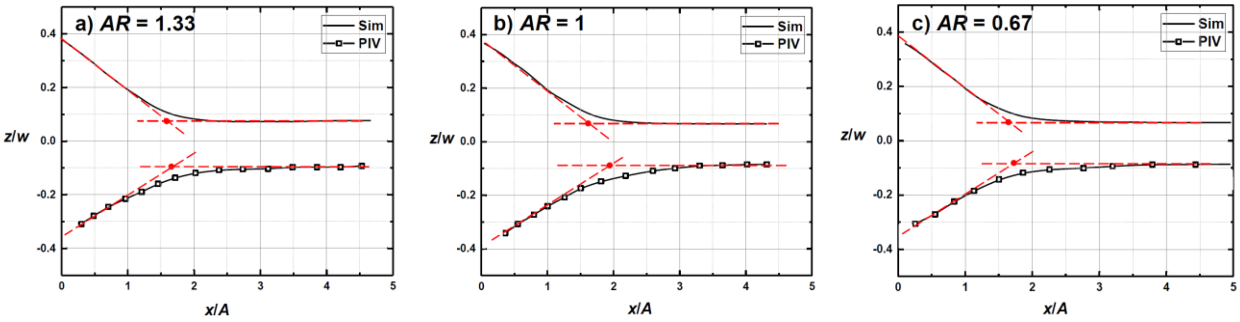

Figure 4.12 Effect of plate aspect ratio on the normalized jet boundary projected on the *x*-*z* plane for the plates with different lengths corresponding to (a) case 5 (l = 15 mm), (b) Case 1 (l = 20 mm), and (c) Case 6 (l = 30 mm).

Figure 4.13 shows the wake vortex structures for different plate lengths examined. The curvature of the vortex structure is nearly identical in all three cases, indicating that the vibration amplitude and the plate width are the primary length scales affecting the wake. But the coherence of the vortex structures is weaker at smaller plate aspect ratios and the structures generated by these plates are more likely to break earlier.

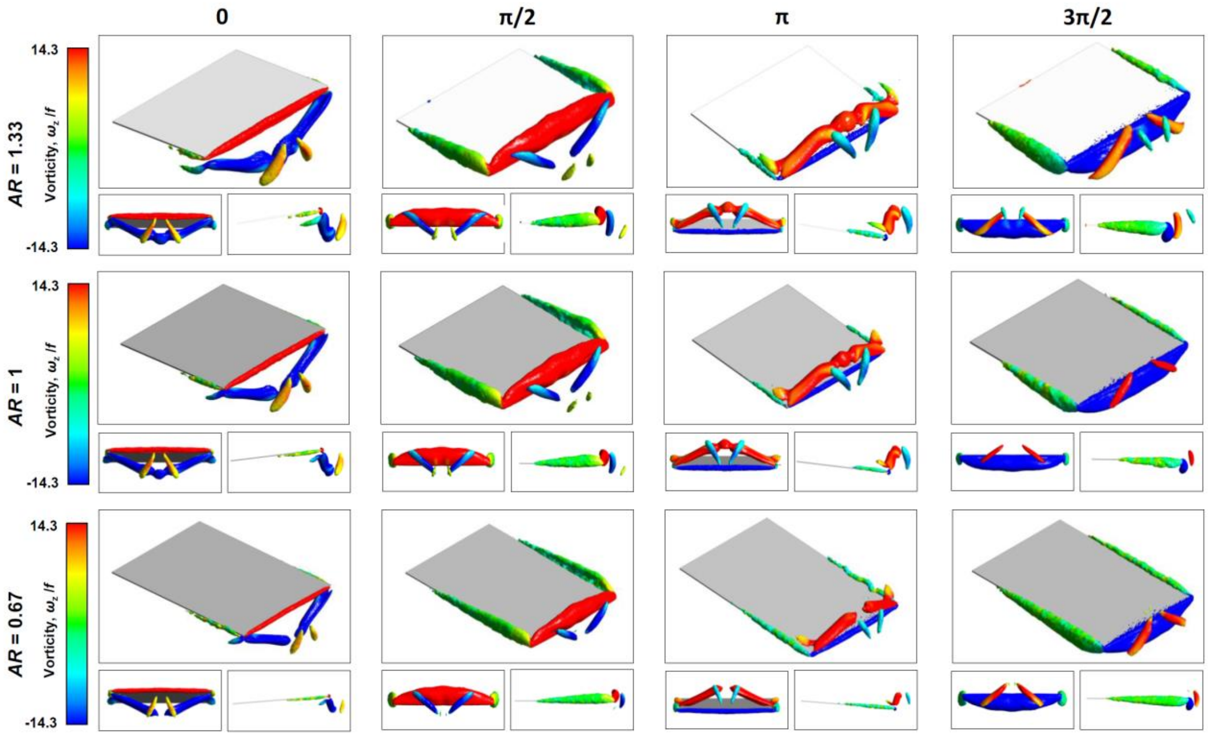

Figure 4.13 Three-dimensional vortex structures obtained from numerical simulations during a full cycle of oscillation for plates with different aspect ratios (corresponding to different lengths in the respective rows: *l* = 15 mm (Case 5), 20 mm (Case 1), and 30 mm (Case 6).)

Effects of Reynolds number, *Re* – Figure 4.14 shows the jet boundary for three different vibration frequencies and hence, different Reynolds numbers. Similar to the plate aspect ratio, changing Re does not affect the boundary of the jet. However, the magnitude of the jet velocity is almost linearly proportional to Re, as previously shown in figure 4.4. The slight up-down asymmetry observed in the PIV results at the lower *Re* is believed to be an experimental artifact caused by environment disturbances.

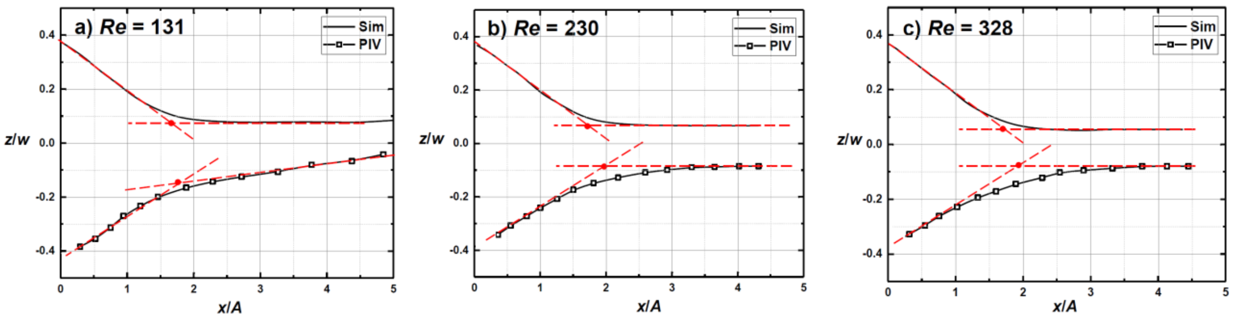

Figure 4.14 Effect of Re on the normalized jet boundary projected on the *x*-*z* plane for plates with different frequencies: *f* = 40 (Case 7), 70 (Case 1), and 100 Hz (Case 8).

Necking length and non-contributing width – The normalized necking length for all the cases examined in this study are presented in figure 4.15a. The necking length varies approximately with α as

$$\frac{x_{NP}}{A} = n\,\alpha^{m} \tag{4.4}$$

The power law curve fits to our experimental and numerical simulation results are shown with the solid and dashed lines, respectively. The exponent, m, is equal to -0.55, suggesting that the necking length is influenced to similar degrees by the plate width and vibration amplitude ($x_{\mathrm{NP}} \sim A^{0.45}w^{0.55}$). We note that the quality of the curve fits in figure 4.15a is not sensitive to the exponent within a margin of $\Delta m = \pm 0.05$, and thus assuming an equal influence from amplitude and width is reasonable. The coefficient n is slightly (~17%) larger for the experimental data. This difference may be attributed to a combination of factors, including the rigid body approximation, the use of the first-order upwind scheme in the numerical simulation, and constant streamwise motion of seed particles due to buoyancy or other environment disturbances. Figure 4.15b shows that the normalized non-contributing width follows a similar power law trend ($w^* = 0.74\,A^{0.85}w^{0.15}$). The correlation suggests that the non-contributing width is predominantly governed by the amplitude of the pitching motion and is only slightly affected by the plate width. This is consistent with the fact that the size of streamwise vortices produced at the lateral edges of the plate also scales with *A* [103]. We believe that at the sharp corners, these lateral vortices tend to suppress the trailing edge vortices, which reduces the strength of vortices near the sharp corners and hence generates a non-contributing width.

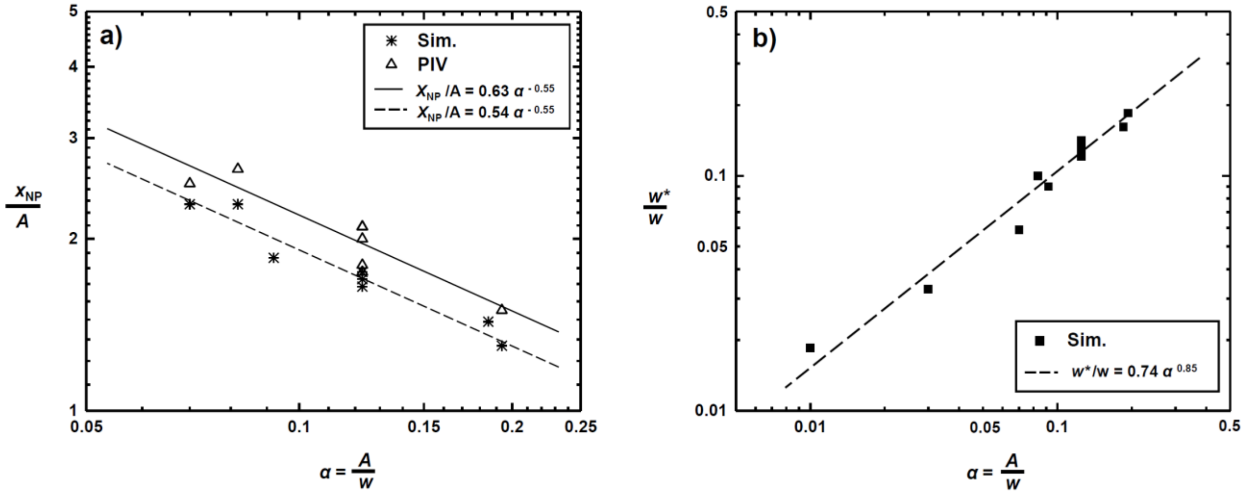

Figure 4.15 (a) Normalized necking length as a function of the normalized vibration amplitude. The solid and dashed lines correspond to the power law curve fits to the experimental and numerical simulation results, respectively. (b) Normalized non-contributing width obtained from the numerical simulation results as a function of the normalized amplitude. The dashed line represents the power law curve fit.

4.4.3 Scaling laws for the shape of the jet

Figure 4.16 shows the jet boundaries, as projected on the *y*-*z* plane, at different streamwise locations from the trailing edge normalized by $(Aw)^{1/2}$. The mean streamwise flow starts as a uniform jet exiting the aperture defined by an oscillation envelope. Before reaching the necking point (figure 4.16 a & b), the jet shrinks linearly in the spanwise (*z*) direction but remains confined within approximately ±*A* in the normal (*y*) direction. As the flow passes the necking point (figure 4.16 c – e), the jet boundary expands in the normal (*y*) direction. The width of the jet boundary (along the *z* direction), however, remains nearly constant (0.2*w*) after the necking point. We note that the jet boundaries from all the cases considered in the present study collapse onto nearly universal curves if we normalize the position along the streamwise (x) direction with $(Aw)^{1/2}$, the position along the normal (y) direction by A and the position along the spanwise (z) direction with either w-w^* (before the necking point) or w (after the necking point). Accounting for the non-contributing width (w^*) in the normalization is crucial for obtaining the convergence. After the necking point, the effect of the noncontributing width is diminished.

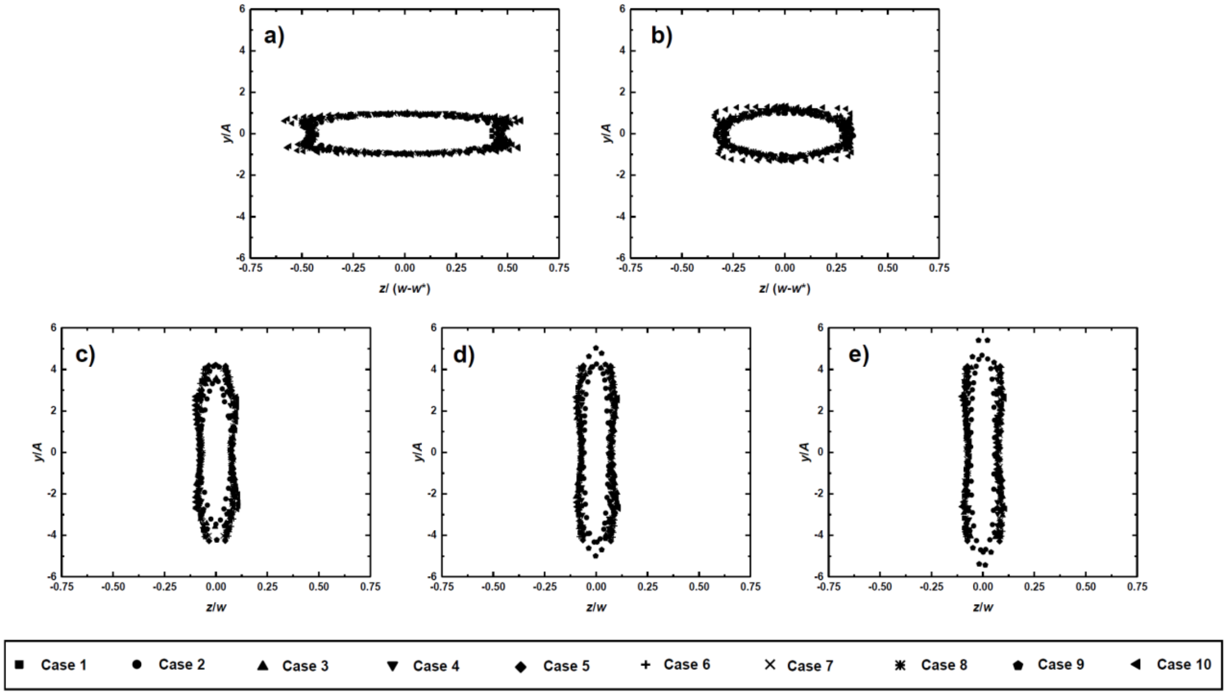

Figure 4.16 Jet boundaries projected on the y-z plane at different streamwise locations (a) $x/(Aw)^{1/2} = 0.07$, (b) $x/(Aw)^{1/2} = 0.29$, (c) $x/(Aw)^{1/2} = 0.86$, (d) $x/(Aw)^{1/2} = 1.14$, and (e) $x/(Aw)^{1/2} = 1.43$.

The transition from the contracting to the expanding region observed in the present study resembles the axis-switching phenomenon in non-circular jets [104]–[108]. In these past studies, the deformation of jet structures and subsequent development of axis switching is associated with the induced velocities of streamwise vortex pairs. The occurrence of this phenomenon is not unique; for instance, up to three axis switchovers are reported by Hussain & Husain [106] for a single jet. The first one is typically the most prominent, whereas the second and third switchovers take place much further downstream and are usually much weaker. Similar to our findings, the location of the first switchover was shown to be directly related to the jet aspect ratio (Krothapalli *et al.* [108]). The uncertainty in these measurements, however, was large.

4.5 Summary

We conducted a combined experimental and numerical study on the three-dimensional geometry of the induced mean jet downstream of a pitching cantilever plate and correlated it with the transient vortex behavior in the wake. Our results showed that the time-averaged velocity field forms two distinct regions in the wake identified by their shrinking or expanding nature. The first region extends from the trailing edge to a downstream distance of ~ $0.55(Aw)^{1/2}$, called the necking point. In this region, the induced fluid jet from the trailing edge shrinks linearly in the spanwise direction towards the midspan line as the flow continues in the streamwise direction. The extent of the jet in the normal direction, however, remains contained within the tip-to-tip displacement of the trailing edge ($2A$) in this region. The velocity profile in this region is approximately uniform and directed in the forward direction with a magnitude of ~5.6 times the tip velocity (Af). The second region starts after the necking point. In this region, the jet boundary stops shrinking in the spanwise direction and forms approximately parallel surfaces $0.15w$ apart, and instead, expands abruptly in the normal direction. An important characteristic of the second region is the appreciable decay of the streamwise component of the velocity after the necking point.

To illustrate the physics behind the complicated shape of the mean jet, we investigated the transient vortex formation at the sharp edges of the cantilever. Our 3D visualizations demonstrated that the vorticity propagates into the wake in the form of curved coherent structures emanated from the trailing edge that are initially attached to the cantilever's trailing edge at the corners. These structures lose their coherency due to diffusion and consequently break as they move in the streamwise direction. The resulting sub-structures tilt as they are convected downstream and induce the flow confinement observed in the mean jet.

We systematically studied the effect of several geometric and vibrational parameters on the shape of the induced jet. Our results revealed that the amplitude and the width of the pitching plates are the primary factors affecting the shape of the mean jet. The frequency of the oscillations has minor effects on the mean jet geometry, although linearly affecting the magnitude of the velocity. We observed no significant influence from the length of the cantilevers. We further demonstrated that the jet boundaries for all the tested cases fall into convergent universal curves when the spatial coordinate system is normalized by appropriate parameters.

Findings presented in this work are of significant importance in applications such as electronics cooling using piezoelectric fans. Placement of the electronic components outside the jet boundary may result in inadequate heat dissipation and overheating of the components. The present study improves our understanding of the complicated geometry of the mean jet downstream of a pitching plate and provides us with the tools to investigate the effect of different plate geometries on the flow generation and power consumption of piezoelectric fans.

Chapter 5. Role of plate geometry in cooling performance of piezoelectric fans

5.1 Background

In the previous chapters, efforts have been made to understand and model the power consumption and fluid mechanics of piezoelectric fans. We investigated the power consumption mechanisms in piezoelectric fans and provided electromechanical models to partition and predict the contribution from each source. Through 2D and 3D numerical and experimental analysis, we also provided physical insight into the mechanisms involved in the vortex generation and propagation and their role in dictating the shape of the jet. These analyses, however, were limited to rectangular plates, with little attention to the effect of plate geometry on the flow generation and cooling performance of the fans.

Investigating the effect of plate geometry requires extensive knowledge of three-dimensional properties of the trailing edge vortices and their influence on the time-averaged jet. Previous studies [41], [42], [109]–[111] investigated the three-dimensional vortex shedding in the wake of pitching plates with different trailing edge geometries in a non-zero free stream using 3D particle image velocimetry (3DPIV) and numerical simulations. Although their observations about the vortex structures and time-averaged properties of the wake are affected by the free stream velocity and therefore cannot be completely generalized to piezoelectric fans, their conclusions about the thrust and efficiency of the motion provide valuable insight into the effect of trailing edge geometry on the overall performance of the pitching plates. Other studies investigated the forces acting on pitching plates. Shrestha *et al.* [36] performed a comprehensive study on the lateral vortex regimes in oscillating plates in quiescent water and their effect on the resulting hydrodynamic forces. Similarly, Bidkar *et al.* [58] studied the aerodynamic damping forces acting on rectangular piezoelectric fans and developed a general model based on inviscid fluid theory to predict the amplitude and frequency dependence of these forces.

In the present chapter, we investigate the effect of plate geometry on the air flow generation, power consumption, thermal performance, and efficiency of piezoelectric fans. We perform immersed boundary numerical simulations to elucidate the effect of the plate trailing edge and upstream geometry on the qualitative and quantitative behavior of the downstream jet of pitching plates. We next accompany these observations with thermal experiments and power measurements to provide an efficiency comparison between different plate geometries.

5.2 Experiment parameters and setup

The vibration characteristics of a thin plate are described by the frequency f and the amplitude A. The characteristic trailing edge velocity is defined as $u_{\mathrm{TE}} = fA$. The main length scale of the plate is its span, S. We consider thin plates where the plate thickness, δ, only has secondary effects on fluid-solid interactions. The aspect ratio of the plates, AR, is fixed at 1. The normalized amplitude, α, which represents the aspect ratio of the oscillation envelope, equivalent to the Keulegan – Carpenter number in similar studies [58], and the oscillatory Reynolds number, Re, are defined respectively as

$$\alpha = \frac{A}{S} \tag{5.1}$$

$$Re = \frac{u_{\mathrm{tip}}\, S}{\nu} = \frac{fAS}{\nu} \tag{5.2}$$

We use commercial piezoelectric elements as actuators (Steminc Inc., SMPF61W20F50) in this study. Plates with different shapes (figure 5.1) are manufactured in house and attached to the actuators using cyanoacrylate glue. Table 5.1 lists the relevant properties of the plates along with their resonance frequencies and amplitude ranges.

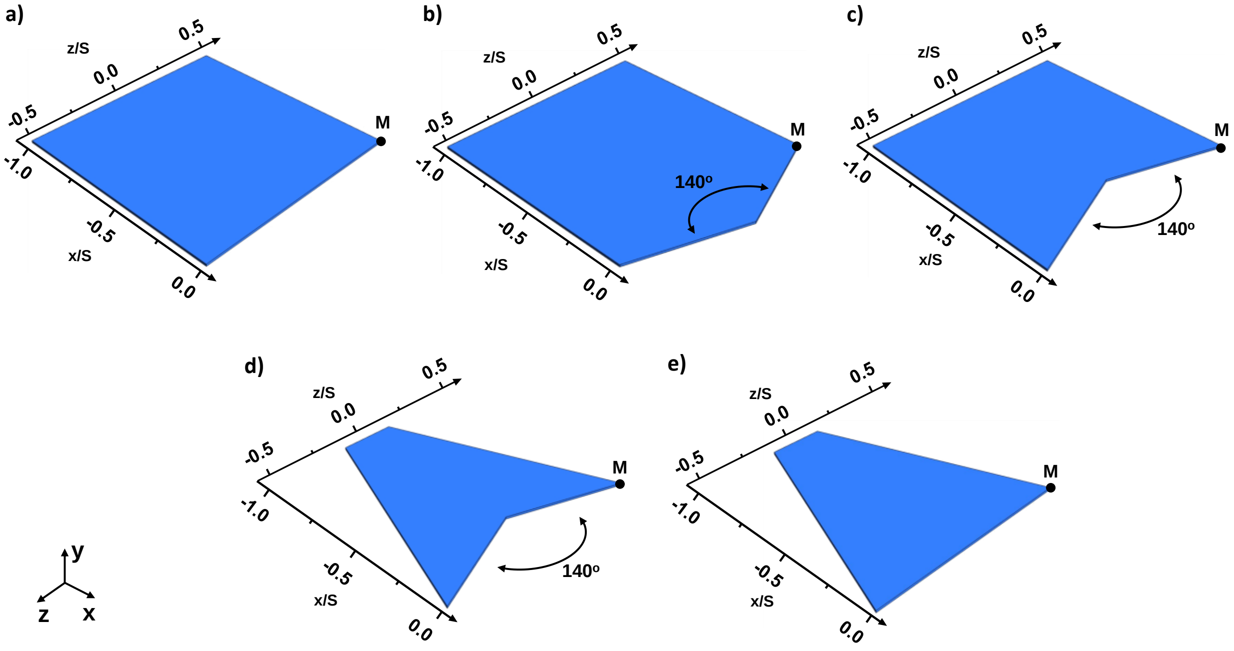

Figure 5.1 Different plate geometries used in the present study: (a) rectangular plate (b) convex plate (c) concave plate (d) concave – tapered plate (e) trapezoidal plate.

A function generator (Model 33220A, Agilent) is used to generate small amplitude (0.4V - 2V) pure sinusoidal voltage waves, which are then amplified using a high-voltage amplifier (Model PZD700A, TREK). The plate oscillation amplitudes are measured optically by tracking the displacements of the sharp corners at point *M* (see figure 5.1) at an uncertainty of 0.3 mm.

Table 5.1 Properties of the plates used in the present study

size, *S* (cm)	**Material and thickness (mm)**	**Shape**	**Normalized weighted area, Ψ/S^2**	**Resonance Frequency (Hz)**	**Voltage (V)**	**Amplitude range (mm)**
4	Steel (0.1)	Concave - Tapered	0.17	59	30, 50, 70, 100, 120, 150	3.5 - 12.5
		Concave	0.23	56		2.5 - 9.0
		Trapezoidal	0.27	44		2.0 - 9.5
		Rectangle	0.33	43		2.5 - 8.8
		Convex	0.48	44		1.8 - 8.5

Figure 5.2a schematically shows our experimental setup for characterizing the convective heat transfer coefficients. We use an aluminum block (75×75×12.7 mm^3) with a thin flexible heater attached to its back as a heated surface. The back and lateral sides of the thick block are insulated using Styrofoam and glass wool to create a nearly 1D isothermal condition. The heat loss due to conduction through the insulation is estimated to be less than 5% of the total supplied heat. A black spray paint with a known emissivity is used to coat the exposed front surface of the block. Five type K thermocouples are inserted into holes from the back of the block to measure temperatures (see figure 5.2a). The temperature profile is also obtained using an IR camera (figure 5.2b). The convective heat transfer coefficients and corresponding Nusselt numbers are obtained as

$$h = \frac{(Q_{\text{total}} - Q_{\text{rad.}})}{L_b^2\,(T_{\text{s}} - T_\infty)} \tag{5.3}$$

$$Nu = \frac{h\,L_b}{k_{air}} \tag{5.4}$$

where Q_{total}, $Q_{\text{rad.}}$, L_{b}, k_{air}, T_{s}, and T_∞ represent the total power input to the heater, heat loss due to radiation, length of the heated block (= 75 mm), thermal conductivity of air, surface temperature, and air temperature, respectively. Because Gr/Re_{L}^2 is of the order of 0.01 in all our experiments, where Gr is the Grashof number, we assume that natural convection has small effects.

Figure 5.2c shows the experimental setup used to measure thrust forces generated by oscillating plates. The setup includes a weight scale (Model Adventurer Pro, Ohaus) with a resolution of 0.0001 g enclosed inside a plastic enclosure. The scale measures the force exerted by airflows generated by the plates on its flat top surface (figure 5.2c).

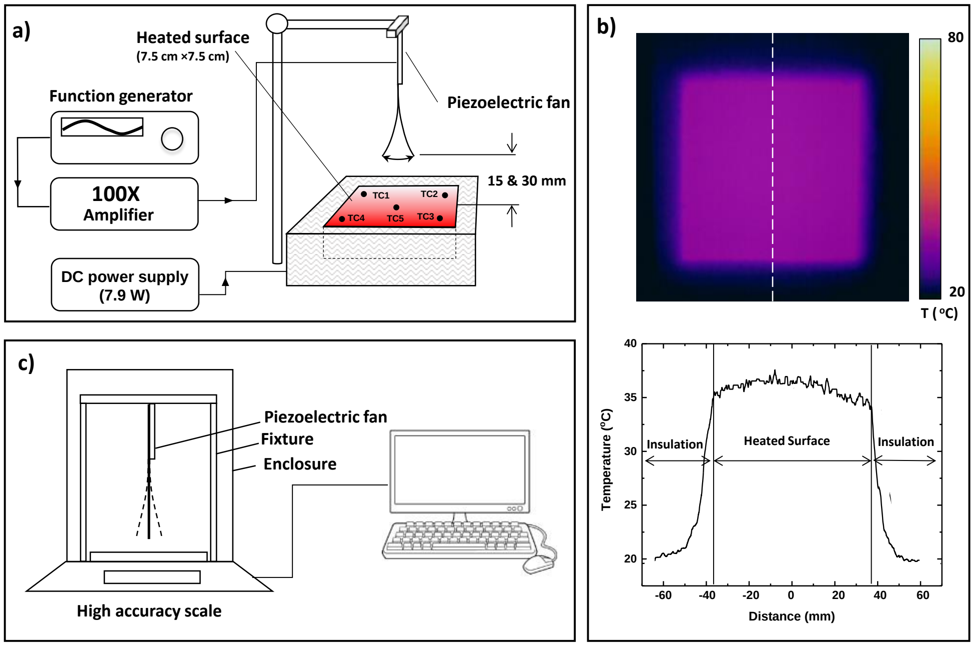

Figure 5.2 (a) Schematic of the experimental setup to measure convective heat transfer coefficients. (b) A representative Infrared thermography result. The graph below shows the measured temperature profile along the white dashed line. (c) Schematic of the experimental setup to measure thrust force.

5.3 Numerical simulations

We use three-dimensional numerical simulation based on the immersed boundary method [112] to predict velocity fields downstream of the plates with different geometries. The dimensions of the simulation domain are $3S \times 2S \times S$ (figure 5.3a). A domain size-independence study and PIV visualization were used to verify that the domain size used is large enough to capture the desired properties of the jets while avoiding complicating effects of the boundaries. Zero relative pressure is specified as the boundary condition on the outer walls.

Further details about our numerical model and its validation are provided in [113]. Briefly, we approximate the oscillatory motion of the plates as a rigid solid rotating about a pivot point at its base. We use tetrahedral meshes whose sizes vary along the trailing edge: 0.005*S* in 7 spheres of radius 0.125*S* centered along the trailing edge, 0.01*S* in 3 intermediate spheres of radius 0.25*S*, and 0.025*S* in the rest of the domain (figure 5.3b). Each numerical simulation run covered 20 cycles of plate oscillation. The velocity fields are averaged from cycles 11 to 20 to capture steady periodic conditions. The power consumption due to drag force acting on the plates is calculated by integrating work done by the pressure difference between the upper and lower sides of the plates. The transient vortex structures discussed in section 5.4.1 are extracted from the last cycle.

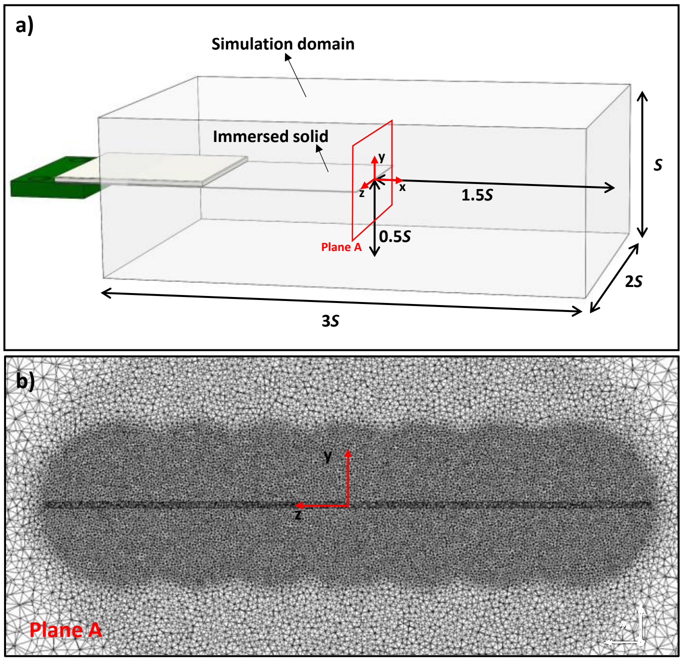

Figure 5.3 (a) Applied boundary conditions in the numerical simulations (b) a representative mesh size at the trailing edge of the rectangular plate.

5.4 Results and discussions

5.4.1 Airflow generation and jet topology

Figures 5.4 and 5.5 show the time-averaged streamwise velocity downstream of the pitching plates with different geometries. The maximum streamwise velocity near the trailing edge correlates with u_{TE} in a similar fashion for all the geometries (~6 u_{TE}), consistent with observations from previous studies [113] [44], [98], [114]. The jet boundaries for all the cases exhibit a shrinking-expanding (i.e. axis switching) behavior, which is typical of pitching plates operating in both quiescent media [113] and finite freestreams [26], [27], [37], [110]. This dual-region behavior has been attributed to the transient interactions between vortex structures generated in each half cycle and their consequent breakdown downstream. The streamwise length of the shrinking region of the jet in a quiescent medium, as indicated by the location of the axis switching point (figure 4a, also see [113]), is a function of the plate's normalized amplitude [113] whereas it is a strong function of the fluid velocity, and hence the Strouhal number, in the presence of a freestream. The jet is more stretched in the streamwise direction when a freestream is present [26], [27], [37], [110].

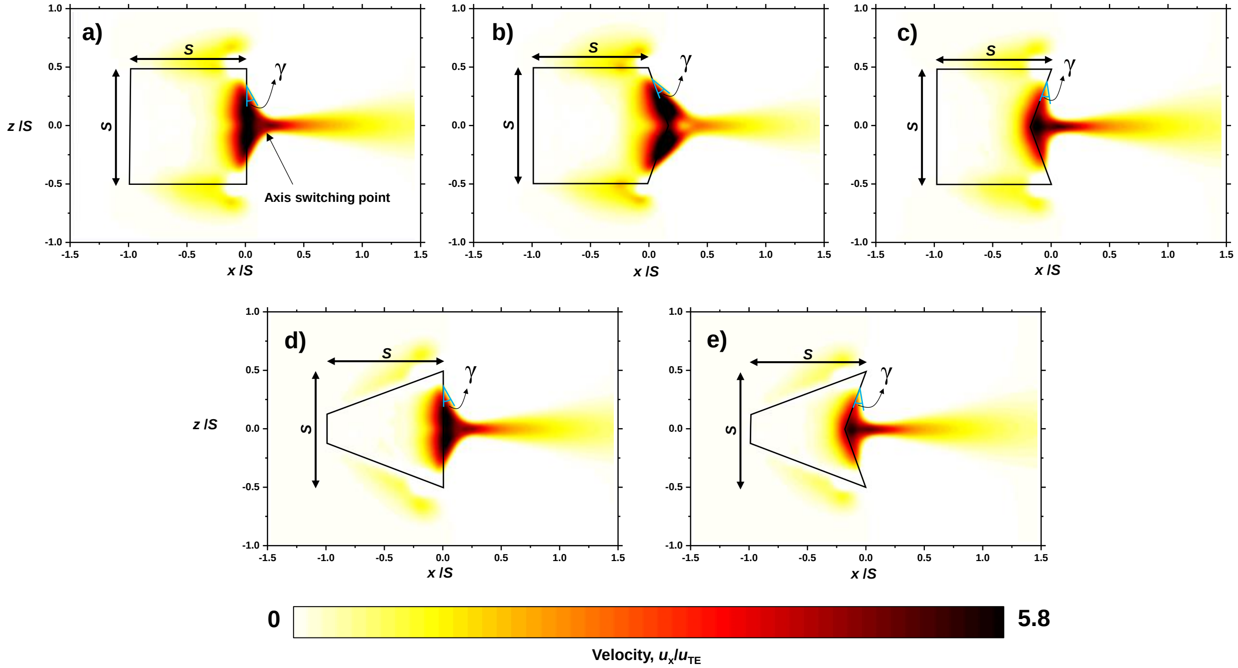

Figure 5.4 The streamwise (*x*-direction) component of the time-averaged velocity field downstream of the plates with different geometries on the *x*-*z* plane (*y* = 0). *α* = 0.123 and *Re* = 230 for all the plates.

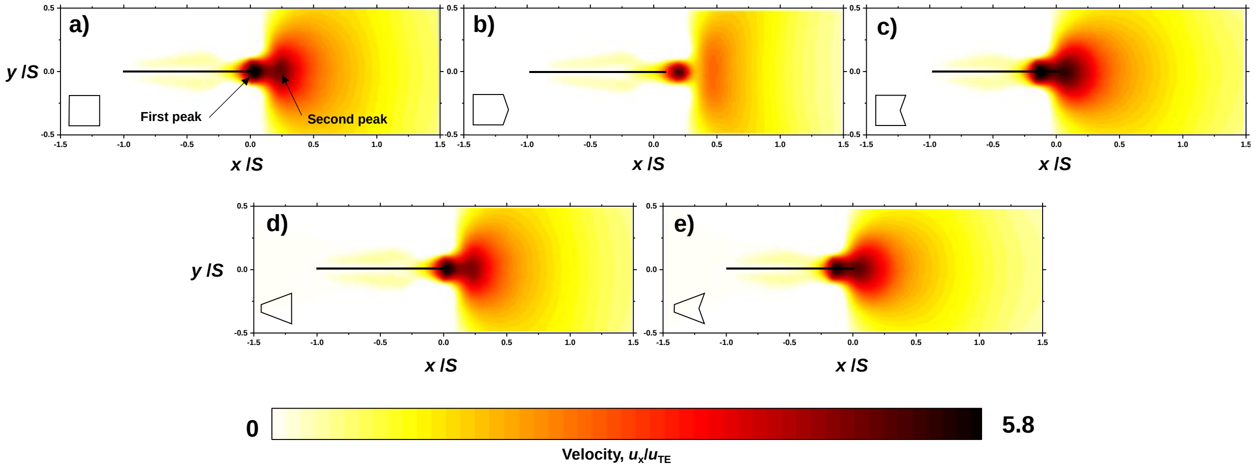

Figure 5.5 The streamwise (*x*-direction) component of the time-averaged velocity field downstream of the plates with different geometries on the *x*-*y* plane (*z* = 0). *α* = 0.123 and *Re* = 230 for all the plates.

The predicted velocity profiles in figure 5.4 show that the shape of the trailing edge significantly influences the jet boundary. Before it undergoes axis switching, the jet conforms to the contour of the trailing edge. In particular, the angle between the jet boundary and the trailing edge (denoted as γ in figure 5.4) remains nearly constant. This causes the jet boundary to get broader for the convex trailing edges. In contrast, the jet boundary shrinks towards the mid-span plane for the concave trailing edges (figure 5.4). Also, due to the increased spanwise spread of the flow, the second velocity peak immediately after the axis switching point (figure 5.5) becomes much less pronounced downstream of the convex trailing edges. Farther away from the axis switching point, the effect of the trailing edge becomes less noticeable and both the jet boundary and the streamwise velocity magnitude are nearly identical for the different plates.

The observed trailing edge dependence of the time-averaged jets, especially in the vicinity of the trailing edge, can be attributed to the transient evolution of the vortex structures and their influence on the flow field. To examine this further, we show in figure 5.6 transient vortex structures emanating from the trailing and lateral edges of the plates for a full cycle of oscillations. The phase angle φ in these figures is specified in terms of the vertical location of the trailing edge, $y = A \sin(\varphi)$. The vortex cores are identified using the Q-criterion method [115] and the colormaps indicate the magnitude of the spanwise vorticity ω_z on the structures.

For all the plate geometries, vortices first emanate as coherent structures that follow the contour of a trailing edge. These structures break down as they travel downstream and approximately half a cycle later form two sub-structures that are significantly tilted about the x-axis and move along diverging trajectories (Trajectory 1 and Trajectory 2 in figure 5.6), corresponding to transport above and below the x-z plane. This vortex breakdown and subsequent tilting and bifurcation of the substructures concentrate the flow towards the midspan in the *y*-z plane and induce a significant flow expansion in the *x*-*y* plane [26], [27], [37], [110], [113].

In addition, the relative proximity of these sub-structures is affected by the curvature of the trailing edge. The substructures become further apart as the convexity of the plates increases. This explains the broader jet boundary in the spanwise (*z*) direction for the convex plate than the flat and concave plates (figure 5.4) because the time-averaged jet boundary in the shrinking region conforms to the substructure trajectories [113].

We also note that these substructures are confined to a relatively short distance ($x/S \sim 0.25$) downstream of the trailing edge in the quiescent medium of our simulation, coinciding with the axis switching points of figure 5.5. This is in contrast to the results from previous studies performed in the presence of a finite free stream. There, the vortex structures begin to diffuse only after being transported a large distance downstream, approximately $x/S \sim 3$ for low Strouhal numbers (high freestream relative to trailing edge velocity) [109], [110]. In the asymptotic limit of $St \rightarrow \infty$, however, it was observed that the trailing edge vortex structures break down more rapidly and over a shorter distance, consistent with our numerical simulation results.

Figure 5.6 further suggests that the coherence of the vortex structures decreases with increasing convexity of the trailing edge; the resulting substructures in the convex plate dissipate more quickly than those of other plate geometries, consistent with experimental observations of Van Buren *et al.* [109] for pitching plates in a finite freestream.

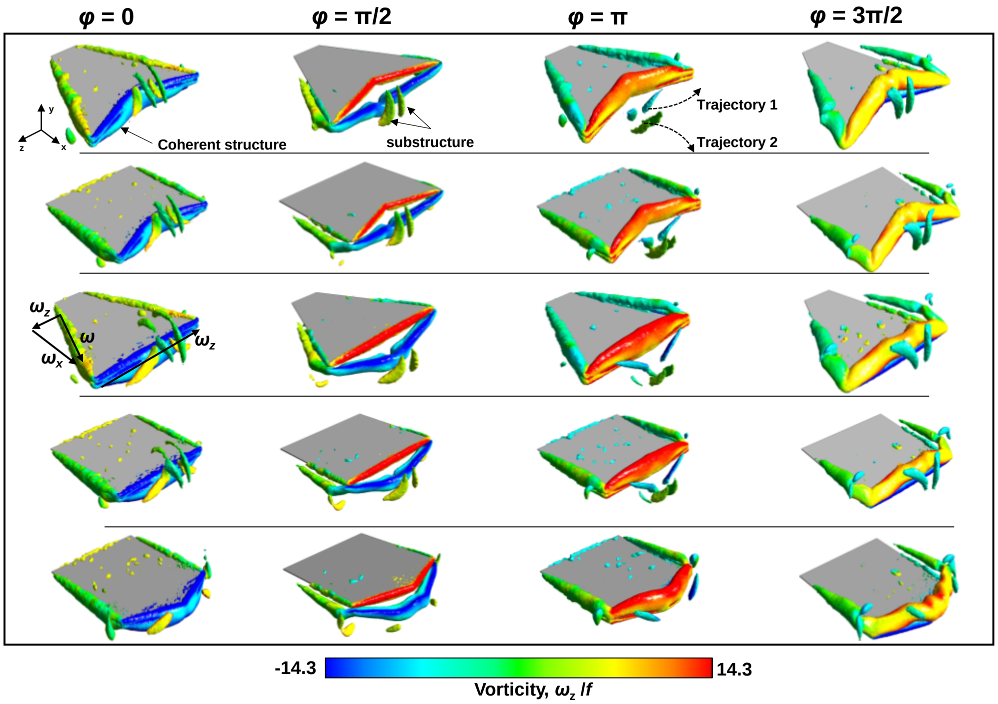

Figure 5.6 Three-dimensional vortex structures obtained from the numerical simulation during one full cycle of oscillations for different plate geometries. α = 0.123 and *Re* = 230 for all plates.

Figure 5.7a shows the calculated time-averaged volumetric flow rates, Ω, of jets through a y-z plane ($y \in [-0.5S, 0.5S]$, and $z \in [-S, S]$) at different streamwise locations. This flowrate has practical implications on convective heat transfer and thrust force. The streamwise position x is normalized with the square root of the oscillation envelope $(AS)^{0.5}$ because the streamwise extent of the jet is influenced to similar degrees by the oscillation amplitude and the plate width for the plate aspect ratio of our study [113]. For all the plate geometries, we observe a rapid decline in the flowrate due to rapid changes in the velocity direction after the necking point (in the expansion region) and viscous diffusion. Figure 5.7a also suggests that the flowrate in the near field (~ $x/(AS)^{0.5} < 1.5$) is significantly affected by the plate geometry. For instance, at $x/(Aw)^{0.5} = 1$, the flowrate downstream of the convex plate is almost twice as high as that of the concave-tapered plate. As we approach the far-field ($x/(Aw)^{0.5} > 1.5$) this difference is still present, albeit less pronounced.

To further explain the difference in the flow generation capability of the plates, we calculate the vortex core strength (circulation), Γ_z, using the area integral of vorticity inside the vortex structures shown in figure 5.6 at $\varphi = 0$. Figure 5.7b shows that Γ_z exhibits a direct correlation with the convexity of the trailing edge and the upstream surface area of the plates. This is reasonable because in oscillating cantilevers, the vorticity originates in the upstream boundary layer due to the no-slip condition [116]–[118]. Reducing the upstream area by tapering the plates or concaving the trailing edge suppresses vorticity generation and thereby flow generation [31], [98]. In addition, tapering the plates adds a vorticity component opposite to that of the trailing edge vortices (see figure 5.6, tapered plate at $\varphi = 0$) to the lateral vortices. This slightly weakens the vortices at the corners of the plates (at $a/L_{TE} = 0$ and 1 for the trapezoidal and concave-tapered plates in figure 5.7b).

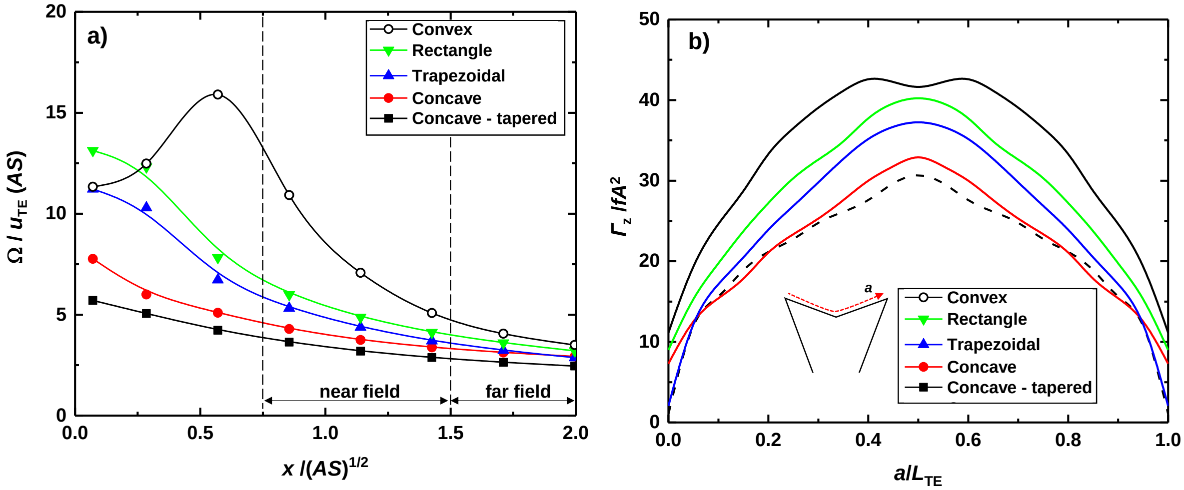

Figure 5.7 (a) The induced flowrate passing through normal planes at different streamwise locations. (b) the trailing edge vortex strength as a function of location along the trailing edge (a is a length marching parameter and L_{TE} is the length of the trailing edge).

5.4.2 Power consumption analysis

Power consumption in plates oscillating in a viscous fluid contains contributions from drag, inertia (due to the mass of the plate and the added mass of the fluid), and structural damping within the plate. The last contribution is very often negligible [46], [76]. In principle, the net power consumption associated with the inertia of the plate is zero for an ideal actuator with an electromechanical conversion efficiency of unity. In the present study, we limit ourselves to the dissipative portion of the power consumption due to drag force on the oscillating plate. We define the dimensionless drag power coefficient as

$$C_{P,d} = \frac{P_d}{\rho_a A^3 f^3 S^2} \tag{5.5}$$

where P_d and ρ_a are the drag power and air density, respectively.

Figure 5.8a shows the dimensionless drag power calculated from our numerical simulation results. The convex plate dissipates up to three times as much drag power as the concave-tapered plate when oscillating with the same frequency and amplitude. To capture this trend, we define a modified dimensionless drag power as

$$\hat{C}_{P,d} = \frac{P_d}{\rho_a A^3 f^3 \Psi} \tag{5.6}$$

Here, Ψ is the weighted surface area of the plates defined as

$$\Psi = \iint \frac{x^2}{s^2}\, dxdz \tag{5.7}$$

The weighted surface area accounts for the fact that the regions of a plate closer to the trailing edge have more contribution to the overall power consumption because both the force and velocity increase almost linearly with the distance from the leading edge. The weighted surface areas of the plates used in the present study are listed in table 5.1. Figure 5.8b shows the modified dimensionless drag power, which is approximately the same (~ 104) for all the plate geometries.

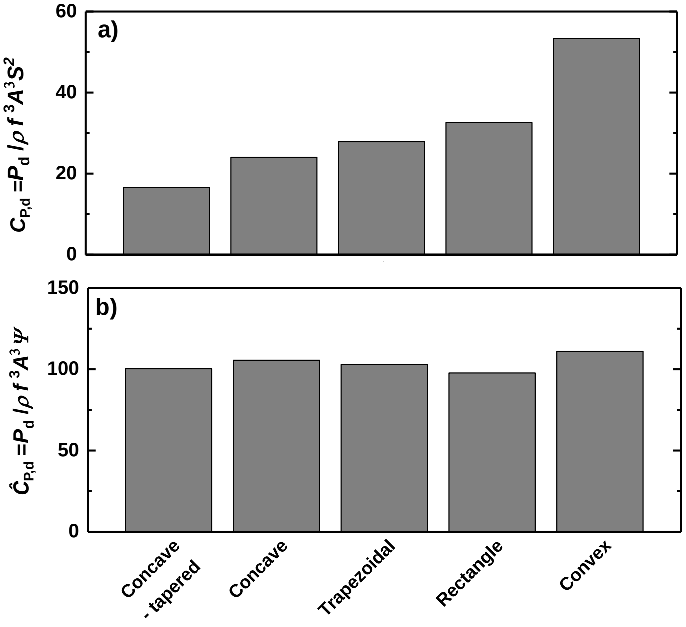

Figure 5.8 (a) Dimensionless drag power $C_{p,d}$ obtained from our numerical simulation results (b) Modified dimensionless drag power $\hat{C}_{p,d}$ for plates with different geometries.

5.4.3 Convective heat transfer

To make meaningful comparison of the convective heat transfer performance of the different plates, we first isolate the amplitude and frequency dependence of our measured Nusselt numbers, which is captured in their Reynolds number dependence. The Reynolds number dependence of Nu may be captured using the power-law, $Nu = K\,Re^n$, with the exponent n being 0.65 for the far field and approximately 0.8 for the near field (figure 5.9). We may view the proportionality factor K, which itself is a function of the plate geometry, as a measure of the effectiveness of each plate in convective heat transfer. The stronger *Re* dependence in the near field can be attributed to the enhanced mixing by the trailing edge oscillating near the stagnation point. The mixing effects become weaker at the far field due to viscous diffusion.

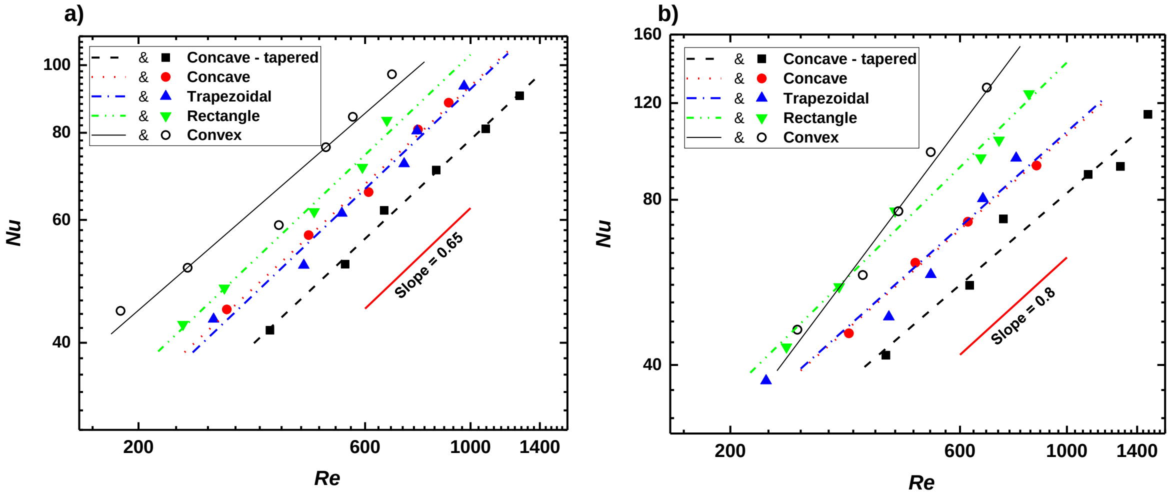

Figure 5.9 *Nu* vs. *Re* for (a) far-field and (b) near-field thermal experiments.

Figures 5.10a and 5.10b show the proportionality factor *K* for each of the plate geometries in the far field and the near field, respectively. Also shown for reference is the dimensionless drag power $C_{p,d}$ for each geometry, which is essentially proportion to Ψ for the fixed *A*, *f* and *S*. We observe that *K* qualitatively follow the similar trend as the airflow generation capability of sections 5.4.1 and 5.4.2. That is, at the same frequency and amplitude, the convex plate generates more airflow and hence stronger convective heat transfer but at a higher power consumption.

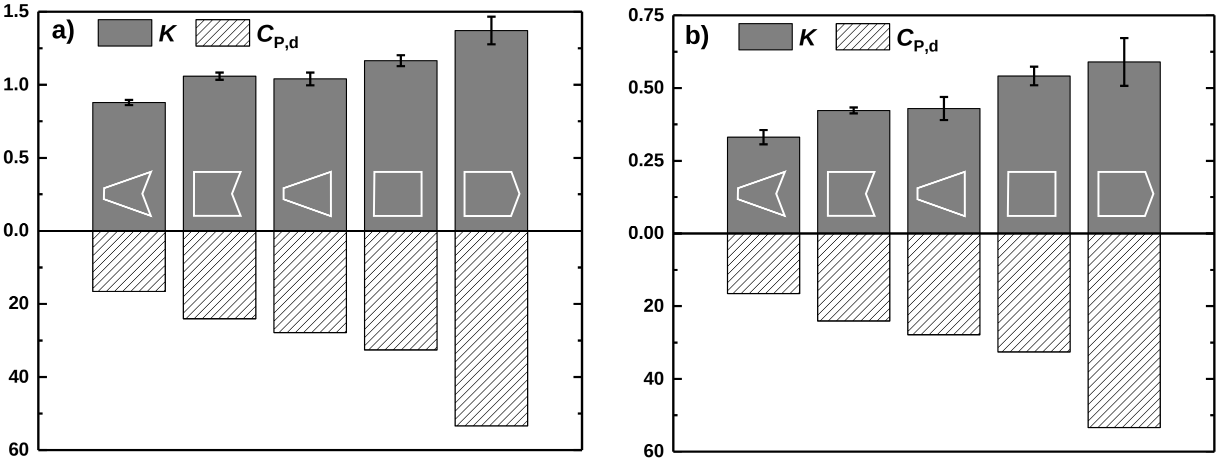

Figure 5.10 (a) Far-field and (b) near-field proportionality factor K for plates with different geometries. The error bars represent the standard deviation in K due to experimental uncertainty and curve fit quality.

Next, we convert these results to compare the power consumptions necessary to achieve the same convective heat transfer performance. Using the Reynolds number dependence of the Nusselt number, we first set the oscillation amplitude for each plate to be A' such that we obtain the same target Nusselt number, Nu', for a given oscillation frequency:

$$A' = \left(\frac{Nu'}{K}\right)^{1/n} \frac{\nu}{fS} \tag{5.8}$$

The corresponding power consumption is

$$P_d{}' = C_{P,d}\rho_a (A'f)^3 S^2 = C_{P,d}\rho_a \left(\frac{\nu}{S}\right)^3 \left(\frac{Nu'}{K}\right)^{3/n} S^2 \tag{5.9}$$

One may compare the plates with different geometries in terms of their convective heat transfer performance per unit power:

$$\eta = \frac{Nu'}{P_d{}'} = \left[\frac{(Nu')^{1-3/n}}{\rho_a \frac{\nu^3}{S}}\right]\left[\frac{K^{3/n}}{C_{P,d}}\right] \tag{5.10}$$

We then define the figure of merit M as

$$M = \frac{K^{3/n}}{C_{P,d}} \tag{5.11}$$

This figure of merit is shown in figures 5.11a and 5.11b for the far field region and the near field region, respectively.

These results indicate that the power efficiency generally improves with the increasing convexity of the trailing edge ($M_{\text{concave}} < M_{\text{rectangle}} < M_{\text{convex}}$) and the increasing upstream surface area ($M_{\text{trapezoidal}} < M_{\text{rectangle}}$ and $M_{\text{concave-tapered}} < M_{\text{concave}}$). In other words, referring back to the discussion in section 5.4.1, we observe that the enhancement in the flow generation capability of the plates more than offsets the associated rise in power consumption. As an example, for a given target Nusselt number, the concave-tapered plate consumes more than twice as much power as the convex plate in the far field and almost three times as much power as the rectangular plate in the near field.

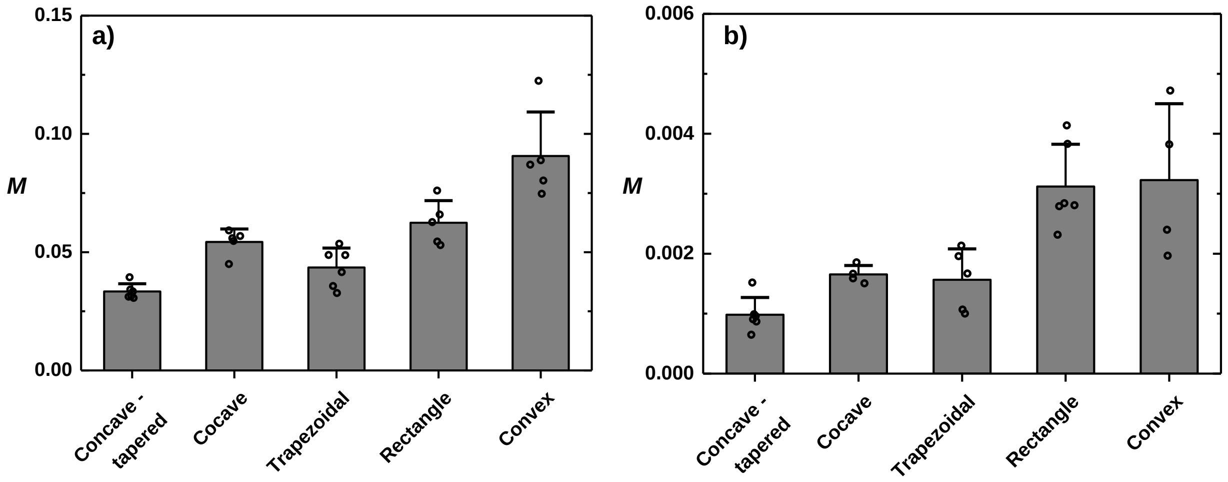

Figure 5.11 Figure of merit, M, of the pitching plates in (a) Far-field and (b) near-field configurations. The error bars represent the standard deviation in the experimental data due to experimental uncertainty and curve fit quality.

5.4.4 Thrust performance

To further characterize the effects of the plate geometry on generated air flows, we measure the force, F, exerted by the airflow generated by an oscillating plate on an opposing flat surface. The near field configuration was used to ensure that the entire jet momentum is transferred to the sensor surface and the measured values thereby approximate the total thrust force generated by the oscillating plate.

Figure 5.12 shows the thrust power, $F\ u_{\mathrm{TE}}$, as a function of the power consumption. The inset shows the associated power efficiency, $\eta_{\mathrm{T}} = F\ u_{\mathrm{TE}} / P_{\mathrm{d}}$, calculated from the slopes of the linear fits to the data. The power efficiencies for thrust follow closely the figure of merits for convective heat transfer shown in figure 5.11b.

Our results are consistent with the findings reported in previous studies on the effects of the trailing edge shape on thrust generation. Van Buren *et al.* [109] reported a maximum enhancement in thrust performance of approximately 40% by changing the trailing edge angle from 45^{o} (concave) to 120^{o} (convex). Using immersed boundary numerical simulations, Hemmati *et al.*

[110] observed approximately 30% increase in the thrust coefficient by increasing the trailing edge convexity. They correlated this enhancement with the rate of wake vortex contraction. Similar results were reported in Zhang *et al.* [111].

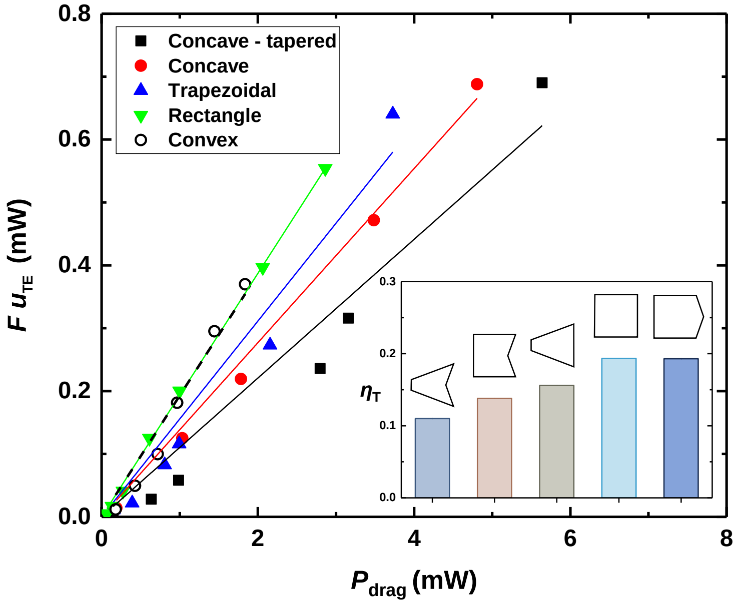

Figure 5.12 Thrust power, F u_{TE}, as a function of the power consumption for the different plate geometries examined in this study. The lines represent linear fits to the data. The inset demonstrates the power efficiency for thrust obtained from the slopes of the linear fits.

5.5 Summary

We conducted a combined experimental and numerical study to investigate the effect of plate geometry on the flow generation, power consumption, and convective thermal performance of pitching plates in a quiescent fluid. Our immersed boundary numerical simulations revealed that the three-dimensional shape of the time-averaged jet in the wake of different plates is strongly influenced by the curvature of the trailing edge. This shape-dependence was further correlated with the difference in the strength and trajectory of the transient vortex structures emanating from the sharp edges of the plates.

Our flow rate measurements showed that the airflow generation capability of the plates improves with increasing trailing edge convexity and upstream surface area, which translates to enhanced convective thermal performance. The difference in the flow rates is more pronounced close to the trailing edge (~ $x/(AS)^{0.5} < 1.5$) and reduces further downstream (~ $x/(AS)^{0.5} > 1.5$). Similarly, the power consumption due to the drag forces on the plates increases linearly with the weighted surface area of the plates, Ψ, suggesting a counterbalancing effect in the power efficiency from these two factors. We found that the enhancement in thermal performance of the plates outweighs the associated rise in power consumption and in general the power efficiency of the plates improves with increasing the convexity of the trailing edge and upstream surface area in both near-field and far-field configurations.

The present study improves our understanding of the role of plate geometry in the flow generation and heat transfer enhancement using oscillating cantilever plates. Findings from this study provide a guideline for the optimized design and selection of plate geometry for applications such as piezoelectric cooling enhancement that highly rely on airflow generation downstream of the pitching plates.

Chapter 6. Thermal enhancement in piezoelectric fans using roughened surfaces

6.1 Background

In the previous chapter, we investigated the effect of the oscillating plate size and geometry on the thermal and power efficiency of the fans and provided useful guidelines for optimal plate shape selection. These results, however, were obtained considering a flat plate as the heating source.

For many decades, smooth surfaces have been commonly used in thermal management components due to their ease of construct. Although smooth surfaces can be sufficient for many applications, there has recently been a strong push to improve the heat transfer performance of these surfaces so as to extend their range of applications and capabilities. Recent innovations in the manufacturing technologies such as precision machining, powder metallurgy, 3D printing metal composites [119] and Direct Laser Metal Sintering (DLMS) [120], created new opportunities for economic and time efficient mass production of complicated roughened surfaces, and thus, sparked more research motive to test and compare the heat transfer performance of such surfaces.

Previous studies in this area have found that by introducing roughness to smooth surfaces, one can notably increases the convective heat transfer coefficient from these surfaces, especially at high Reynolds flows. Gao and Sundén [121] measured the heat transfer performance and pressure drop of rib-roughened surfaces in a duct flow experiment setup and observed a factor of two increase in the Nusselt numbers compared with the flat surfaces in the same configuration. Bopche and Tandale [122] used U-shaped turbulators on the absorber surface of an air heater duct at Reynolds number range from 3800 to 18000 and observed a heat transfer enhancement by 2.82 times compared with flat surfaces. Similarly, Thianpong *et al.* [123] and Yang and Chen [124] studied the heat transfer characteristics of roughened surfaces with triangular ribs in channel flows of Reynolds number 5000-22,000. They observed a factor of 4 improvement in the heat transfer performance of their surfaces at the expense of a large pressure drop in their channel due to the large roughness of the tested surface. Other surfaces such as sinusoidal wavy walls [125] and dimpled-roughened surfaces [126], [127] were also studied before.

More recently, roughened surfaces with machined fish-scale patterns started to gain attention due to their biomimetic structure and slightly higher performance. Chang *et al.* [128]–[134] and Zhou *et al.* [135]–[137] reported 25% improvement compared with ribbed and dimpled surfaces. These experiments, however, were conducted at high Reynolds numbers, and therefore, cannot be generalized to low Reynolds applications such as electronics cooling and packaging where small-scale components and low-velocity flows are of main interest.

The present study aims to investigate the effect of the heat source roughness on the thermal and power performance of the piezoelectric fans as another means of improving their efficiency [138].

6.2 Experimental setup

The scaled surfaces are fabricated by CNC machining bulk 6061 aluminum bars. Figure 6.1a shows the dimensions of thus prepared surfaces. Scaled surfaces with feature heights of e = 0.46 m, 0.75 mm, and 1 mm are tested in this study.

Flat and scaled surfaces are tested in a rectangular channel setup as shown in figure 6.1b. Compressed air with constant temperature of 21^{o}C is injected to the channel. Different levels of flow straighteners are used to ensure a uniform velocity profile. Due to the large entrance length of the flow in the tested Reynolds numbers (1~2.4 m), the uniform velocity profile is retained in the heat transfer test section.

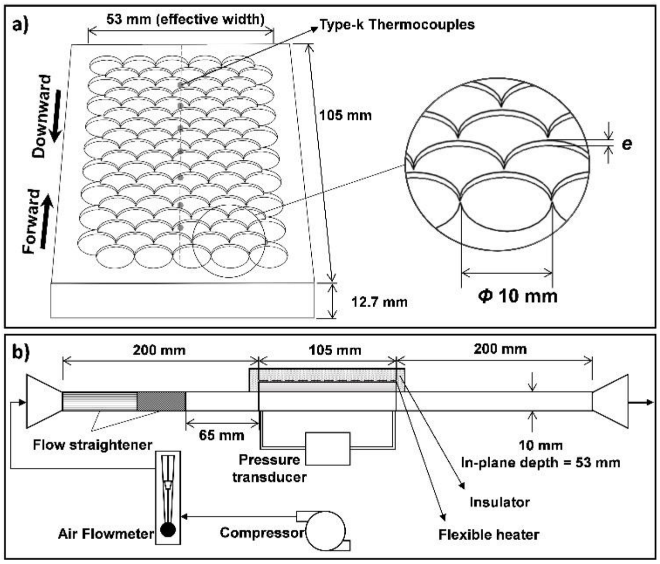

Figure 6.1 Schematic of the channel flow setup used in this study.

Surfaces are electrically heated using a flexible heater attached to their flat side. Heat loss from the other side of the surfaces is minimized using Styrofoam insulation. We measure the temperature along the centerline of the surfaces using 7 type-k thermocouples spaced 10 mm from each other. The surfaces are coated with Kylon Colormaster No.1602 with a known emissivity of 0.95 to calculate the heat transfer rate through radiation.

The Reynolds number in the channel, Re_c, and the average Nusselt number, Nu_c, are estimated as

$$\boldsymbol{Re_{\mathrm{c}}} = \frac{\bar{U}_c\, D_{h,c}}{\nu} \tag{6.1}$$

$$\boldsymbol{Nu_{\mathrm{c}}} = \frac{(Q_{\mathrm{total}} - Q_{\mathrm{rad.}})\, D_{h,c}}{A\, k_{air}\, (T_s - T_m)} \tag{6.2}$$

where $\bar{U}_c$, $D_{h,c}$, and v in Equ. (6.1) are the average air velocity in the channel, hydraulic diameter of the duct, and kinematic viscosity of air, respectively. In Equ. (6.2), Q, A, k_{air}, T_s, and

T_m represent the total heat power from the heater, the exposed area of the surfaces, thermal conductivity of air, surface temperature, and average air temperature, respectively. Due to the large thermal conductivity of aluminum, no significant temperature gradient was observed on the heated surface.

Figure 6.2a shows the schematic of the experimental setup for the piezoelectric fan and scaled surface combined configuration. A symmetric scaled surface is used due to the piezoelectric fan's symmetric air flow on opposing walls (see figure 6.8 and 6.9). The area of the heated surfaces in this experiment (75×75 mm^2) and the input heat power are equal to that of the tested surface in channel setup.

Three piezoelectric fans are positioned in an orthogonal orientation relative to the surfaces with 5 mm distance from each other. The distance from the tip of the fans to the heated surfaces is 5 mm. Fans operate at the same frequency and amplitude. Five type-k thermocouples are located inside of the test surfaces to monitor the temporal temperature changes until steady state. An IR camera (FLIR thermovision A40) is used to obtain the temperature distribution on the heated surfaces. The aluminum surfaces are chosen thick enough (12.7 mm) to create an isothermal boundary condition at the outer surface. Figure 6.2 shows about $\pm 1^{o}$C temperature difference on a representative temperature profile obtained from the IR thermography.

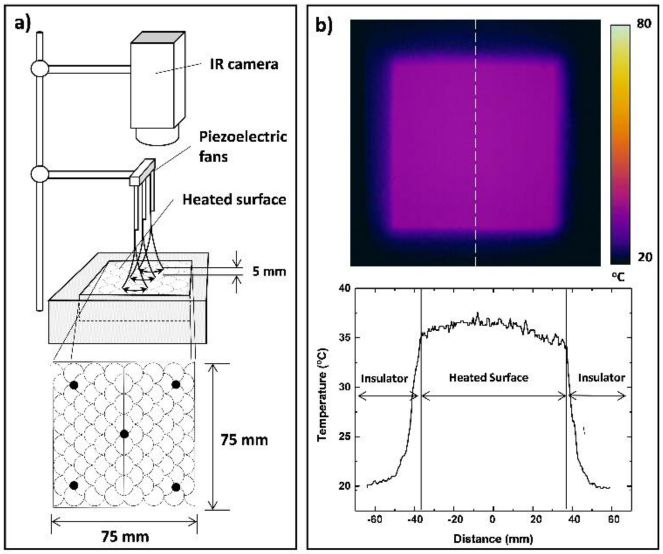

Figure 6.2 a) Combined piezoelectric fan and scaled surface performance measurement setup. The feature height used in this experiment is e = 1 mm. The black dots indicate the position of the monitoring thermocouples. b) a sample IR thermography result. The graph shows the measured temperature along the white dashed line. We use the temperature gradient in the insulator to estimate the heat loss from the back and lateral sides of the tested surfaces.

The estimated loss in both experiments is less than 10% of the total supplied heat, as quantified by measuring the temperature gradient in the insulator using IR thermography (figure 6.2b).

The convective heat transfer coefficient due to the fan's operation, h_{fan}, is calculated as

$$\boldsymbol{h}_{\mathbf{fan}} = \frac{(\boldsymbol{Q}_{\mathbf{total}} - \boldsymbol{Q}_{\mathbf{rad.}})}{\boldsymbol{A}\,(\boldsymbol{T}_{\mathbf{s}} - \boldsymbol{T}_{\infty})} \tag{6.3}$$

To be consistent with the definition of Nusselt number in impinging jets, we use the following correlation for the average Nusselt number for the combined piezoelectric fan and scaled surface experiment.

$$\boldsymbol{Nu}_{\mathbf{p}} = \frac{\boldsymbol{h}_{\mathbf{fan}}\,\boldsymbol{D}_{\boldsymbol{h},\boldsymbol{p}}}{\boldsymbol{k}_{\boldsymbol{air}}} \tag{6.4}$$

$D_{\text{h,p}}$ is the hydraulic diameter of the fan's envelope of oscillations [139].

The vibration characteristics of the piezoelectric fans are described by their frequency, *f*, and amplitude, A_p. The relevant length scale to the physics of the problem is the gap, g, between the fan and the surfaces. The width, length, and thickness of the fan blades only have secondary effects on the induced flow over the surface. We suggest the following definition for the Reynolds number associated with the piezoelectric fan's oscillations, Re_p:

$$\boldsymbol{Re}_\mathbf{p} = \frac{\bar{\boldsymbol{U}}_{\boldsymbol{p}}\,\boldsymbol{g}}{\boldsymbol{\nu}} \tag{6.5}$$

where $\bar{U}_\mathrm{p}$ is the average velocity on the heated surfaces obtained from numerical simulations.

We use commercially available piezoelectric fans (Steminc Inc., SMPF61W20F50). A function generator (Model 33220A, Agilent) is used to generate sinusoidal voltage waves, which are then amplified by using a high-voltage amplifier (Model PZD700A, TREK) before being fed to the piezoelectric actuator (figure 6.3a). The total power consumption of the piezoelectric fans is obtained using a method described in an earlier study [76].

We use Particle Image Velocimetry (PIV) to obtain a qualitative and quantitative measure of the velocity magnitude and jet profile upon impingement on the heated surface. The setup (figure 6.3b) consists of a 500 mW continuous wave laser (Hercules, LASERGLOW Technologies) with a wavelength of 532 nm. The laser beam is shaped into a light sheet using a cylindrical lens. We use a high-speed camera (Phantom VEO-640L) to capture the motion of particles suspended in the air. The frame rate is chosen such that at least 100 frames are captured per full period of the oscillations.

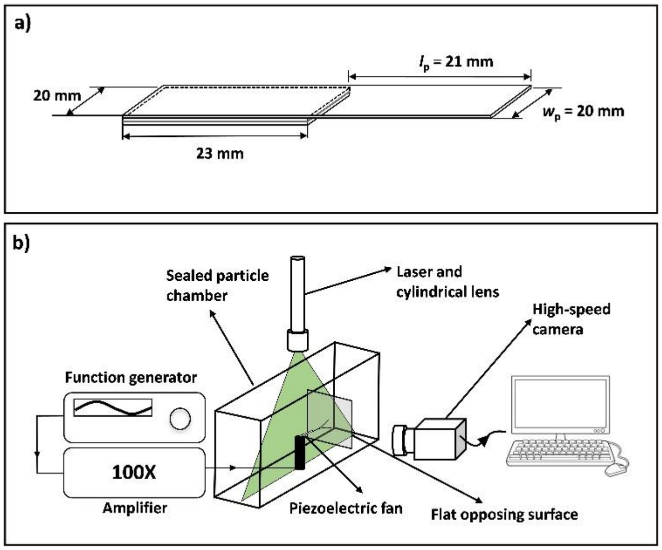

Figure 6.3 a) Dimensions of the piezoelectric fans. b) power measurement and PIV experimental setup.

PIV experiments are conducted in a transparent acrylic chamber, large enough to reduce interference from the side walls. Seeding particles are generated by heating a solution of water and glycerin (30% glycerin in volume) and injected into the chamber where they are allowed to settle for about a minute to minimize initial disturbances. The particle motions due to buoyancy are measured separately in the absence of an oscillating plate and deducted from velocity fields. An open-source software package (PIVlab) [78] is used to analyze the captured video images by cross-correlating the successive video frames to obtain the velocity profiles at each time instance.

6.3 Numerical simulations

Three-dimensional numerical simulations are done using the Immersed Boundary Method embedded in Ansys CFX to avoid computational overheads associated with re-meshing in moving mesh methods. The 3D simulation domain size is 6 cm × 4 cm × 4 cm, large enough to avoid any complicating effect at the boundaries. To help resolve the details of the transient flow around the trailing edge of the fan, we use meshes of spatially varying size along the width of the cantilever: 0.1 mm in the internal regions (7 spheres of radius 2.5 mm), 0.2 mm in the intermediate regions (3 spheres of radius 5 mm), 0.3 mm on the wall, and 1 mm in the rest of the domain (figure 6.4). Mesh independence of the numerical simulations is confirmed by halving the mesh size from the above values in a representative case and observing less than 5% change in the velocity profile downstream the fan. The outer walls of the simulation's domain are specified as open boundaries with zero relative pressure to allow the fluid motion in both directions normal to the walls.

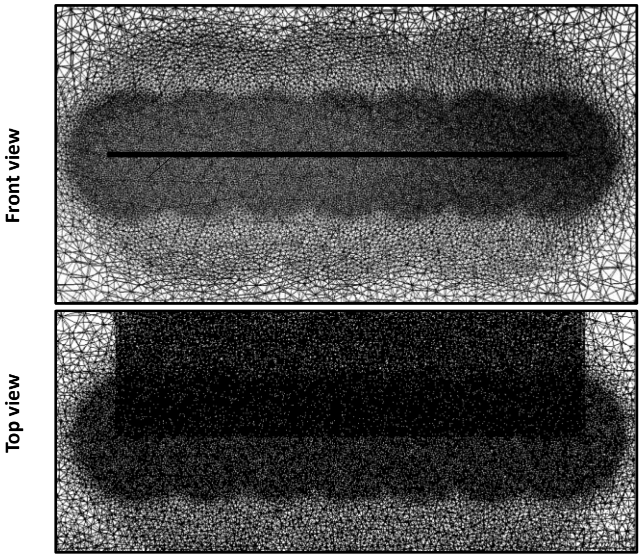

Figure 6.4 The varying mesh size around the oscillating blade of the fan in the simulation domain.

6.4 Results and discussions

6.4.1 Channel flow experiments

Previous study by Chang *et al.* [128] compared the measured Nusselt numbers of the scale-roughened walls to the Nusselt number associated with fully developed flows in circular pipes, i.e. constant value of 3.66. However, it must be considered that their experiments were done in a well-developing flow (i.e. very close to the entrance) inside a rectangular channel in which the Nusselt number for the flat surface could be above 3.66. Therefore, it is important to perform a fair comparison between flat and scaled surfaces in similar conditions to reveal the real thermal enhancement. Table 6.1 summarizes the different channel flow conditions used to compare the surfaces.

Table 6.1 Channel flow conditions

Re_c	**$\bar{U}_c$ (m/s)**
1000	0.9
1500	1.3
2000	1.7
2500	2.2
2750	2.4

Figure 6.5 shows the average channel Nusselt number Nu_c for the tested surfaces with different feature heights e as a function of the channel Reynolds number Re_c. The extracted results from [128] (e = 1 mm) are also shown in the same figure. For all the feature heights tested in this study, the heat transfer augmentation increases with Re_c. Figure 6.5 also suggests that the heat transfer enhancement from the scaled surfaces has a direct relationship with the height of the features. The percent Nusselt enhancement at different feature heights for $Re_c = 2750$ is shown in the inset of figure 6.5, where we observe a maximum 60% enhancement in the Nusselt numbers of the scaled surfaces in our experiments with an almost linear trend, in agreement with the results reported in [135]. Furthermore, changing the direction of the flow does not seem to significantly affect the average Nusselt numbers, with forward flows being slightly better.

We note that the results from [128] are slightly higher due to the differences in their experimental setup. More specifically, they used heated surfaces on both the top and bottom of the test section, which increases the average air temperature at each cross-section and eventually results in slightly higher convective heat transfer coefficient.

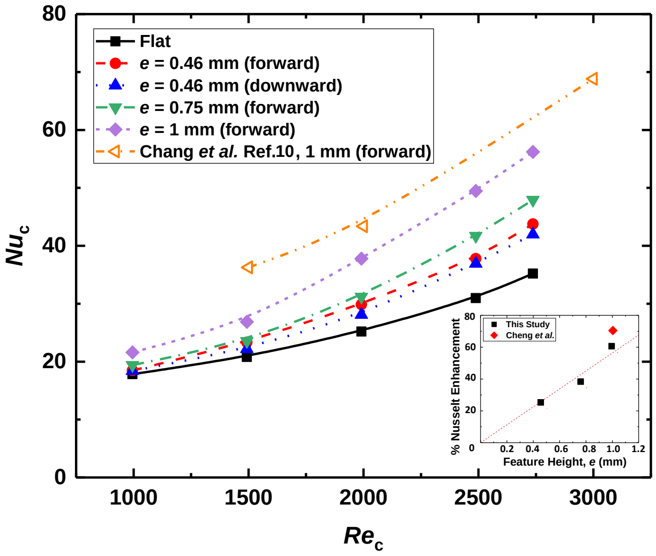

Figure 6.5 Average channel Nusselt number vs. the channel Reynolds number. The inset represents the % Nusselt enhancement at Re_c = 2750 as a function of feature height of the surface. The red dashed line serves as a guide to the eye.

The heat transfer enhancement on the wall's surface is usually accompanied with the pressure drop increase in the test section. Figure 6.6 shows the measured pressure drops in the test section as a function of the Re_c. The uncertainty in the pressure drop measurements is 0.3 Pa. The pressure drop along the test section does not vary significantly in the range of studied Reynolds numbers. This pressure drop increase is not as significant as the resulted heat transfer augmentation. For instance, for e = 1mm and Re_c = 2750, the Nusselt number increase relative to the flat surface is ~ 60%, while the pressure drop increase is ~14%. The measured pressure drops in figure 6.6 agree with the reported results in [135], both in the trend and order of magnitude, however, we avoid a direct comparison as their numerical simulations were conducted in the turbulent regime.

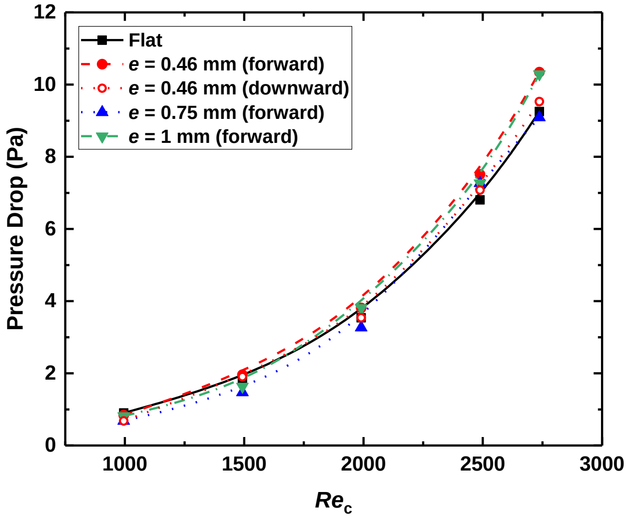

Figure 6.6 Pressure drop in the test section vs. the channel Reynolds number.

6.4.2 Piezoelectric fan experiment

Figures 6.7 – 6.9 show the average velocity field resulting from the piezoelectric fan's induced jet upon impinging a flat surface located 5 mm downstream the fan. The velocity field is averaged over 20 cycles of oscillations. Table 6.2 lists the flow conditions for all the piezoelectric fan configurations used in this study. For a fixed vibration amplitude, the velocity profile on the heated surface is not uniform. It consists of a stagnation region in the middle evolving from an almost linear shape at lower amplitudes to a circle at high amplitudes. This stagnation region is followed by two maxima in the direction of the oscillations. After this point, the velocity gradually decreases. Increasing the amplitude of the oscillations results in an increase in both velocity magnitude and the effective area of the flow. For instance, at Re_p = 120 (figure 6.9), the induced jet of the fan shrinks to almost half its initial size due to the dominance of viscosity. This effect is less pronounced at high Re_p as shown in figures 6.8 and 6.9.

Table 6.2 Flow conditions of piezoelectric fans

A_p (mm)	f_p (Hz)	P_{fan} (mW)	U_{max} (m/s)	$\bar{U}_p$ (m/s)	Re_p
2	130	12.1	1.3	0.36	120
2.5	130	25.9	1.5	0.50	167
3	130	44.9	2	0.75	250
3.75	130	62.5	2.2	1.10	367
4	130	116.6	2.47	1.38	459
4.5	130	184.1	2.7	1.50	500
5.5	130	370.0	3	2.00	667
7	130	723.7	3.7	2.40	800
7.75	130	1210.5	4.16	2.78	927

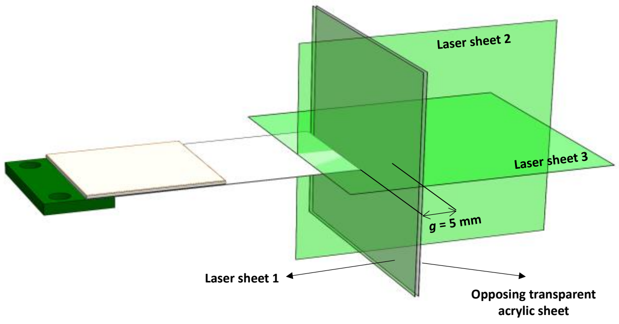

Figure 6.7 Schematic of the orientation of the illuminating laser sheets relative to the opposing surface. The distance between laser sheet 1 and the opposing surface in 0.5±0.1 mm.

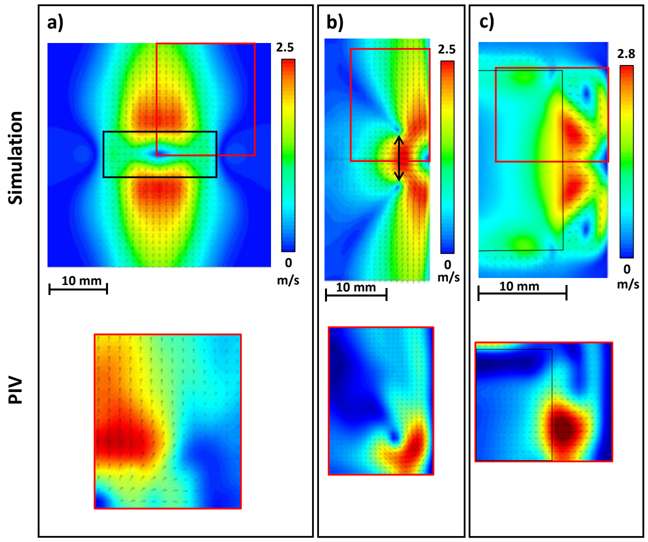

Figure 6.8 Numerical and experimental visualization of the jet-wall interaction at a) laser sheet 1 b) laser sheet 2 c) laser sheet 3 for Re_p = 459. The red and black rectangles indicate the PIV visualization domain and the piezoelectric fan vibration envelope, respectively.

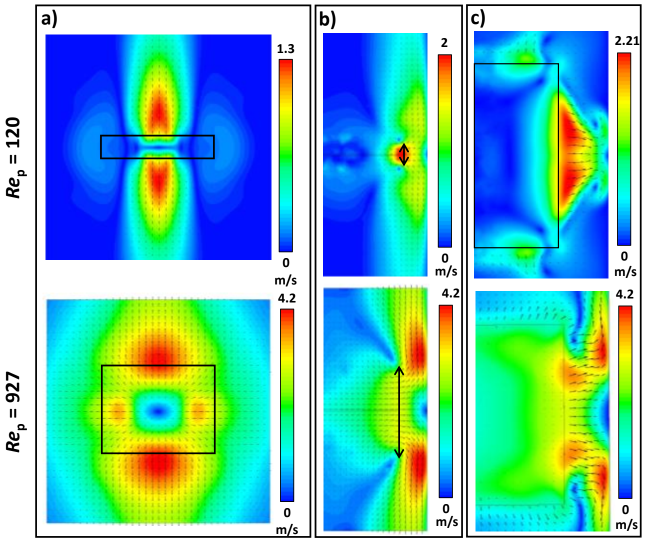

Figure 6.9 Numerical visualization of the jet-wall interaction at a) laser sheet 1 b) laser sheet 2 c) laser sheet 3 for Re_p = 120 and 927. The scale of the images is the same as in figure 6.8. The black rectangles indicate the piezoelectric fan vibration envelope.

Piezoelectric fans' average Nusselt numbers Nu_p on flat and scaled surfaces are shown in figure 6.10 as a function of the fans' Reynolds number Re_p. At low Re_p (Re_p<367), we observe negligible heat transfer augmentation relative to the flat surface due to low average velocities and small effective area of the flow. Increasing the Re_p above this point will result in noticeable heat transfer augmentation. The relative heat transfer enhancement at the highest Re_p tested in this study is 14.3%.

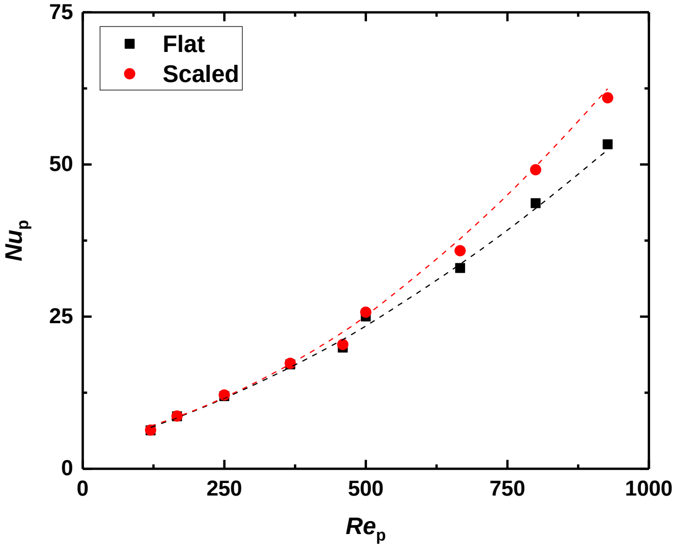

Figure 6.10 Average Nusselt numbers on the tested surfaces as a function of the piezoelectric fan's Reynolds number for *e* = 1 mm.

Figure 6.11 shows the normalized convective heat transfer coefficient h_{fan}/h_{NC} as a function of the power consumption of the fans. The natural convection heat transfer coefficient h_{NC} is measured to be ~17.6 W/m^2 K while the fan is off, consistent with previously reported values for similar test setups [76]. This figure shows the amount of heat transfer enhancement resulting from the piezoelectric fans with and without the scales surfaces.

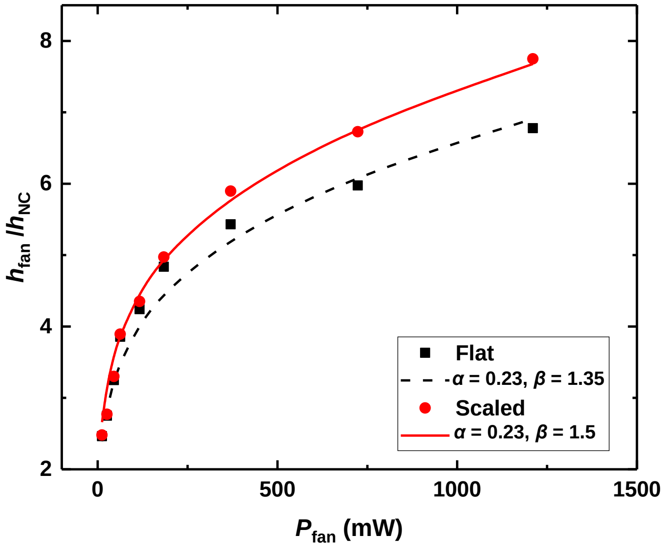

Figure 6.11 Normalized convective heat transfer coefficient vs. fan power consumption for *e* = 1 mm.

The data points shown in figure 6.11 can be fitted using empirical correlations of the form

$$\frac{h_{\mathrm{fan}}}{h_{\mathrm{NC}}} = \beta (P_{\mathrm{fan}})^{\alpha} \tag{6.6}$$

where the exponent α represents the thermo-hydraulic interactions between the fan's blade and the surrounding air. Previous studies [76] suggest a nearly constant value of α for different blade geometries at a fixed distance from the heat source. The coefficient β includes the effect of the surface patterns on the heat transfer augmentation. The fitted curves along with the resulted values of α and β are shown in figure 6.11 for both flat and scaled surfaces.

Figure 6.12 depicts the percent Nusselt enhancement due to the scaled surfaces in a wide range of Reynolds numbers. The horizontal axis in this figure represents Re_{p} for piezoelectric fans and Re_{c} for channel setup. The results extracted from [135] are also shown for turbulent flows. The heat transfer augmentation associated with the laminar flow regimes ($Re < 2500$) ranges from 0 to 60%. As the flow transitions to turbulent regime ($3000 < Re < 4000$), the Nusselt enhancement increases abruptly due to the generation of secondary vortical flows [135]. After a modest peak at $Re \sim 6000$, the Nusselt enhancement decreases with increasing Reynolds numbers.

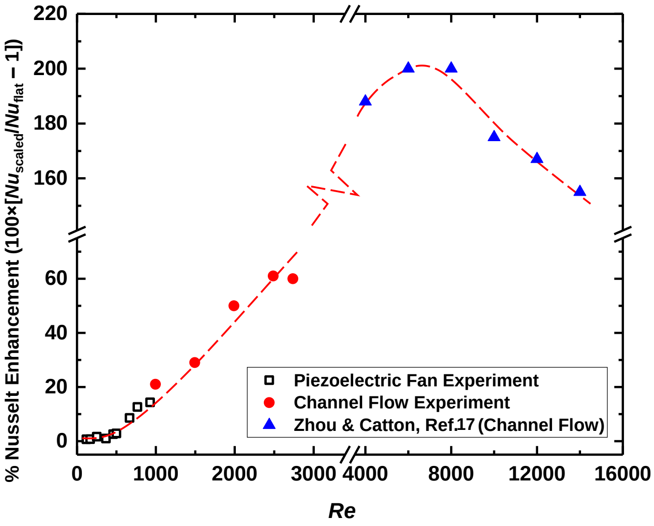

Figure 6.12 Percent Nusselt enhancement in scaled surfaces (e = 1 mm) relative to a flat surface. The red dashed line is a guide to the eye and is not meant to serve as a curve fit.

The power efficiency of the scale-roughened surfaces in channel flows is quantified by performance factor, η, defined as

$$\eta = \frac{Nu}{f^{1/3}} \tag{6.7}$$

where f is the friction factor obtained from the pressure drop in the test section using

$$f = \frac{\Delta P}{0.5\rho \bar{U}_c{}^2}\frac{D_{h,c}}{4L} \tag{6.8}$$

The performance factor indicates the amount of Nusselt number enhancement resulting from the surface per pump power increase. The exponent 1/3 satisfies the constant pump power requirement [140].

Unlike the channel test, the power efficiency of the piezoelectric fans' flow on the tested surfaces cannot be directly related to the pressure drop. Furthermore, direct measurement of the pressure drops in the unconfined domain that the piezoelectric fans are operating poses different challenges. Therefore, to analyze the power efficiency of the two surfaces in this configuration, we directly measure the power consumption of the fans using the method described in a previous work [76]. The power efficiency of the piezoelectric fans is then quantified as

$$\boldsymbol{\eta} = \frac{\boldsymbol{Nu}}{\boldsymbol{P}_{\mathbf{fan}}} \tag{6.9}$$

Figure 6.13 shows the percent power efficiency enhancement resulting from the scaled surfaces. In contrast with the previous graph, the high Nusselt enhancement in the turbulent regime is moderated by the accompaniment of large pressure drops in this regime, forming an almost continuous curve in the range of investigated Reynolds numbers. This figure further indicates that a maximum of ~50% efficiency enhancement can be achieved using scaled surfaces. This maximum occurs in the transition regime, where the occurrence of secondary flows assists the heat transfer from the surface with minimum power consumption increase.

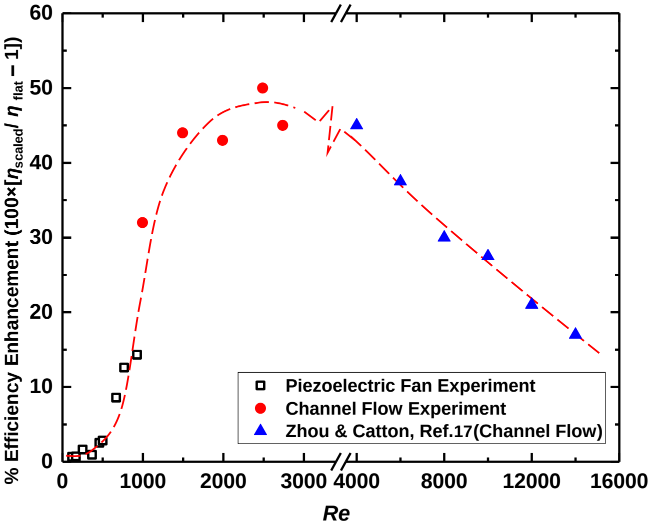

Figure 6.13 Percent efficiency enhancement in scaled surfaces (e = 1 mm) relative to a flat surface. The red dashed line is a guide to the eye and is not meant to serve as a curve fit.

6.5 Summary

In the present study, we measured and compared the convective heat transfer performance of scaled and flat surfaces in low Reynolds flows. In the presence of a uniform channel flow, the heat transfer enhancement exhibited a direct correlation with the channel Reynolds number and the surface feature heights within the studied range ($1000 < Re_c < 2750$, $0.46 \text{ mm} < e < 1 \text{ mm}$). This trend agrees with the previous observations reported elsewhere in the literature. A maximum heat transfer augmentation of 60% relative to the flat surface was observed for $Re_c = 2750$ and $e = 1$ mm. Furthermore, no appreciable pressure drop was introduced in the test section by increasing the surface roughness.

Visualization of the piezoelectric fan's flow interaction with an opposing wall revealed that a nonuniform symmetric velocity field is induced parallel to the wall with an average velocity comparable to the uniform velocity in the test channel. This nonuniform flow resulted in 14% enhancement at the highest tested fan's Reynolds number ($Re_p = 927$).

A quantitative representation of the power efficiency of the different surfaces was assessed by defining a performance factor, η, which indicates the Nusselt number enhancement per power consumption increase. With this standard, a maximum of ~50% efficiency enhancement was achieved using scaled surfaces. This maximum occurred in the transition regime where the formation of secondary flows with low power costs assisted the heat transfer from the surface.

The results presented in this study demonstrate the application of scaled surfaces in low Reynolds thermal components, such as piezoelectric fans, motivate more systematic design and optimization of such surfaces.

Chapter 7. Summary and future work recommendations

7.1 Summary

In the present study, we provided a comprehensive investigation of the power consumption mechanisms, complex fluid dynamics, and heat transfer performance of piezoelectric fans in order to facilitate their optimized design for a variety of applications. We began by performing a combined experimental and modeling study to help elucidate different power dissipation mechanisms in piezoelectric fans and obtain an optimal operating condition for maximum power efficiency. Our data and model analyses showed that the mechanical hysteresis loss and, to a lesser extent, the dielectric loss are dominant sources of parasitic power dissipation in the actuators. We also showed that in a typical piezoelectric fan, 30 to 80% of the total consumed power stems from the presence of the plate and aerodynamic interactions.

We next investigated the vortex regimes present in the wake of a harmonically oscillating cantilever plate in a quiescent, incompressible, viscous fluid and analyzed their effect on the mean fluid jet downstream. Based on the qualitative features of the vortex shedding from the trailing edge, we identified three distinct vortex regimes in the wake, namely non-propagating, intermediate and propagating. We further demonstrated that these regimes can be presented in a regime map with lines of constant *Re* as transition lines between adjacent regimes. Our qualitative and quantitative analysis of the flow on the normal mid-plane revealed that these vortex regimes significantly affect the mean fluid jet downstream of the thin plate.

In the next step, we conducted a combined experimental and numerical study on the three-dimensional geometry of the induced mean jet downstream of a pitching cantilever plate and correlated it with the transient vortex behavior in the wake. Our results showed that the time-averaged velocity field forms two distinct regions in the wake identified by their shrinking or expanding nature. We systematically studied the effect of several geometric and vibrational parameters on the shape of the induced jet, such as normalized amplitude, plate aspect ratio, and Reynolds number, and provided scaling laws to predict the shape of the induced jet in a variety of operating conditions.

Finally, we investigated the effect of plate geometry and surface roughness on the power efficiency of the piezoelectric fans. Our results show that using artificially patterned surfaces as the cooling target, such as a scale-roughened surface, can increase the Nusselt numbers in otherwise similar conditions by ~20%. We also demonstrated that plates with concave-tapered geometry provide the most thermal enhancement per unit power, and hence the most efficiency, for applications with a prescribed amplitude and frequency. For most of the piezoelectric fans' applications, however, power consumption at a prescribed Nusselt number is of interest. Our results show that different geometries exhibit nearly equal efficiencies for these applications, with convex plates requiring the lowest amplitude.

7.2 Future work recommendations

Although this study endeavors to address some of the common challenges in using piezoelectric fans as viable low power thermal solutions for consumer electronics and wearable devices, there remain areas that require further research and development effort should piezoelectric fans be chosen for thermal management applications. The following recommendations and guidelines are based on the author's five-year experience in working with these fans:

7.2.1 Using flexible polymer piezoelectric actuators

Current commercial piezoelectric fans have two important intrinsic issues that prevent their wide-spread application: fragility and long form factor. The former issue arises from the use of thin and delicate piezoceramics in the actuator section, while the latter is due to the separation of the rigid actuator and flexible vibrating plate, which makes the overall length of the device excessively long. Recently, novel polymer-based piezoelectric materials, such as PVDF [141]–[144], have been introduced that exhibit superior flexibility and durability compared to piezoelectric ceramics, such as PZT ceramic. These piezoelectric materials can be used to resolve the reliability issues associated with the current piezoelectric fans. In addition, the flexibility of these materials allows combining the actuator and plate into a single cantilever, and as a result, reducing the overall length of the fans. To the best of our knowledge, no fundamental research has been done so far to investigate the feasibility of using these materials as high-amplitude, high-frequency oscillators for cooling applications.

7.2.2 A control algorithm for rectifying the resonance frequency shifts

Another important issue associated with piezoelectric fans, and multi-component vibrating mechanical systems in general, is the resonance frequency shift due to the accumulation of dirt on the oscillating part, and chemical and physical changes in the adhesive material with time and temperature. It was frequently observed that the resonance frequency of the fans changes within ± 5 Hz from its initial value over long periods of operation, especially in cases with rigid plates (metallic plates). This issue, however, can be solved to a great extent by generating a control algorithm that runs a sweep over the acceptable range of frequency within specific time intervals and chooses the frequency that results in the maximum power consumption (power consumption peaks at the resonance frequency of the plate).

7.2.3 Effect of plate material and geometry on noise generation

Piezoelectric fans that are required to operate at high frequencies (f >150 Hz) usually generate audible and disturbing noise. The noise issue can even occur at lower frequencies if the plate creates higher frequency noise due to its in-plane deflections (usually for metallic plates). In our experience, several factors play role in mitigating the noise issue, including the plate material, plate geometry, plate surface topology (smoothness), and the condition at the base where the plate connects to the actuator. To the best of our knowledge, no comprehensive study has been performed to investigate the physics of the noise in piezoelectric fans and methods to reduce the noise by changing the above-mentioned factors.

Chapter 8. References

[1] M. Arik, J. Petroski, A. Bar-Cohen, and M. Demiroglu, “Energy Efficiency of Low Form Factor Cooling Devices,” *ASME Int. Mech. Eng. Congr. Expo.*, vol. Volume 8: Heat Transfer, Fluid Flows, and Thermal Systems, Parts A and B, pp. 1347–1354, Jan. 2007, doi: 10.1115/IMECE2007-41275.

[2] M. Kimber, K. Suzuki, N. Kitsunai, K. Seki, and S. V. Garimella, “Pressure and Flow Rate Performance of Piezoelectric Fans,” *IEEE Trans. Compon. Packag. Technol.*, vol. 32, no. 4, pp. 766–775, Dec. 2009, doi: 10.1109/TCAPT.2008.2012169.

[3] T. Açikalin and S. V. Garimella, “Analysis and Prediction of the Thermal Performance of Piezoelectrically Actuated Fans,” *Heat Transf. Eng.*, vol. 30, no. 6, pp. 487–498, May 2009, doi: 10.1080/01457630802529115.

[4] T. AÇIKALIN, S. M. WAIT, S. V. GARIMELLA, and A. RAMAN, “Experimental Investigation of the Thermal Performance of Piezoelectric Fans,” *Heat Transf. Eng.*, vol. 25, no. 1, pp. 4–14, Jan. 2004, doi: 10.1080/01457630490248223.

[5] C.-N. Lin, “Analysis of three-dimensional heat and fluid flow induced by piezoelectric fan,” *Int. J. Heat Mass Transf.*, vol. 55, no. 11–12, pp. 3043–3053, May 2012, doi: 10.1016/j.ijheatmasstransfer.2012.02.017.

[6] T. Lei, Z. Jing-zhou, and T. Xiao-ming, “Numerical investigation of convective heat transfer on a vertical surface due to resonating cantilever beam,” *Int. J. Therm. Sci.*, vol. 80, pp. 93–107, Jun. 2014, doi: 10.1016/j.ijthermalsci.2014.02.004.

[7] S. F. Sufian, M. Z. Abdullah, M. K. Abdullah, and J. J. Mohamed, “Effect of Side and Tip Gaps of a Piezoelectric Fan on Microelectronic Cooling,” *IEEE Trans. Compon. Packag.*

Manuf. Technol., vol. 3, no. 9, pp. 1545–1553, Sep. 2013, doi: 10.1109/TCPMT.2013.2251759.

[8] P. Burmann, A. Raman, and S. V. Garimella, "Dynamics and topology optimization of piezoelectric fans," *IEEE Trans. Compon. Packag. Technol.*, vol. 25, no. 4, pp. 592–600, Dec. 2002, doi: 10.1109/TCAPT.2003.809111.

[9] T. Wu, P. I. Ro, A. I. Kingon, and J. F. Mulling, "Piezoelectric resonating structures for microelectronic cooling," *Smart Mater. Struct.*, vol. 12, no. 2, p. 181, 2003, doi: 10.1088/0964-1726/12/2/304.

[10] T. Açıkalın, S. V. Garimella, A. Raman, and J. Petroski, "Characterization and optimization of the thermal performance of miniature piezoelectric fans," *Int. J. Heat Fluid Flow*, vol. 28, no. 4, pp. 806–820, Aug. 2007, doi: 10.1016/j.ijheatfluidflow.2006.10.003.

[11] J. Cho, T. Lim, and B. S. Kim, "Measurements and predictions of the air distribution systems in high compute density (Internet) data centers," *Energy Build.*, vol. 41, no. 10, pp. 1107–1115, Oct. 2009, doi: 10.1016/j.enbuild.2009.05.017.

[12] J. H. Yoo, J. I. Hong, and W. Cao, "Piezoelectric ceramic bimorph coupled to thin metal plate as cooling fan for electronic devices," *Sens. Actuators Phys.*, vol. 79, no. 1, pp. 8–12, Jan. 2000, doi: 10.1016/S0924-4247(99)00249-6.

[13] C.-H. Huang, Y.-F. Chen, and H. Ay, "An inverse problem in determining the optimal position for piezoelectric fan with experimental verification," *Int. J. Heat Mass Transf.*, vol. 55, no. 19–20, pp. 5289–5301, Sep. 2012, doi: 10.1016/j.ijheatmasstransfer.2012.05.037.

[14] C.-H. Huang and G.-Y. Fan, "Determination of relative positions and phase angle of dual piezoelectric fans for maximum heat dissipation of fin surface," *Int. J. Heat Mass Transf.*, vol. 92, pp. 523–538, Jan. 2016, doi: 10.1016/j.ijheatmasstransfer.2015.09.006.

[15] J. Petroski, M. Arik, and M. Gursoy, “Optimization of Piezoelectric Oscillating Fan-Cooled Heat Sinks for Electronics Cooling,” *IEEE Trans. Compon. Packag. Technol.*, vol. 33, no. 1, pp. 25–31, Mar. 2010, doi: 10.1109/TCAPT.2009.2023859.

[16] C. Liang, F. P. Sun, and C. A. Rogers, “An Impedance Method for Dynamic Analysis of Active Material Systems,” *J. Vib. Acoust.*, vol. 116, no. 1, pp. 120–128, Jan. 1994, doi: 10.1115/1.2930387.

[17] Y. S. Cho, Y. E. Pak, C. S. Han, and S. K. Ha, “Five-port equivalent electric circuit of piezoelectric bimorph beam,” *Sens. Actuators Phys.*, vol. 84, no. 1–2, pp. 140–148, Aug. 2000, doi: 10.1016/S0924-4247(99)00231-9.

[18] W.-J. Sheu, R.-T. Huang, and C.-C. Wang, “Influence of bonding glues on the vibration of piezoelectric fans,” *Sens. Actuators Phys.*, vol. 148, no. 1, pp. 115–121, Nov. 2008, doi: 10.1016/j.sna.2008.06.028.

[19] S. M. Wait, S. Basak, S. V. Garimella, and A. Raman, “Piezoelectric Fans Using Higher Flexural Modes for Electronics Cooling Applications,” *IEEE Trans. Compon. Packag. Technol.*, vol. 30, no. 1, pp. 119–128, Mar. 2007, doi: 10.1109/TCAPT.2007.892084.

[20] G. H. Koopmann, “The vortex wakes of vibrating cylinders at low Reynolds numbers,” *J. Fluid Mech.*, vol. 28, no. 3, pp. 501–512, May 1967, doi: 10.1017/S0022112067002253.

[21] O. M. Griffin and S. E. Ramberg, “The vortex-street wakes of vibrating cylinders,” *J. Fluid Mech.*, vol. 66, no. 3, pp. 553–576, Nov. 1974, doi: 10.1017/S002211207400036X.

[22] C. H. K. Williamson and A. Roshko, “Vortex formation in the wake of an oscillating cylinder,” *J. Fluids Struct.*, vol. 2, no. 4, pp. 355–381, Jul. 1988, doi: 10.1016/S0889-9746(88)90058-8.

[23] M. M. Koochesfahani, “Vortical patterns in the wake of an oscillating airfoil,” *AIAA J.*, vol. 27, no. 9, pp. 1200–1205, 1989, doi: 10.2514/3.10246.

[24] D. G. Bohl and M. M. Koochesfahani, “MTV measurements of the vortical field in the wake of an airfoil oscillating at high reduced frequency,” *J. Fluid Mech.*, vol. 620, pp. 63–88, Feb. 2009, doi: 10.1017/S0022112008004734.

[25] T. Schnipper, A. Andersen, and T. Bohr, “Vortex wakes of a flapping foil,” *J. Fluid Mech.*, vol. 633, pp. 411–423, Aug. 2009, doi: 10.1017/S0022112009007964.

[26] J. H. J. Buchholz and A. J. Smits, “The wake structure and thrust performance of a rigid low-aspect-ratio pitching panel,” *J. Fluid Mech.*, vol. 603, pp. 331–365, May 2008, doi: 10.1017/S0022112008000906.

[27] J. H. J. Buchholz and A. J. Smits, “On the evolution of the wake structure produced by a low-aspect-ratio pitching panel,” *J. Fluid Mech.*, vol. 546, pp. 433–443, Jan. 2006, doi: 10.1017/S0022112005006865.

[28] J. H. J. Buchholz, M. A. Green, and A. J. Smits, “Scaling the circulation shed by a pitching panel,” *J. Fluid Mech.*, vol. 688, pp. 591–601, Dec. 2011, doi: 10.1017/jfm.2011.408.

[29] J. C. Lai and M. F. Platzer, “Characteristics of a plunging airfoil at zero freestream velocity,” *AIAA J.*, vol. 39, no. 3, pp. 531–534, 2001.

[30] S. Heathcote, D. Martin, and I. Gursul, “Flexible flapping airfoil propulsion at zero freestream velocity,” *AIAA J.*, vol. 42, no. 11, 2004.

[31] Y.-H. Kim, S. T. Wereley, and C.-H. Chun, “Phase-resolved flow field produced by a vibrating cantilever plate between two endplates,” *Phys. Fluids 1994-Present*, vol. 16, no. 1, pp. 145–162, Jan. 2004, doi: 10.1063/1.1630796.

[32] Y.-H. Kim, C. Cierpka, and S. T. Wereley, "Flow field around a vibrating cantilever: coherent structure eduction by continuous wavelet transform and proper orthogonal decomposition," *J. Fluid Mech.*, vol. 669, pp. 584–606, Feb. 2011, doi: 10.1017/S0022112010005318.

[33] M. Choi, C. Cierpka, and Y.-H. Kim, "Vortex formation by a vibrating cantilever," *J. Fluids Struct.*, vol. 31, no. Supplement C, pp. 67–78, May 2012, doi: 10.1016/j.jfluidstructs.2012.03.004.

[34] M. H. Oh, S. H. Park, Y.-H. Kim, and M. Choi, "3D flow structure around a piezoelectrically oscillating flat plate," *Eur. J. Mech. - BFluids*, vol. 67, pp. 249–258, Jan. 2018, doi: 10.1016/j.euromechflu.2017.09.002.

[35] A. Eastman, J. Kiefer, and M. Kimber, "Thrust measurements and flow field analysis of a piezoelectrically actuated oscillating cantilever," *Exp. Fluids*, vol. 53, no. 5, pp. 1533–1543, Sep. 2012, doi: 10.1007/s00348-012-1373-6.

[36] B. Shrestha, S. N. Ahsan, and M. Aureli, "Experimental study of oscillating plates in viscous fluids: Qualitative and quantitative analysis of the flow physics and hydrodynamic forces," *Phys. Fluids*, vol. 30, no. 1, p. 013102, Jan. 2018, doi: 10.1063/1.5001330.

[37] J. H. J. Buchholz and A. J. Smits, "Wake of a low aspect ratio pitching plate," *Phys. Fluids*, vol. 17, no. 9, p. 091102, Aug. 2005, doi: 10.1063/1.1942512.

[38] J. H. J. Buchholz, R. P. Clark, and A. J. Smits, "Thrust performance of unsteady propulsors using a novel measurement system, and corresponding wake patterns," *Exp. Fluids*, vol. 45, no. 3, pp. 461–472, Sep. 2008, doi: 10.1007/s00348-008-0489-1.

[39] J. H. J. Buchholz, "The flowfield and performance of a low aspect ratio unsteady propulsor," *PhD Thesis*, 2006, [Online]. Available: http://adsabs.harvard.edu/abs/2006PhDT........79B.

[40] M. A. Green and A. J. Smits, “Effects of three-dimensionality on thrust production by a pitching panel,” *J. Fluid Mech.*, vol. 615, pp. 211–220, Nov. 2008, doi: 10.1017/S0022112008003583.

[41] M. A. Green, C. W. Rowley, and A. J. Smits, “The unsteady three-dimensional wake produced by a trapezoidal pitching panel,” *J. Fluid Mech.*, vol. 685, pp. 117–145, Oct. 2011, doi: 10.1017/jfm.2011.286.

[42] J. T. King and M. A. Green, “Experimental Study of the Three-Dimensional Wakes Produced by Trapezoidal Panels with Varying Trailing Edge Geometry and Pitching Amplitude,” in *AIAA Scitech 2019 Forum*, 2019, p. 1380.

[43] K. Taira and T. Colonius, “Three-dimensional flows around low-aspect-ratio flat-plate wings at low Reynolds numbers,” *J. Fluid Mech.*, vol. 623, pp. 187–207, Mar. 2009, doi: 10.1017/S0022112008005314.

[44] A. Agarwal, K. P. Nolan, J. Stafford, and N. Jeffers, “Visualization of three-dimensional structures shed by an oscillating beam,” *J. Fluids Struct.*, vol. 70, pp. 450–463, Apr. 2017, doi: 10.1016/j.jfluidstructs.2017.02.013.

[45] M. H. Oh, J. Seo, Y.-H. Kim, and M. Choi, “Endwall effects on 3D flow around a piezoelectric fan,” *Eur. J. Mech. - BFluids*, vol. 75, pp. 339–351, May 2019, doi: 10.1016/j.euromechflu.2018.10.021.

[46] W. E. Baker, W. E. Woolam, and D. Young, “Air and internal damping of thin cantilever beams,” *Int. J. Mech. Sci.*, vol. 9, no. 11, pp. 743–766, Nov. 1967, doi: 10.1016/0020-7403(67)90032-X.

[47] “IEEE Standard on Piezoelectricity,” *ANSIIEEE Std 176-1987*, p. 0_1-, 1988, doi: 10.1109/IEEESTD.1988.79638.

[48] M. W. Hooker, “Properties of PZT-Based Piezoelectric Ceramics Between -150 and 250 C,” Sep. 1998. Accessed: Jan. 19, 2017. [Online]. Available: https://ntrs.nasa.gov/search.jsp?R=19980236888.

[49] A. I. Kingon, P. J. Terblanche, and J. B. Clark, “Variability of the high field properties of PZT-4 and PZT-8 type piezoelectric ceramics,” *Ferroelectrics*, vol. 37, no. 1, pp. 635–638, Oct. 1981, doi: 10.1080/00150198108223504.

[50] T. S. Low and W. Guo, “Modeling of a three-layer piezoelectric bimorph beam with hysteresis,” *J. Microelectromechanical Syst.*, vol. 4, no. 4, pp. 230–237, Dec. 1995, doi: 10.1109/84.475550.

[51] M. Rakotondrabe, Y. Haddab, and P. Lutz, “Quadrilateral Modelling and Robust Control of a Nonlinear Piezoelectric Cantilever,” *IEEE Trans. Control Syst. Technol.*, vol. 17, no. 3, pp. 528–539, May 2009, doi: 10.1109/TCST.2008.2001151.

[52] W. T. Ang, F. A. Garmon, P. K. Khosla, and C. N. Riviere, “Modeling rate-dependent hysteresis in piezoelectric actuators,” in *Proceedings 2003 IEEE/RSJ International Conference on Intelligent Robots and Systems (IROS 2003) (Cat. No.03CH37453)*, Oct. 2003, vol. 2, pp. 1975–1980 vol.2, doi: 10.1109/IROS.2003.1248937.

[53] G. Bertotti and I. D. Mayergoyz, *The Science of Hysteresis: Hysteresis in materials*. Gulf Professional Publishing, 2006.

[54] D. Whitley, “A genetic algorithm tutorial,” *Stat. Comput.*, vol. 4, no. 2, pp. 65–85, Jun. 1994, doi: 10.1007/BF00175354.

[55] S. Chonan, Z. Jiang, and T. Yamamoto, “Nonlinear Hysteresis Compensation of Piezoelectric Ceramic Actuators,” *J. Intell. Mater. Syst. Struct.*, vol. 7, no. 2, pp. 150–156, Mar. 1996, doi: 10.1177/1045389X9600700205.

[56] A. J. Fleming and S. O. R. Moheimani, “A grounded-load charge amplifier for reducing hysteresis in piezoelectric tube scanners,” *Rev. Sci. Instrum.*, vol. 76, no. 7, p. 073707, Jun. 2005, doi: 10.1063/1.1938952.

[57] J. Minase, T.-F. Lu, B. Cazzolato, and S. Grainger, “A review, supported by experimental results, of voltage, charge and capacitor insertion method for driving piezoelectric actuators,” *Precis. Eng.*, vol. 34, no. 4, pp. 692–700, Oct. 2010, doi: 10.1016/j.precisioneng.2010.03.006.

[58] R. A. Bidkar, M. Kimber, A. Raman, A. K. Bajaj, and S. V. Garimella, “Nonlinear aerodynamic damping of sharp-edged flexible beams oscillating at low Keulegan–Carpenter numbers,” *J. Fluid Mech.*, vol. 634, pp. 269–289, 2009.

[59] M. Toda, “Theory of air flow generation by a resonant type PVF2 bimorph cantilever vibrator,” *Ferroelectrics*, vol. 22, no. 1, pp. 911–918, Jan. 1978, doi: 10.1080/00150197908239445.

[60] K. Yao and K. Uchino, “Analysis on a composite cantilever beam coupling a piezoelectric bimorph to an elastic blade,” *Sens. Actuators Phys.*, vol. 89, no. 3, pp. 215–221, Apr. 2001, doi: 10.1016/S0924-4247(00)00552-5.

[61] K. Jambunathan, E. Lai, M. A. Moss, and B. L. Button, “A review of heat transfer data for single circular jet impingement,” *Int. J. Heat Fluid Flow*, vol. 13, no. 2, pp. 106–115, 1992.

[62] J. C. AKFIRAT, “Heat transfer characteristics of impinging two-dimensional air jets,” 1966, Accessed: Mar. 07, 2017. [Online]. Available: https://heattransfer.asmedigitalcollection.asme.org/pdfaccess.ashx?resourceid=4514409&pdfsource=13.

[63] A. Hales and X. Jiang, “A review of piezoelectric fans for low energy cooling of power electronics,” *Appl. Energy*, vol. 215, pp. 321–337, Apr. 2018, doi: 10.1016/j.apenergy.2018.02.014.

[64] I. Sauciuc *et al.*, “Key challenges for the piezo technology with applications to low form factor thermal solutions,” in *Thermal and Thermomechanical Proceedings 10th Intersociety Conference on Phenomena in Electronics Systems, 2006. ITHERM 2006.*, May 2006, p. 5 pp. – 785, doi: 10.1109/ITHERM.2006.1645426.

[65] H.-C. Wang, N. E. Jewell-Larsen, and A. V. Mamishev, “Thermal management of microelectronics with electrostatic fluid accelerators,” *Appl. Therm. Eng.*, vol. 51, no. 1–2, pp. 190–211, Mar. 2013, doi: 10.1016/j.applthermaleng.2012.08.068.

[66] H.-C. Su and H. Y. Xu, “Investigation of a double oscillating-fan cooling device using electromagnetic force,” *Appl. Therm. Eng.*, vol. 103, pp. 553–563, Jun. 2016, doi: 10.1016/j.applthermaleng.2016.04.123.

[67] A. L. C. Fujarra, C. P. Pesce, F. Flemming, and C. H. K. Williamson, “VORTEX-INDUCED VIBRATION OF A FLEXIBLE CANTILEVER,” *J. Fluids Struct.*, vol. 15, no. 3, pp. 651–658, Apr. 2001, doi: 10.1006/jfls.2000.0368.

[68] T. Sarpkaya, “A critical review of the intrinsic nature of vortex-induced vibrations,” *J. Fluids Struct.*, vol. 19, no. 4, pp. 389–447, May 2004, doi: 10.1016/j.jfluidstructs.2004.02.005.

[69] C. H. K. Williamson and R. Govardhan, “A brief review of recent results in vortex-induced vibrations,” *J. Wind Eng. Ind. Aerodyn.*, vol. 96, no. 6, pp. 713–735, Jun. 2008, doi: 10.1016/j.jweia.2007.06.019.

[70] N. Gravish, J. M. Peters, S. A. Combes, and R. J. Wood, "Collective Flow Enhancement by Tandem Flapping Wings," *Phys. Rev. Lett.*, vol. 115, no. 18, p. 188101, Oct. 2015, doi: 10.1103/PhysRevLett.115.188101.

[71] C. Prince, W. Lin, J. Lin, S. D. Peterson, and M. Porfiri, "Temporally-resolved hydrodynamics in the vicinity of a vibrating ionic polymer metal composite," *J. Appl. Phys.*, vol. 107, no. 9, p. 094908, May 2010, doi: 10.1063/1.3410727.

[72] S. D. Peterson, M. Porfiri, and A. Rovardi, "A Particle Image Velocimetry Study of Vibrating Ionic Polymer Metal Composites in Aqueous Environments," *IEEEASME Trans. Mechatron.*, vol. 14, no. 4, pp. 474–483, Aug. 2009, doi: 10.1109/TMECH.2009.2020979.

[73] K. Abdelnour, E. Mancia, S. D. Peterson, and M. Porfiri, "Hydrodynamics of underwater propulsors based on ionic polymer–metal composites: a numerical study," *Smart Mater. Struct.*, vol. 18, no. 8, p. 085006, 2009, doi: 10.1088/0964-1726/18/8/085006.

[74] M. Aureli, C. Pagano, and M. Porfiri, "Nonlinear finite amplitude torsional vibrations of cantilevers in viscous fluids," *J. Appl. Phys.*, vol. 111, no. 12, p. 124915, Jun. 2012, doi: 10.1063/1.4730383.

[75] R. J. Linderman, O. Nilsen, and V. M. Bright, "Electromechanical and fluidic evaluation of the resonant microfan gas pump and aerosol collector," *Sens. Actuators Phys.*, vol. 118, no. 1, pp. 162–170, Jan. 2005, doi: 10.1016/j.sna.2004.08.011.

[76] N. Dehdari Ebrahimi, Y. Wang, and Y. S. Ju, "Mechanisms of power dissipation in piezoelectric fans and their correlation with convective heat transfer performance," *Sens. Actuators Phys.*, vol. 272, pp. 242–252, Apr. 2018, doi: 10.1016/j.sna.2018.01.031.

[77] A. Eastman and M. L. Kimber, “Aerodynamic damping of sidewall bounded oscillating cantilevers,” *J. Fluids Struct.*, vol. 51, pp. 148–160, Nov. 2014, doi: 10.1016/j.jfluidstructs.2014.07.016.

[78] W. Thielicke and E. Stamhuis, “PIVlab – Towards User-friendly, Affordable and Accurate Digital Particle Image Velocimetry in MATLAB,” *J. Open Res. Softw.*, vol. 2, no. 1, Oct. 2014, doi: 10.5334/jors.bl.

[79] W. Thielicke and E. J. Stamhuis, “PIVlab - Time-Resolved Digital Particle Image Velocimetry Tool for MATLAB (version: 1.41).” doi: 10.6084/m9.figshare.1092508.v6.

[80] D. Garcia, “Robust smoothing of gridded data in one and higher dimensions with missing values,” *Comput. Stat. Data Anal.*, vol. 54, no. 4, pp. 1167–1178, Apr. 2010, doi: 10.1016/j.csda.2009.09.020.

[81] W. Thielicke, “The flapping flight of birds: Analysis and application,” University of Groningen, 2014.

[82] “Immersed Boundary Methods,” *Annu. Rev. Fluid Mech.*, vol. 37, no. 1, pp. 239–261, 2005, doi: 10.1146/annurev.fluid.37.061903.175743.

[83] S. N. Ahsan and M. Aureli, “Three-Dimensional Analysis of Shape-Morphing Cantilever Oscillations in Viscous Fluids,” p. V003T22A005, Oct. 2017, doi: 10.1115/DSCC2017-5402.

[84] A. L. Facci and M. Porfiri, “Analysis of three-dimensional effects in oscillating cantilevers immersed in viscous fluids,” *J. Fluids Struct.*, vol. 38, no. Supplement C, pp. 205–222, Apr. 2013, doi: 10.1016/j.jfluidstructs.2012.11.006.

[85] D. G. Crighton, “The Kutta condition in unsteady flow,” *Annu. Rev. Fluid Mech.*, vol. 17, no. 1, pp. 411–445, 1985.

[86] S. J. Lighthill, *Mathematical biofluiddynamics*. SIAM, 1975.

[87] T. Y.-T. Wu, “Swimming of a waving plate,” *J. Fluid Mech.*, vol. 10, no. 3, pp. 321–344, May 1961, doi: 10.1017/S0022112061000949.

[88] N. Dehdari Ebrahimi, Z. Zeng, and Y. S. Ju, “Vortex propagation in air flows generated by piezoelectric fans and their correlation with fan cooling power efficiency,” *Proc. 16th Int. Heat Transf. Conf. IHTC-16 Beijing China*, pp. 3895–3902, 2018.

[89] T. Açıkalın, A. Raman, and S. V. Garimella, “Two-dimensional streaming flows induced by resonating, thin beams,” *J. Acoust. Soc. Am.*, vol. 114, no. 4, pp. 1785–1795, Oct. 2003, doi: 10.1121/1.1610453.

[90] L. Graftieaux, M. Michard, and N. Grosjean, “Combining PIV, POD and vortex identification algorithms for the study of unsteady turbulent swirling flows,” *Meas. Sci. Technol.*, vol. 12, no. 9, p. 1422, 2001, doi: 10.1088/0957-0233/12/9/307.

[91] J.-Z. Wu, H. Ma, and M.-D. Zhou, *Vorticity and Vortex Dynamics*. Springer Science & Business Media, 2007.

[92] M. Nazari, A. Masoudi, P. Jafari, P. Irajizad, V. Kashyap, and H. Ghasemi, “Ultrahigh Evaporative Heat Fluxes in Nanoconfined Geometries,” *Langmuir*, vol. 35, no. 1, pp. 78–85, Jan. 2019, doi: 10.1021/acs.langmuir.8b03463.

[93] P. Jafari *et al.*, “Evaporation Mass Flux: A Predictive Model and Experiments,” *Langmuir*, vol. 34, no. 39, pp. 11676–11684, Oct. 2018, doi: 10.1021/acs.langmuir.8b02289.

[94] L. Cen and A. Erturk, “Bio-inspired aquatic robotics by untethered piezohydroelastic actuation,” *Bioinspir. Biomim.*, vol. 8, no. 1, p. 016006, Jan. 2013, doi: 10.1088/1748-3182/8/1/016006.

[95] M. Asadzade and A. Shamloo, “Design and simulation of a novel bipolar plate based on lung-shaped bio-inspired flow pattern for PEM fuel cell,” *Int. J. Energy Res.*, vol. 41, no. 12, pp. 1730–1739, 2017, doi: 10.1002/er.3741.

[96] M. A. Bidakhvidi, R. Shirzadeh, G. Steenackers, and S. Vanlanduit, “Experimental study of the flow field induced by a resonating piezoelectric flapping wing,” *Exp. Fluids*, vol. 54, no. 11, p. 1619, Oct. 2013, doi: 10.1007/s00348-013-1619-y.

[97] M. J. Lighthill, “Large-amplitude elongated-body theory of fish locomotion | Proceedings of the Royal Society of London. Series B. Biological Sciences,” *Proc. R. Soc. Lond. B Biol. Sci.*, vol. 179, no. 1055, pp. 125–138, 11 1971, doi: https://doi.org/10.1098/rspb.1971.0085.

[98] N. Dehdari Ebrahimi, J. D. Eldredge, and Y. S. Ju, “Wake vortex regimes of a pitching cantilever plate in quiescent air and their correlation with mean flow generation,” *J. Fluids Struct.*, vol. 84, pp. 408–420, Jan. 2019, doi: 10.1016/j.jfluidstructs.2018.11.010.

[99] J. Jeong and F. Hussain, “On the identification of a vortex,” *J. Fluid Mech.*, vol. 285, pp. 69–94, Feb. 1995, doi: 10.1017/S0022112095000462.

[100] R. GODOY-DIANA, C. MARAIS, J.-L. AIDER, and J. E. WESFREID, “A model for the symmetry breaking of the reverse Bénard–von Kármán vortex street produced by a flapping foil,” *J. Fluid Mech.*, vol. 622, pp. 23–32, 2009, doi: 10.1017/S0022112008005727.

[101] S. Y. Shinde and J. H. Arakeri, “Flexibility in flapping foil suppresses meandering of induced jet in absence of free stream,” *J. Fluid Mech.*, vol. 757, pp. 231–250, 2014, doi: 10.1017/jfm.2014.480.

[102] D. J. Cleaver, Z. Wang, and I. Gursul, “Bifurcating flows of plunging aerofoils at high Strouhal numbers,” *J. Fluid Mech.*, vol. 708, pp. 349–376, Oct. 2012, doi: 10.1017/jfm.2012.314.

[103] V. Raspa, S. Ramananarivo, B. Thiria, and R. Godoy-Diana, “Vortex-induced drag and the role of aspect ratio in undulatory swimmers,” *Phys. Fluids*, vol. 26, no. 4, p. 041701, Apr. 2014, doi: 10.1063/1.4870254.

[104] S. KOSHIGOE, E. GUTMARK, K. C. SCHADOW, and A. TUBIS, “Initial development of noncircular jets leading to axis switching,” *AIAA J.*, vol. 27, no. 4, pp. 411–419, 1989, doi: 10.2514/3.10128.

[105] K. B. M. Q. Zaman, “Axis switching and spreading of an asymmetric jet: the role of coherent structure dynamics,” *J. Fluid Mech.*, vol. 316, pp. 1–27, Jun. 1996, doi: 10.1017/S0022112096000420.

[106] F. Hussain and H. S. Husain, “Elliptic jets. Part 1. Characteristics of unexcited and excited jets,” *J. Fluid Mech.*, vol. 208, pp. 257–320, Nov. 1989, doi: 10.1017/S0022112089002843.

[107] F. Krebs, F. Silva, D. Sciamarella, and G. Artana, “A three-dimensional study of the glottal jet,” 2012, Accessed: Oct. 14, 2019. [Online]. Available: https://hal.archives-ouvertes.fr/hal-00653101.

[108] A. Krothapalli, D. Baganoff, and K. Karamcheti, “On the mixing of a rectangular jet,” *J. Fluid Mech.*, vol. 107, pp. 201–220, Jun. 1981, doi: 10.1017/S0022112081001730.

[109] T. Van Buren, D. Floryan, D. Brunner, U. Senturk, and A. J. Smits, “Impact of trailing edge shape on the wake and propulsive performance of pitching panels,” *Phys. Rev. Fluids*, vol. 2, no. 1, p. 014702, Jan. 2017, doi: 10.1103/PhysRevFluids.2.014702.

[110] A. Hemmati, T. Van Buren, and A. J. Smits, “Effects of trailing edge shape on vortex formation by pitching panels of small aspect ratio,” *Phys. Rev. Fluids*, vol. 4, no. 3, p. 033101, Mar. 2019, doi: 10.1103/PhysRevFluids.4.033101.

[111] C. Zhang, H. Huang, and X.-Y. Lu, “Effect of trailing-edge shape on the self-propulsive performance of heaving flexible plates,” *J. Fluid Mech.*, vol. 887, Mar. 2020, doi: 10.1017/jfm.2019.1076.

[112] R. Mittal and G. Iaccarino, “Immersed Boundary Methods,” *Annu. Rev. Fluid Mech.*, vol. 37, no. 1, pp. 239–261, 2005, doi: 10.1146/annurev.fluid.37.061903.175743.

[113] N. D. Ebrahimi, J. D. Eldredge, and Y. S. Ju, “Three-dimensional characteristics of the jet flows induced by a pitching plate in a quiescent fluid,” *J. Fluid Mech.*, vol. 887, Mar. 2020, doi: 10.1017/jfm.2020.2.

[114] J. Stafford and N. Jeffers, “Aerodynamic Performance of a Vibrating Piezoelectric Blade Under Varied Operational and Confinement States,” *IEEE Trans. Compon. Packag. Manuf. Technol.*, vol. 7, no. 5, pp. 751–761, May 2017, doi: 10.1109/TCPMT.2017.2666879.

[115] J. C. R. Hunt, “Eddies, streams, and convergence zones in turbulent flows,” *Cent. Turbul. Res. Rep.*, vol. CTR-S88, pp. 193–208, Dec. 1988.

[116] M. J. Lighthill, *Boundary layer theory*. Oxford University Press London, 1963.

[117] B. R. Morton, “The generation and decay of vorticity,” *Geophys. Astrophys. Fluid Dyn.*, vol. 28, no. 3–4, pp. 277–308, Apr. 1984, doi: 10.1080/03091928408230368.

[118] T. Lundgren and P. Koumoutsakos, “On the generation of vorticity at a free surface,” *J. Fluid Mech.*, vol. 382, pp. 351–366, Mar. 1999, doi: 10.1017/S0022112098003978.

[119] N. Dehdari Ebrahimi and Y. S. Ju, “Thermal conductivity of sintered copper samples prepared using 3D printing-compatible polymer composite filaments,” *Addit. Manuf.*, vol. 24, pp. 479–485, Dec. 2018, doi: 10.1016/j.addma.2018.10.025.

[120] L. Ventola *et al.*, “Rough surfaces with enhanced heat transfer for electronics cooling by direct metal laser sintering,” *Int. J. Heat Mass Transf.*, vol. 75, pp. 58–74, Aug. 2014, doi: 10.1016/j.ijheatmasstransfer.2014.03.037.

[121] X. Gao and B. Sundén, “Heat transfer and pressure drop measurements in rib-roughened rectangular ducts,” *Exp. Therm. Fluid Sci.*, vol. 24, no. 1, pp. 25–34, Mar. 2001, doi: 10.1016/S0894-1777(00)00054-6.

[122] S. B. Bopche and M. S. Tandale, “Experimental investigations on heat transfer and frictional characteristics of a turbulator roughened solar air heater duct,” *Int. J. Heat Mass Transf.*, vol. 52, no. 11, pp. 2834–2848, May 2009, doi: 10.1016/j.ijheatmasstransfer.2008.09.039.

[123] C. Thianpong, T. Chompookham, S. Skullong, and P. Promvonge, “Thermal characterization of turbulent flow in a channel with isosceles triangular ribs,” *Int. Commun. Heat Mass Transf.*, vol. 36, no. 7, pp. 712–717, Aug. 2009, doi: 10.1016/j.icheatmasstransfer.2009.03.027.

[124] Y.-T. Yang and P.-J. Chen, “Numerical Optimization of Turbulent Flow and Heat Transfer Characteristics in a Ribbed Channel,” *Heat Transf. Eng.*, vol. 36, no. 3, pp. 290–302, Feb. 2015, doi: 10.1080/01457632.2014.916158.

[125] S. W. Chang, A. W. Lees, and T. C. Chou, “Heat transfer and pressure drop in furrowed channels with transverse and skewed sinusoidal wavy walls,” *Int. J. Heat Mass Transf.*, vol. 52, no. 19, pp. 4592–4603, Sep. 2009, doi: 10.1016/j.ijheatmasstransfer.2009.02.039.

[126] S. W. Chang, K. F. Chiang, and T. C. Chou, “Heat transfer and pressure drop in hexagonal ducts with surface dimples,” *Exp. Therm. Fluid Sci.*, vol. 34, no. 8, pp. 1172–1181, Nov. 2010, doi: 10.1016/j.expthermflusci.2010.04.006.

[127] C. Slabaugh, “Heat Transfer Augmentation In A Narrow Rectangular Duct With Dimples Applied To A Single Wall,” *Electron. Theses Diss.*, Jan. 2010, [Online]. Available: https://stars.library.ucf.edu/etd/4359.

[128] S. W. Chang, T.-M. Liou, and M. H. Lu, “Heat transfer of rectangular narrow channel with two opposite scale-roughened walls,” *Int. J. Heat Mass Transf.*, vol. 48, no. 19, pp. 3921–3931, Sep. 2005, doi: 10.1016/j.ijheatmasstransfer.2005.04.015.

[129] S. W. Chang, T.-M. Liou, K. F. Chiang, and G. F. Hong, “Heat transfer and pressure drop in rectangular channel with compound roughness of V-shaped ribs and deepened scales,” *Int. J. Heat Mass Transf.*, vol. 51, no. 3, pp. 457–468, Feb. 2008, doi: 10.1016/j.ijheatmasstransfer.2007.05.010.

[130] T. M. Liou, S. W. Chang, J. S. Chen, and C. Y. Chan, “Fluid Flow Inside a Rectangular Duct With Two Opposite Walls Roughened by Deepened Scales,” pp. 161–170, Jan. 2009, doi: 10.1115/GT2009-59302.

[131] S. W. Chang, T. L. Yang, T.-M. Liou, and G. F. Hong, “Heat transfer of rotating rectangular duct with compound scaled roughness and V-ribs at high rotation numbers,” *Int. J. Therm. Sci.*, vol. 48, no. 1, pp. 174–187, Jan. 2009, doi: 10.1016/j.ijthermalsci.2008.03.001.

[132] S. W. Chang, T. L. Yang, T.-M. Liou, and H. G. Fang, “Heat transfer in rotating scale-roughened trapezoidal duct at high rotation numbers,” *Appl. Therm. Eng.*, vol. 29, no. 8, pp. 1682–1693, Jun. 2009, doi: 10.1016/j.applthermaleng.2008.07.024.

[133] S. W. Chang and A. W. Lees, “Endwall heat transfer and pressure drop in scale-roughened pin-fin channels,” *Int. J. Therm. Sci.*, vol. 49, no. 4, pp. 702–713, Apr. 2010, doi: 10.1016/j.ijthermalsci.2009.09.008.

[134] S. W. Chang and C. Y. Lin, “Thermal performance improvement with scale imprints over boiling surface of two-phase loop thermosyphon at sub-atmospheric conditions,” *Int. J. Heat Mass Transf.*, vol. 56, no. 1, pp. 294–308, Jan. 2013, doi: 10.1016/j.ijheatmasstransfer.2012.08.060.

[135] F. Zhou and I. Catton, “A Numerical Investigation of Turbulent Flow and Heat Transfer in Rectangular Channels With Elliptic Scale-Roughened Walls,” *J. Heat Transf.*, vol. 135, no. 8, pp. 081901-081901–9, Jun. 2013, doi: 10.1115/1.4024278.

[136] F. Zhou, G. W. DeMoulin, D. J. Geb, and I. Catton, “Closure for a plane fin heat sink with scale-roughened surfaces for volume averaging theory (VAT) based modeling,” *Int. J. Heat Mass Transf.*, vol. 55, no. 25, pp. 7677–7685, Dec. 2012, doi: 10.1016/j.ijheatmasstransfer.2012.07.075.

[137] F. Zhou and I. Catton, “Obtaining closure for a plane fin heat sink with elliptic scale-roughened surfaces for Volume Averaging Theory (VAT) based modeling,” *Int. J. Therm. Sci.*, vol. 71, pp. 264–273, Sep. 2013, doi: 10.1016/j.ijthermalsci.2013.04.020.

[138] N. Dehdari Ebrahimi and Y. S. Ju, “Heat Transfer Augmentation Using Scale-Roughened Surfaces for Low-Reynolds Number Flows Generated by Piezoelectric Fans,” in *2019 18th IEEE Intersociety Conference on Thermal and Thermomechanical Phenomena in Electronic Systems (ITherm)*, May 2019, pp. 1212–1219, doi: 10.1109/ITHERM.2019.8757369.

[139] F. P. Incropera and A. S. Lavine, *Fundamentals of Heat and Mass Transfer*. John Wiley & Sons, 2011.

[140] J. C. Han, J. S. Park, and C. K. Lei, “Heat Transfer Enhancement in Channels With Turbulence Promoters,” *J. Eng. Gas Turbines Power*, vol. 107, no. 3, pp. 628–635, Jul. 1985, doi: 10.1115/1.3239782.

[141] C. S. Lee, J. Joo, S. Han, and S. K. Koh, “An approach to durable PVDF cantilevers with highly conducting PEDOT/PSS (DMSO) electrodes,” *Sens. Actuators Phys.*, vol. 121, no. 2, pp. 373–381, Jun. 2005, doi: 10.1016/j.sna.2005.03.005.

[142] B. Gaihre, G. Alici, G. M. Spinks, and J. M. Cairney, “Synthesis and performance evaluation of thin film PPy-PVDF multilayer electroactive polymer actuators,” *Sens. Actuators Phys.*, vol. 165, no. 2, pp. 321–328, Feb. 2011, doi: 10.1016/j.sna.2010.10.009.

[143] A. M. Vinogradov, V. Hugo Schmidt, G. F. Tuthill, and G. W. Bohannan, “Damping and electromechanical energy losses in the piezoelectric polymer PVDF,” *Mech. Mater.*, vol. 36, no. 10, pp. 1007–1016, Oct. 2004, doi: 10.1016/j.mechmat.2003.04.002.

[144] Y. Fu, E. C. Harvey, M. K. Ghantasala, and G. M. Spinks, “Design, fabrication and testing of piezoelectric polymer PVDF microactuators,” *Smart Mater. Struct.*, vol. 15, no. 1, pp. S141–S146, Dec. 2005, doi: 10.1088/0964-1726/15/1/023.